ANNUAL REPORT
of
THE INSTITUTE OF PHYSICS
ACADEMIA SINICA

JUNE 1990

ACADEMIA SINICA
REPUBLIC OF CHINA

ANNUAL REPORT
of
THE INSTITUTE OF PHYSICS
ACADEMIA SINICA

VOLUME 19 JUNE 1990

THE INSTITUTE OF PHYSICS, ACADEMIA SINICA

TAIPEI, TAIWAN, REPUBLIC OF CHINA

中央究研院物理研究所集刊

發行人 (Publisher)
何侗民 (L. T. Ho)

編輯 (Editor)
蕭先雄 (S.S. Hsiao)
陳志強 (C.K. Chan)

The Annual Report is published annually by the Institute of Physics, Academia Sinica, Taipei Taiwan, 115, Republic of China.

中央研究院物理研究所集刊

中央研究院物理研究所印行

CONTENTS 目 錄

NEW PELLETRON TANDEM ACCELERATOR FOR RESEARCH

E. K. Lin, C. W. Wang, P. K. Teng, G. C. Kiang, C. Y. Chen
S. C. Wu and C. H. Hsieh

Institute of Physics, Academia Sinica, Taipei, Taiwan
Republic of China

Abstract*

A 3 MV Pelletron tandem accelrator of NEC model 9SDH-2 has been installed at the Institute of Physics, Academia Sinica. Detailed description of the accelerator systems is given. Results of the beam performance are presented. For experiments we have established three beamlines on which three newly built target chambers were mounted. Areas of research with use of accelerator are suggested.

I. Introduction

A 3 MV Pelletron tandem accelerator is now operational at the Institute of Physics, Academia Sinica. It is an ion accelerator of model 9SDH-2 manufactured by the National Electrostatics corporation (NEC), Wiscosin, USA [1]. Since the new technology of pelletron charging chains for the electrostatic accelerator to replace the belt was developed in 1970, many S-Series Pelletrons rated at terminal voltage below 3 MV have been installed in the small accelerator laboratories over the world and used entensively for research in atomic physics and materials technology. Accelerators of this type capable of producing good beam quality have the following main features:

(1) use pelletron charging chains which consist of metal cylinders joined by links of solid insulating plastic.

(2) use all metal and ceramic for acceleration tubes.

(3) use metal gaskets for vacuum system and no oil-diffusion pump.

In recent years the higher rated Pelletrons have met their terminal voltage to operate at 3 MV. The 3MV Pelletron became commercial in 1985 [1]. The higher rated Pelletrons broaden the range of possibilities for accelerator applications in general research and technology. From 1987-89 more new 3 MV tandem accelerators have been installed than any other low energy accelerators [2-5] and good performance of operation has been reported [6]. Table 1 lists the 9SDH-2 Pelletron being installed in universities, national laboratories and industrial research laboratories over the world since it was introduced in market in 1985.

II. Project Schedule

The accelerator project for the Institute of Physics was initiated in 1985. We considered the 3 MV 9SDH-2 Pelletron a suitable accelerator to be installed with versatility in adapting to our experimental needs for basic research in atomic and nuclear physics and for a wide range of ion beam techniques applications. It features easy operation and maintenance, excellent voltage stability, high reliability, flexible energy control, and minimum radiation.

The construction of the Physics Building has been completed in 1984, of which the basement was designed for installation of a small accelerator. A $2^m \times 2^m$ hatch at one end of the first floor was prepared to allow removal of heavy equipments for the accelerator. After taking two years for preparation, the accelerator project has been set into operation in 1986. In 1987 the government funding was granted and later the contract was signed with NEC to purchase a 9SDH-2 Pelletron.

In December 1988 two colleagues of the accelerator group of the Institute made a visit to NEC factory and worked with NEC people during the assembly and testing of our Pelletron systems for familiarization and first-hand experience with the systems. Before the shipment arrival, we have set up the power cabling for ion injector system, switching and analyzing magnets, main components of the

accelerator and gas handling systems. We have also set up the cooling water system and compressed air system, and completed the preliminary beamline alignment. Most ultilities were placed in the basement, and cable ways for experimental signals were placed on the periphercal walls of building to isolate them from equipment power and controls.

The shipment which consists of 37 packed boxes arrived at the Institute on March 20, 1989. All was inside the building and in place by March 28, 1989. The installation proceeded smoothly and the work for installation of entire systems was completed in three weeks with help of two NEC's technical staffs.

III. The Accelerator Systems

3.1 Ion Injection System

The ion injection system includes two sources of negative ions (SNICS II for solid source material and Alphatorss for noble gas source), 30° injection magnet, pump station, double slits, Faraday cup, X-Y steerers and Einzel lens. Power supplies in the ion injection system are regulated and equipped with a spark protection circuit.

The SNICS II utilizes a cesium plasmas which is produced by surface ionization on a hot tantalum helix coaxial with a cathode made (or coated) with a small amount of the element to be ionized to introduce sputtering from the cathode, it will produce negative ions of most sputterable elements of solid materials [7]. Negative ions produced at about 5 keV energy in the source are focused and accelerated to a maximum of 80 keV as they reach the 30° injection magnetic image slit by the extractor-einzel lens and air insulated acceleration tubes. The negative ions are then injected into the accelerator. A 0-10 kv, 5 μA and a 0-15 kv, 1.25 μA high voltage power supply is used for the extractor and Einzel lens respectively.

The SNICS source vacuum volume is extremely small. A gate valve is equipped to allow rapid changing from one ion beam species to another. Usually change of the sputter cathode can be done in ~10 min.

The Alphatross is a RF positive ion source-rubidium metal charge exchange negative ion source, developed by Richard and Billen [8,9]. It utilizes an air-cooled positive RF ion source to inject positive ions into a Rb metal vapor charge exchange cell. There is a Rb oven producing Rb metal vapor. Collisions with the Rb vapor convert a portion of positive ions to negative ions in the charge exchange process. As a result, a portion of negative ion beam is produced. Rubidium metal is used as to maximize negative ion beam yields at the ion source production energies. Negative ions produced at about 5 keV energy in the source and extractor are focused and accelerated in the preaceeleration tube of metal and ceramic, as in the case of the SNICS system, to a total of 80 kev as they reach the injection magnetic image slit by the extractor einzel lens and air insulated acceleration tube. This ion source will produce negative ions of helium or hydrogen isotopes by simply changing the source feed gas.

The injection magnet is used to select the negative ions produced from SNICS or Alphatross. A double slit and a Faraday cup are mounted immediately following the injection magnet. They are used to separate unwanted ions and to measure the beam to be injected into the accelerator and as a part of the accelerator safety interlock system.

Two electrostatic X-Y steerers (one in the pump tee, and one between the injection magnet and the base of the accelerator tank) and a 40 kv einzel len (between the injection magnet and the accelerator entrance) are used to focus and direct the negative ion beams into the accelerator terminal stripper tube.

3.2 The Accelerator

The accelerator is of NEC new model 9SDH-2 Pelletron tandem with 3 MV terminal voltage. It includes 9 accelerating tube sections each side of high voltage terminal; 24 inch diameter column; 2 chain pellet charging systems; turbo-molecular pumped gas stripping in high voltage terminal; foil stripper; corona triode point and energy stabilizer circuit; generating meter; capacitator pickup; pressure tank; and control console with remote control of accelerator. The accelerator is operated using about 80 psig pressure of SF_6 as insulating gas. Most of the SF_6 gas below atmospheric pressure can be recovered by using a gas handling system. The negative ions injected from ion sources are first accelerated to the terminal inside the accelerating tube, then stripped with either a gas or a foil stripper and further accelerated in the second stage of the accelerator.

Two charging chain systems are installed in the column. They are designed to deliver full charging current of about 300 A at terminal voltage. The system utilizes a rugged chain (1.25" in diameter) consisting of metal cylinders (pellet) joined by links of solid insulating plastic. Gaps between the adjacent metal cylinders serve as spark gaps in protecting the insulators in the chain. The chains are driven by two 3.0 hp motors. The total charging current of each pair of chains is monitored.

For operation in high pressure SF_6 the high electrical gradient acceleration tube is used. Acceleration tubes are organic-free and bakeable for ultra-high vacuum and contaminant-free operation. Tubes are made of 9 short sections bolted together, using metal gasket seals. Tube sections are of alumina ceramic and titanium. Annular spark gaps give excellent spark protection of the acceleration tube for long period operation.

The accelerator tank is about 18'9"(5.72m) in length, 4'0" (1.22m) in diameter, 229 cu.ft (6.49 m^3) in volume and weights 1800 kg. It is made of steel in two parts, an end and a bell section. After disconnecting the input and output beamlines and rolling the tank out to the side, the end section along with the accelerator column can be rolled out for servicing of the inner components of the accelerator. There are ports in the tank for two windows, electrical feed through, generating voltmeter of SF_6 gas fill.

The insulating column which supports the high voltage terminal spinning consists of four lucite plates. Insulating shafts running from the ground end to the terminal are used to control the stripper gas flow, titanium getter pump current and to select titanium getter elements in the terminal.

The high voltage terminal is about 26 inches (0.66m) in diameter and 30 inches (0.76m) in length. Voltage on the high potential terminal is stabilized by a feedback system incorporating a small beam current signal on a control slit after the analyzing-switching magnet and a biased corona needle pointing at the high voltage terminal. A reading of terminal voltage is displayed by a generating voltmeter reading of the electrostatic field at the tank wall.

For gas stripping, nitrogen stripper gas (stored in a bottle at 150 psig) is used in the high voltage terminal by means of a plastic tube from outside the pressure tank to feed gas to the stripper. Besides the gas stripping, the foil stripper is added to the terminal of accelerator. A carbon foil and target changers are used. The foil changer holds 48 thin carbon foil holders which are mounted on a small steel belt driven by a low power motor. It is possible to use foil stripping to get a higher charge state than is normally accomplished with gas stripping.

3.3 Vacuum System

The vacuum system of the Pelletron is of all metal and ceramic construction, with the exception of ion sources, turbo molecular and cryogenic pumps and gate valves, and is capable of ultra-high vacuum operation.

A 1100 ℓ/s air rated turbo-molecular pump with pneumatic actuated gate value, a 400 ℓ/m air rated mechanical fore pump, an automtic isolation and bleed-up valve and connectors are used to the injection beamline on which the Alphatross is mounted. Instead, a 6″ cryopumps is used to the SNICS beamline. Both SNICS and Alphatross beamlines can be maintained at 1 X 10^{-8} Torr or better.

Additional two 6″ cryopumps are used for the accelerator, installed in the two ends of the accelerator respectively. It can be maintained at 1 X 10^{-8} Torr to 5 X 10^{-8} Torr when no beam or tube conditioning are present.

A 120 ℓ/s Perkin Elmer ion pump is used to evacuate the beamline region between the analyzing and switching magnets. Additional two 120 ℓ/s ion pumps are used for the 0° and 15° beamlines from the switching magnet to target chambers respectively. While for the −30° beamline on which a RBS chamber is mounted, a 360 ℓ/s turbo-molecular pump is used.

The entire vacuum system and injection system are equipped with interlock system which interlocks on power fail and vacuum fail.

3.4 Analyzing and Switching Systems

The analyzing system consists of mainly a 90° analyzing magnet which is double focusing with a mean deflection radius of 48 inches (1.22m). The magnet has a maximum mass-energy product (ME/Z^2) of 150 amu-MeV. It is water cooled. For ^{58}Ni beams with energies 9 MeV (for 2+) and 12 MeV (for 3+) for example, the mass-energy products are 130.5 amu-MeV (2+) and 77.3 amu-MeV (3+), both of these beams can be easily handled by the magnet. A solid state current regulated power supply 0-40 volt, 320 ampere is used for the magnet. A cryopump station identical to those in the ion injection system is used to evacuate the high energy end of the accelerator.

The switch magnet has a maximum mass energy product of 150 amu-MeV at 15° and 18 amu-MeV at 45°. It has a stainless steel vacuum chamber with exit ports at ±45°, ±30°, ±15°, 0°. It is also water cooled. A solid state current regulated power supply 0-15 volt, 150 ampere is used for the magnet. To focus the beam of ions from the analyzing magnet into the switching magnet, a magnetic quadruple doublet is used and is located in front of the switching magnet.

Also, a magnetic quadruple doublet with remote control is used to focus the accelerated beam from the switching magnet into the target chamber. A beam profile monitor and a Faraday cup are mounted to monitor the beam at the end of the beamline. Placement of beam handling and beam monitoring component is determined from beam optics calculation.

The switching magnet is provided with 7 ports. The deflection of beam is controlled by the magnetic field of switching magnet. Gate valves are used for isolation of the beamline extension from the magnet and the target chamber. All beamlines setup are metal sealed with the exception of the large pump isolation valves.

IV. System Performance

The installed Pelletron started to operate in the middle of April, 1989. Table 2 shows the NEC specifications of 9SDH-2 Pelletron, and Table 3 gives our results obtained in the acceptance test. The guaranteed beam currents were all obtained. Beam transmissions through the accelerator were found to be very good especially using the foil stripper. It is noted that ^{3}He and ^{90}Zr ion beams were the first time data that have been acumulated on any 9SDH-2 machine for these beams. Also, new data on ^{3}He beam was obtained with two particle microamperes on target.

Over the period of ten months since operation, the accelerator has operated reliably. We found the energy stability of accelerator is excellent. The 3.0 MV rated terminal voltage can be reached within a few minutes after accelerator start up. In this period we have gained much experience with operation of the Pelletron system. So far we encounter almost no trouble. Several problems did happen, but soon be solved without causing trouble. The frequent problem happened was related with the fracture of a small connecting tube used for the Alphatross source. This problem has since been solved by a replacement of new connecting tube made of different material.

V. Experiment Area and Research

We have completed the installation of three beamlines at 0°, 15° and 30° from the switching magnet. It includes the beamlines from analyzing-switching magnet to the target chamber. Two target chambers (one for gas jet target and one for nuclear radiative transition reaction studies) have been built and installed at the end of the 0° and +15° beamlines. ·A NEC RBS-400 analytical end station has been set up at the 30° beamline. At present, there are three experimental areas are available for experiments. Totally up to five beamlines will be installed ultimately in the present beam room of rather limited space.

The first beamline (15°) is used for experiments in atomic physics. For the first series of experiments, we have set up a gas jet target to study the charge exchange transfer mechanism and molecular effect in the ion-atom collision induced by ion beams from the new Pelletron on a gas target. The experiments will follow soon.

The second beamline (0°) is used for experiments in nuclear physics. The present program of nuclear reaction studies with solid state detector and HpGe detector will be continued and extended by the availability of light and heavy ion beams. By using ion beams from our Pelletron in the MeV/amu range, experiments for nuclear reaction studies can be conducted. The great flexibility of the beam energy makes a very broad range of energy excitation measurements practical. We are interested in starting experimental investigation for some nuclear radiative transition reactions, heavy ion transfer reaction, and few-nucleon transfer reaction. One ongoing experiment was performed with use of the ^{4}He beam at energies 3.3 – 6.3 MeV bombarding on a thin Al target to study the ^{27}Al(^{4}He,p)^{30}Si and ^{27}Al(^{4}He,γ)^{31}P reactions. We have measured energy excitations in steps of 6 keV over the ^{4}He energy range 3.3 – 6.3 MeV. The results will be published later.

The third beamline (30°) permits measurements for RBS, PIXE, NRA channeling and all other ion beam techniques applications. It is expected to serve many users from outside the Institute doing research in a broad area of applied science and technology. The installed accelerator is adequate for a variety of research purpose. Areas of research with use of the new Pelletron are suggested as given in Table 4.

V. Summary

In summary, while the emphasis on fundamental and long term physics is maintained at the Institute, the installation of a 3 MV Pelletron tandem accelerator enable us to extend our research activities to applied physics and technology in addition to the atomic physics and low energy nuclear physics. The accelerator is the first one of electrostatic tandem type capable to produce light and heavy ion beams installed in Taiwan, ROC. It provides an useful experimental facility for local scientists to use for research and would promote the mutual collaboration between the Institute and universities as well as the cooperation with foreign leading laboratories.

References

1. J. B. Schroeder, C. W. Howell and G. A. Norton, Nucl. Instr. and Meth. B24/25 (1987) 763.
2. J. L. Duggan, Bull. of the APS, Vol. 33, No. 8 (1988) 1700.
3. J. M. Anthony, S. Matteson, F. D. McDaniel and J. L. Duggan, Nucl. Instr. and Meth. B40/41 (1989) 731.
4. Al-Juwair, M. M. Al-Kofahi, A. B. Hallak and M. Rajeh, Bull. of the APS, Vol. 33, No. 8 (1988) 1721.
5. C. C. Sun, C. R. Lu, Z. Y. Fe, D. S. Yuan and F. Yang, Nucl. Instr. and Meth. B40/41 (1989) 714.
6. See for instance: Proceedings of the 9th and 10th International Conference on the Application of Accelerators in Research and Industry at Denton, appeared in Nucl. Instr. Meth. B24/B25, 1987 and B40/B41, 1989.
7. R. D. Rathmell and G. A. Norton, Proc. 6th Inst. Conf. Implantation Technology, Nucl. Instr. and Meth. B21 (1987) 270.
8. H. T. Richards, Proc. Symp. on Ion Source and Formation of an Ion Beam, BNL 50301 (Upton, NY1071) P. 295.
9. J. H. Billen, IEEE Trans. Nucl. Sci NS-28 (1981).

TABLE 1 3 MV 9SDH Pelletron Installed in the World

Location	Country	Year
IBM, Yorktown	USA	1986
Los Alamos National Lab., Los Alamos	USA	1987
Naval Research Lab., Washington DC	USA	1987
Fudan University, Shanghai	POC	1987
North Texas State Univ., Denton	USA	1988
Institute of Physics, Academia Sinica, Taipei	ROC	1989
White Oakland Lab., Maryland	USA	1989
Institute of Physics, Bhubhaneswar	India	1989
Max Planck Institute, Heidelberg	Germany	1990
JAERI, Takasaki	Japan	1990

TABLE 2 Performance Specifications of Model 9SDH-2 Pelletron

Accelerator:		
Insulating Column Voltage Rating		3.00 Megavolts
Voltage Stability		Better than 1 KV
Voltage Ripple		500V peak-to-peak
Singly Charged Ion Energy Range		1.0 – 6.0 MeV
Doubly Charged Ion Energy Range		1.5 – 9.0 MeV
Triply Charged Ion Energy Range		2.0 – 12.0 MeV
Charging Current Rating		300 microamps (60Hz power) 250 microamps (50Hz power)
Beam Current (in acceptance test):		
	H^+	2.0 microamps at 3.0 MeV
	$^4He^{++}$	1.0 microamps at 3.0 MeV
	B^{++}	10.0 microamps at 9.0 MeV
	B^{+++}	6.0 microamps at 9.0 MeV
	Si^{++}	25.0 microamps at 9.0 MeV
Base Vacuum (no beam)		$1 \times 10^{-8} - 5 \times 10^{-8}$ Torr

TABLE 3. Measured beam current of the analyzed beams in the beam test

BEAM SPECIES	BEAM CURRENT MICROAMPERES	STRIPPER TYPE	INJECTED CURRENT MICROAMPERES	ENERGY MeV
$^{3}He^{+2}$	4.50	FOIL	2.50	9.0
$^{4}He^{+2}$	2.60	FOIL	1.60	9.0
B^{+}	0.250	GAS	6.89	6.0
B^{+2}	10.00	GAS	20.00	9.0
B^{+3}	10.03	GAS	9.28	12.0
B^{+4}	1.53	GAS	8.27	15.0
B^{+5}	0.036	GAS	8.27	18.0
Si^{+}	0.840	GAS	28.50	6.0
Si^{+2}	31.0	GAS	54.0	9.0
Si^{+3}	19.60	GAS	28.50	12.0
Si^{+4}	10.90	GAS	28.50	15.0
Si^{+5}	2.60	GAS	28.50	18.0
Si^{+6}	0.60	GAS	28.50	21.0
Si^{+7}	0.076	GAS	28.50	24.0
Si^{+8}	0.004	GAS	28.50	27.0
H^{+}	14.70	FOIL	19.70	6.0
H^{+}	15.25	GAS	26.70	1.50
H^{+}	9.51	GAS	30.50	0.60
Zr^{+3}	0.300	GAS	1.5*	12.0
Zr^{+4}	0.100	GAS	1.5*	15.0
Zr^{+5}	0.100	GAS	1.5*	18.0
Zr^{+6}	0.016	GAS	1.5*	21.0

* Zirconium injection current includes serveral isotopes 90, 91, 92.

TABLE 4. Suggested areas of research with use of the 3 MV Pelletron

Low-energy nuclear physics	Atomic Physics	Applied science and technology
nuclear radiative transition reaction	ion-atom collision	material analysis by PIXE, RBS, channeling and NRA
few-nucleon transfer reaction	inner-shell inoization	materials modification and ion implantation
cluster structure of light nuclei	atomic bremsstrahlung	depth profiling
coulomb excitation	X-ray production	isotropic analysis
energy levels of O-O nuclei	multiple inner shell ionization	ion beam technique application: to environmental problems
heavy ion induced fussion and transfer reaction	charge exchange reaction	chronometric dating
high spin states of compound nuclei	molecular effect	beam-foil interaction
lifetime of excited states problems related to astrophysics	proton-induced X-ray emission spectroscopy	radiation damage problems related to surface physics

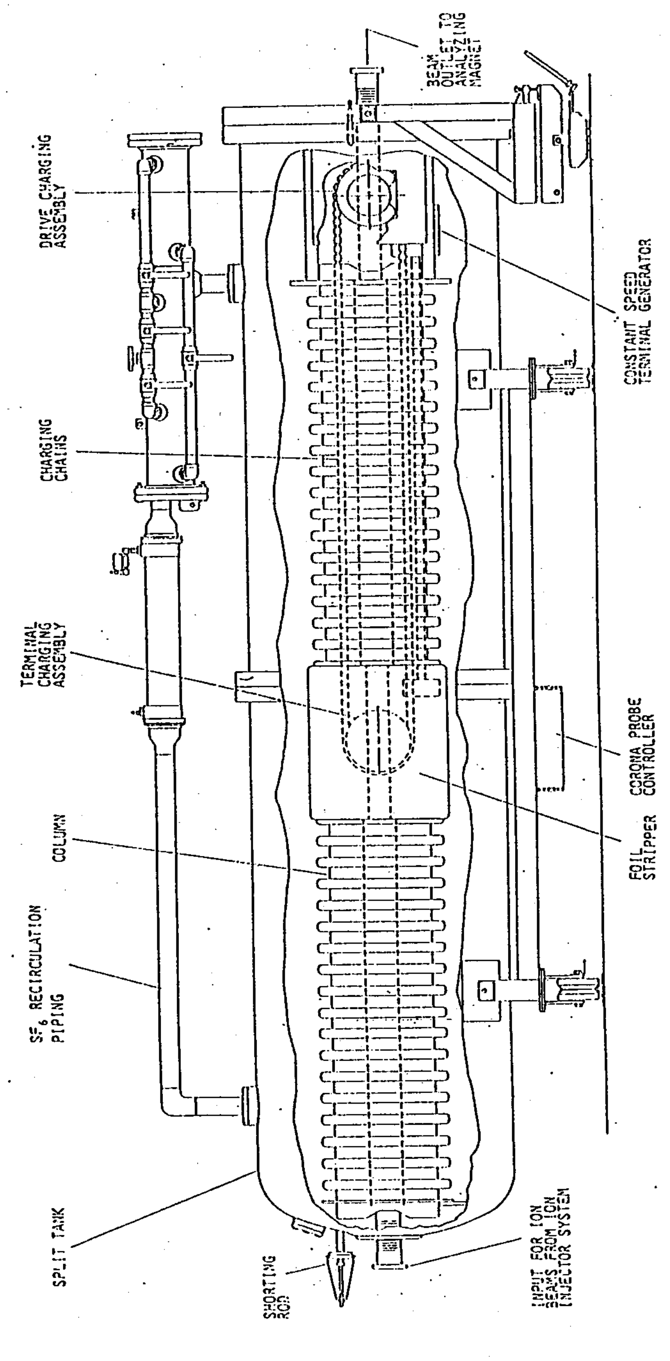

FIG. 1. A view of the Pelletron tandem accelerator inside the tank.

AN EXPERIMENTAL INVESTIGATION OF $H^+ + e \rightarrow H^0$ WITH A 350 keV PROTON BEAM ON A THIN CARBON TARGET

C. M. Fou, E. K. Lin, P. K. Teng and C. W. Wang

Institute of Physics, Academia Sinica, Nankang, Taipei 11529
Republic of China

Abstract

The reaction $H^+ + e \rightarrow H^0$ in ion-atom collisions was investigated from $\theta = 45°$ to $75°$. An enhancement of about 10% of the H^0 yield was observed between $60°$ and $65°$. Preliminary explanations for the experimental results and a discussion attributing the enhancement to classical double scattering known as the Thomas mechanism are presented.

Published in J. Phys. B: At. Mol. Opt. Phys. 22 (1989) 3017-3022.

由基態^{82}Br核經 β- 衰變形成^{82}Kr受激態實驗研究

李　琳
國立清華大學物理研究所

和

江紀成　鄧炳坤　林爾康　袁天竑　王建萬
羅榮立　程　斌
中央研究院物理研究所

摘　　要

我們利用高純度鍺—碘化鈉（鉈）組成的康普吞抑制能譜儀及高純度鍺—碘化鈉（鉈）晶體的符合電路，研究了由基態^{82}Br核經 β- 衰變後生成的^{82}Kr 受激態。在伽瑪單能譜中我們觀測到30個伽瑪躍遷，量度了6個串級伽瑪躍遷的方向角相關函數，並得出在^{82}Kr核中多伽瑪躍遷的多極性混合比 δ ，根據玻子作用模型（IBM）及其衍生的BSDI 模型我們計算了^{82}Kr核的能階，及其伽瑪躍遷的電雙極縮減躍遷機率B（E2）並與實驗的結果比較及討論。

刊於核子科學第廿六卷第一期，中華民國七十八年二月

STUDIES ON THE LEVEL STRUCTURE OF ^{154}Gd VIA THE β-DECAY OF ^{154}Eu NUCLEUS

L. L. Kiang[1], *G. C. Kiang*[2], *P. K. Teng*[2], *G. C. Jon*[2], *T. H. Yuan*[2]
and Y. M. Hsu[2]

1 Department of Physics, National Tsing-Hua University
Hsinchu, Taiwan, Republic of China
2 Institute of Physics, Academia Sinica, Taipei, Taiwan, Republic of China

Abstract

The excited state of ^{154}Gd populated by the β-decay of ^{154}Eu($T_{1/2}$ = 8.5 y) have been studied. With a HPGe-NaI(Tl) Compton suppression spectrometer and a HPGe-NaI(Tl) coincidence circuit γ-ray singles spectra, coincidence spectra and the γ-γ directional correlational functions have been obtained. The deduced mixing ratios of multipolarities are presented. The energy levels and the relative B(E2) values of the various γ-transitions in ^{154}Gd nucleus have been calculated both in the IBA model and it's extended version with boson surface delta interaction (BSDI).

Published in Z. Phys. A – Atomic Nuclei 333, 19-28 (1989).

SPECTROSCOPY OF ^{24}Al THROUGH THE ^{24}Mg(p, n)^{24}Al REACTION AT E_p = 35 MeV

G. C. Kiang[1], H. Orihara[1], Y. Takahashi[2], A. Satoh[2], T. Niizeki[1]
J. Takamatsu[2], M. Kabasawa[2], T. Kawamura[2], K. Furukawa[2], T. Nakagawa[2]
K. Maeda[3], K. Ishii[1], K. Miura[4], L. L. Kiang[5], P. K. Teng[6], and H. Ohnuma[7]

1 Cyclotron and Radioisotope Center, Tohoku University, Sendai 980, Japan
2 Department of Physics, Tohoku University, Sendai 980, Japan
3 College of General Education, Tohoku University, Sendai 980, Japan
4 Tohoku Institute of Technology, Sendai 982, Japan
5 Department of Physics, National Tsing Hua University, Hsinchu Taiwan 30042, Republic of China
6 Institute of Physics, Academia Sinica, Nankang, Taipei, Taiwan 11529 Republic of China
7 Department of Physics, Tokyo Institute of Technology, Tokyo 152, Japan

Abstract

An experimental study of the ^{24}Mg(p, n)^{24}Al reaction at E_p = 35 MeV was carried out. High-resolution neutron time-of-flight spectra were measured at 17 angles in a range of 0°-110°. Neutron peaks corresponding to seventeen states in ^{24}Al have been resolved. A number of spin-parity assignments have been made based on distorted-wave Born-approximation (DWBA) analyses for the measured angular distributions, using microscopic transition amplitudes obtained from the 1s0d shell model for positive-parity states and those from the 0s0p-1s0d-1p0f open-shell random phase approximation (OSRPA) for negative-parity states. Reasonable correlation between the low-energy (p, n) cross section and the β-decay strength has been found for the observed $0^+ \rightarrow 1^+$ Gamow-Teller transitions leading to the 0.439, 1.116 and 3.023 MeV states in ^{24}Al. The 1.56 MeV, 5^+ state has been identified as a 0 ħω stretched state, in addition to the 5.54 MeV, 6^- state of 1 ħω character. Candidates for the 1 ħω negative-parity transitions leading to the 2^-, 3^-, 4^- states are also presented.

Published in Nuclear physics A 499 (1989) 339-352.

TOWARD THE UNDERSTANDING OF K → 3π DECAYS IN CHIRAL PERTURBATION THEORY

Hai-Yang Cheng, C. Y. Cheung and Wai Bong Yeung

Institute of Physics, Academia Sinica, Taipei, Taiwan 11529

Abstract

Corrections to current-algebra analysis of $K \to 3\pi$ decay amplitudes are calculated using the dimension-four effective chiral Lagrangians, which are uniquely determined from the integration of nontopological chiral anomalies. We find that the constant and linear terms in the $\Delta I = ½$ amplitude are in good agreement with experiment; the previous discrepancy of 20–35% between current algebra and experiment is thus accounted for by including the higher order chiral Lagrangians. Predictions for quadratic terms are also given for both $\Delta I = 1/2$ and 3/2 transitions.

Published in Modern Phys. Lett. A4, 869 (1989).

ANALYSIS OF K → 3π DECAYS IN CHIRAL PERTURBATION THEORY

Hai-Yang Cheng, C. Y. Cheung and Wai Bong Yeung

Institute of Physics, Academia Sinica, Nankang
Taipei, Taiwan 11529, Republic of China

Abstract

Using the recently proposed higher-order chiral Lagrangians determined from the integration of nontopological chiral anomalies, we calculate corrections to the current-algebra analysis of $K \to 3\pi$ decay amplitudes expanded in powers of the Dalitz variables. Effects of quartic-derivative weak chiral Lagrangians are determined through the use of short-distance effective weak Hamiltonian and the factorization method. We find that (1) the constant and linear terms in the amplitude for $\Delta I = 1/2$ $K \to 3\pi$ are in excellent agreement with experiment; the previous discrepancy of (20–35)% between current algebra and data is thus accounted for by the higher-order effective Lagrangians, (2) the penguin interaction does not play an essential role in the $\Delta I = 1/2$ rule, for otherwise it will lead to a large disagreement for the constant and linear terms, (3) one of the two quadratic terms in the $\Delta I = 1/2$ process, which arise from the quartic chiral Lagrangians, is in accord with data within experimental errors, while the other is off by four standard deviations, (4) the linear term in the $\Delta I = 3/2$ transitions is in good agreement with experiment and contributions from quadratic terms are sizable.

Published in Z. Phys. C43, 391 (1989)

SOLVING A PHENOMENOLOGICAL TWO-BODY DIRAC EQUATION

C. Y. Cheung and S. P. Li

Institute of Physics, Academia Sinica, Taipei, Taiwan 11529
Republic of China

Abstract

We present a general scheme of solving a relativisitic two-body equation with phenomenological potentials. It is shown that, for a rather general class of local potentials, the problem can be reduced to that of solving a pair of coupled Schrödinger-type equations. A general discussion of the mixing of partial wave channels and the question of the Klein paradox is also presented.

Published in Phys. Lett. B234, 444 (1990)

ISOTROPIC TO LAMELLAR PHASE UNDER SHEAR

S. P. Li

Institute of Physics, Academia Sinica, Taipei, Taiwan 11529
Republic of China

Abstract

A class of models exhibiting an isotropic to lamellar phase transition under shear is considered here. Two competing types of fluctuations, namely, the nonlinear coupling fluctuations and mode coupling fluctuations are included to study the change of the critical behavior of these models.

PACS numbers: 47.20 Hw, 61.25 Hg, 64.60 Ht, 64.70Md.

A VECTORIZED ALGORITHM ON THE ETA-10Q FOR MD SIMULATION OF PARTICLES IN A BOX INTERACTING BY LONG-RANGED FORCES

S. C. Wang, C. K. Chan and S. P. Li

Institute of Physics, Academia Sinica
Taipei, Taiwan 11529, Republic of China

Abstract

We present a thoroughly vectorizable algorithm suitable for molecular dynamics (MD) computer simulation of particles confined in a box and interacting via long-ranged forces. A substantial reduction of computational CPU time has been achieved.

對流雲的模擬與應用

王崑洲　　　　曾忠一
交通部民航局　　中央研究院物理研究所

摘　　要

本研究旨在建立一個二維軸對稱對流雲數值模式，來探討對流雲在其發展生命期中動力與雲微物理過程間的相互作用以及水相結構在雲發展過程上所可能扮演的角色，以了解其相對重要性。此二維數值模式是利用前向時間差分格式以及修正上游空間差分來解非彈性方程組，使得空間交錯網格內的熱胞得以發展成雲。模式中使用了很多微物理參數化和次網格參數化。

研究結果表明，雲的形成以及降水過程在模式裏都可以模擬出，而且在整個模擬過程中，也可看出不同雲微物理過程與雲發展的關係。由此關係我們發現，凝結量與凍結量在雲成長階段扮演著重要角色，而冰珠（雹）的熔解與水滴的蒸發則對雲的衰減具有決定性的作用。此外，模式中又分別模擬了無冰及不含雲冰兩種情況，以便了解其差異。結果顯示模式中的上升下降速度以及雲頂高度都比無冰相大，而比不含雲冰的情況略小，至於降水量則以無冰相情況最大。這說明了在深對流雲中，如果忽略了冰相結構，將會高估降水量而低估氣流強度。

關鍵詞：雲模式　　大氣對流

前　　言

積雲對流在大氣運動中屬於一種小尺度的垂直運動，由於它在大氣熱收支及天勢的演變上扮演著極爲重要的角色，因此有關對流雲的研究，在過去三十多年始終受到氣象學家的重視。尤其是近些年來觀測設備的進展，使得對流雲三維測更爲完整詳細，然而再好的觀測儀器對於這種在時間和空間上尺度如此小的

運動，仍受到極大的限制，故利用數值模式來模擬對流雲以獲取觀測上無法分辨的資料，已被視爲一種相當有效而重要的方法。

自從Malkus and Witt（1959）以及 Ogura（1963）首先利用數值試驗模擬積雲對流後，到目前爲止已發展完成的動力數值模式有很多，其中在雲微物理結構上大多採用水質整體技術，將降水粒子（液態或固態）的粒徑分布視爲呈Marshall-Palmer 的分布（Kessler, 1969）。少數因研究目的不同，使用詳盡的微物理技術，將降水粒子依粒徑大小分成許多不同的類別，如Takeda（1971)將水質細分爲7類，Danielsen et al.（1972）分爲40類，Ogura and Takahashi（1971）更細分爲61類。至於動力結構的處理大多配合所用的微物理過程而採取四種不同的簡化技術，這四種技術在應用上分別爲僅考慮垂直方向的一維雲模式、二維軸對稱雲模式、二維面對稱雲模式以及三維模式。

一般而言，強調雲微物理結構的一維模式都採用詳盡的微物理技術，因爲這種模式內省略了很多動力項，而使得小型計算機有足夠能力來解很多複雜的水質守恆方程；反之強調動力結構的二維或三維模式，則採用簡單的水質整體技術來處理微物理過程，以使計算機的儲存空間及運算速度得以對方程做時間積分。由此可見，要建立一個完整詳細的雲模式，除非大幅度改進計算機功能，否則任何雲模式都無法在動力或微物理過程上做詳細的討論而必須做某些簡化。

由於計算機能力的限制，目前所發展完成的三維數值雲模式，在雲微物理過程上都採用了高度參數化，因此如想更詳細探討對流雲的微物理結構，以及它們在雲發展上所扮演的角色，利用二維數值模式來模擬是一種有效的方法。近來在雲改造實驗上，二維數值模式更被用來做爲評估工作，並獲致相當成就（Orville et al., 1982；Hsie et al., 1980）。

早期由於處理雲微物理過程較爲困難，以致所有利用二維數值模式來模擬對流雲的研究，大多忽略了冰相結構，而只考慮液相的微物理過程，如Ogura（1963）不含降水過程的濕對流模式，以及Murray（1970），Takeda（1971），Takahashi（1975），Soong and Ogura（1973）等包含降水過程的積雲模式。因此這些

式基本上都是屬於暖雲或是無冰粒子的冷雲結構。直到Koenig and Murray 976）才開始將冰相微物理過程引進他們的雲模式中，以探討冰粒子在不同類型流雲（如海洋性或大陸性）內所扮演的角色，結果證實冰粒子的發展和豐富的含量對於雲內氣流的強度以及降水量有增強作用。在這個模式中，冰粒子依密度不分成同質核化和異質核化兩種類型。此種分類法雖忽略了冰雹和雪花的微物理過，然而對於雲冰和冰珠的微物理過程却有詳細的討論。後來Orville and Kopp 977）將冰雹成長的微物理過程引進他們的雹暴模式裏，結果和雷達所觀測到雹的結構相比較，顯示出模擬非常的成功。近來Lin et al.（1983）更將雪花的微理過程加入Orville and Kopp 的模式中，結果也十分滿意。到此有關冰相微物結構對現有的計算機能力而言，可說已相當完備和複雜。然而實際上由冰粒子的態分析顯示，並非模式中所假定呈規則形或是球形那樣的理想化。

因此最近有些從事雲物理研究的工作者，又開始研究是否能用某種技術（如數式）將冰粒子的粒徑和形狀定量特徵化，以改進模式中雲微物理參數化的缺點。信此種技術的成功，將有助於對流雲數值模式的再突破。

有關冰相微物理參數化的應用從1970年代以來，最簡單的有Ogura and Taahashi（1971）的方法，較複雜的除了Orville and Kopp（1977）的模式外，還Wisner et al.（1972），Takahashi（1976)等模式。本文基於研究熱帶地區對雲的目的，上述冰雹成長的複雜過程並不需要，而採用Cotton et al.（1981）簡的冰相參數化。

本模式發展之初是由李（1986）參考Soong and Ogura（1973）的軸對稱模式理，因此模式的基本架構和Soong and Ogura 一樣，但在數值的計算過程以及些技巧上有一些不同，然就雲的發展結構而言，兩者仍極爲相似（李，1986）。

本研究目的除了改進李（1986）的模式外，並改進 Cotton et al.（1981）的冰參數化，建立一個完整二維軸對稱模式，以探討單胞對流雲在其發展生命期中動與雲微物理過程間的相互作用以及冰粒子成長在雲發展過程上所可能扮演的角色進而利用此模式模擬實際對流雲，以檢驗此模式的模擬能力。最後並希望改善或

擴充模式爲播雲或三維數值模式，以便更有效的模擬對流雲的動力結構，並在未來台灣地區雲改造實驗上，能做爲先前的評估工作，以證據支持實驗的進行。此外，模式建立後也將有助於風暴的研究及提高對流性雷雨預報的準確率。

2.雲模式

此數值模式爲二維模式，所使用的熱動力方程及數值方法和Soong and Ogura (1973) 的雲模式略似，其中不同的是在雲微物理參數化方面，本模式加上了Cotton et al.(1981)的冰相參數化結構。因此，本模式中的對流雲是一混合雲結構。

模式內的水質分爲5類：水汽(q_v)、雲滴(q_c)、雨滴(q_r)、雲冰(q_I)和冰珠(q_g) 等。雲冰和冰珠依其粒徑大小又各分成三種及兩種形式。爲了模擬方便起見，模式中做了以下幾項定義和假設：

(1)雲滴的粒徑數目在整個模擬過程中視爲常數 50 cm^{-3} 。

(2)雲滴很小(< 30 μm)，其終端速度忽略不計。

(3)雨滴、雲冰和冰珠的粒徑視爲Marshall-Palmer (1948) 分布。

(4)冰相最初是由沈積核、接觸核和凍結核所形成。

(5)冰晶的數目密度假定爲溫度的函數(Fletcher, 1962)。

(6)雲內不允許有過飽和現象，如有過飽和將立即凝結成雲滴。

(7)環境密度的局部變化率假定爲零。

(8)在整個模擬過程中使用水質整體技術。

(9)降水粒子的拖曳力等於其本身重力。

模式中所使用的方程爲一組非彈性系統的運動方程，其包括二個動量方程、渦度方程、非彈性連續方程、熱力學方程、水汽方程、雲滴方程、雨滴方程、雲冰方程以及冰珠方程等10個方程。若以圓柱座標表示，就是

$$\frac{\partial u}{\partial t}=-u\frac{\partial u}{\partial r}-w\frac{\partial u}{\partial z}-c_p\bar{\theta}\frac{\partial \pi'}{\partial r}+F_r \tag{1}$$

$$\frac{\partial w}{\partial t}=-u\frac{\partial w}{\partial r}-w\frac{\partial w}{\partial z}-c_p\bar{\theta}\frac{\partial \pi'}{\partial z}+g\left(\frac{\theta'}{\bar{\theta}}+0.61q'_v-q_c-q_r-q_I-q_g\right)+F_z \tag{2}$$

$$\frac{\partial \eta}{\partial t}=-u\frac{\partial \eta}{\partial r}-w\frac{\partial \eta}{\partial z}+\left(\frac{2w}{\bar{\rho}}\frac{\partial \bar{\rho}}{\partial z}+\frac{u}{r}\right)\left(\eta-u\frac{\partial \bar{\rho}}{\partial z}\right)+uw\frac{\partial^2 \bar{\rho}}{\partial z^2}-\bar{\rho}g\frac{\partial}{\partial r}\left(\frac{\theta'}{\bar{\theta}}+0.61q'_v-q_c-q_r-q_I-q_g\right)+D_\eta \tag{3}$$

其中u和w代表風速，c_p爲乾空氣的定壓比熱，$\bar{\theta}$代表環境位溫，θ'代表位溫偏差，π爲無因次氣壓，其表達式爲$\pi=(p/p_o)^{R/C_p}$，R爲氣體常數，p_o爲參考氣壓，g爲重力加速度，q'_v爲水汽混合比，q_c爲雲滴混合比，q_r爲雨滴混合比，q_I爲雲冰混合比，q_g爲冰珠混合比。F_r，F_z 爲渦動擴散項。η爲渦度，其定義爲：

$$\eta=\partial\bar{\rho}u/\partial z-\partial\bar{\rho}w/\partial r$$

如另定義一流函數ψ，則

$$\eta=\frac{1}{r}\left(\frac{\partial^2\psi}{\partial z^2}+\frac{\partial^2\psi}{\partial r^2}-\frac{1}{r}\frac{\partial\psi}{\partial r}\right)$$

$$\frac{\partial r\bar{\rho}u}{\partial r}+\frac{\partial r\bar{\rho}w}{\partial z}=0 \tag{4}$$

$$\frac{\partial \theta'}{\partial t}=-u\frac{\partial \theta}{\partial r}-w\frac{\partial \theta}{\partial z}+\frac{Q_L}{\pi}+D'_\theta \tag{5}$$

Q_L的物理解釋將於冰相參數化中討論。

$$\frac{\partial q'_v}{\partial t}=-u\frac{\partial q'_v}{\partial r}-w\frac{\partial q'_v}{\partial z}+P_v+Dq'_v \tag{6}$$

$$\frac{\partial q_c}{\partial t}=-u\frac{\partial q_c}{\partial r}-w\frac{\partial q_c}{\partial z}+P_c+Dq_c \tag{7}$$

$$\frac{\partial q_r}{\partial t}=-u\frac{\partial q_r}{\partial r}-w\frac{\partial q_r}{\partial z}+\frac{1}{\bar{\rho}}\frac{\partial}{\partial z}(\bar{\rho}V_r q_r)+P_r \tag{8}$$

$$\frac{\partial q_i}{\partial t}=-u\frac{\partial q_i}{\partial r}-w\frac{\partial q_i}{\partial z}+\frac{1}{\bar{\rho}}\frac{\partial}{\partial z}\left(\bar{\rho}V_i q_i\right)+P_i \tag{9}$$

$$\frac{\partial q_g}{\partial t}=-u\frac{\partial q_g}{\partial r}-w\frac{\partial q_g}{\partial z}+\frac{1}{\bar{\rho}}\frac{\partial}{\partial z}\left(\bar{\rho}V_g q_g\right)+P_g \tag{10}$$

(5)到(10)式爲一組預報方程，其中P項代表水質的產生率，V_r 和 V_g 分別代表雨滴和冰珠的終端速度，D項則代表次網格擴散項，其表達式爲

$$D_\chi=\frac{1}{r}\frac{\partial}{\partial r}\left(Kr\frac{\partial\chi}{\partial r}\right)+\frac{1}{\bar{\rho}}\frac{\partial}{\partial z}\left(K\bar{\rho}\frac{\partial\chi}{\partial z}\right)$$

$$=K\left(\frac{\partial^2\chi}{\partial r^2}+\frac{\partial^2\chi}{\partial z^2}\right)+\frac{\partial\chi}{\partial r}\frac{\partial K}{\partial r}+\frac{K}{r}\frac{\partial\chi}{\partial r}+\frac{K}{\bar{\rho}}\frac{\partial\chi}{\partial z}\frac{\partial\bar{\rho}}{\partial z}+\frac{\partial\chi}{\partial z}\frac{\partial K}{\partial z}$$

其中渦動擴散係數K值根據Deardorff（1972），有

$$K=(c\Delta)^2\left\{\left(\frac{\partial w}{\partial r}+\frac{\partial u}{\partial z}\right)^2+2\left[\left(\frac{\partial u}{\partial r}\right)^2+\left(\frac{\partial w}{\partial z}\right)^2+\left(\frac{u}{r}\right)^2\right]\right\}^{1/2}$$

其中 $\Delta=(\Delta r\Delta z)^{1/2}$，$\Delta r$ 和 Δz 分別爲水平和垂直網格間距。c爲無因次量常數，其值根據Deardorff的研究取0.2。此K值可分別使用於 θ'，q_v' 和 q_c 之中。對 D_η 值的表達式爲

$$D_\eta=\frac{1}{r}\frac{\partial}{\partial r}\left(Kr\frac{\partial\eta}{\partial r}\right)+\frac{1}{\bar{\rho}}\frac{\partial}{\partial z}\left(K\bar{\rho}\frac{\partial\eta}{\partial z}\right)-K\frac{\eta}{r^2}$$

本研究目的在探討熱帶地區對流雲的熱動力結構及發展過程，因此採用熱帶標準大氣的溫度和濕度做爲模式的環境條件，其溫度濕度的廓線分別敍述如下：

(a)假設地表溫度爲25℃（298°K）且以乾絕熱遞減率向上減少至雲底，而雲底假定爲從地表往上至0.8 km處。

(b)地表相對濕度假設70％，線性上升至雲底爲90％。而在雲底之上，相對濕度則以7.5％ km^{-1} 向上遞減，在高層爲了和真實大氣類似，因而在較高層之相對濕度至少維持在30％。

(c)雲底之上，溫度遞減率爲6.0℃ km^{-1}。

由以上溫度廓線看出熱帶大氣在5公里以下屬於條件性不穩定層，有利於濕對

流的發展；此外環境風場在本模式中假設爲靜止狀態。

對流雲模式通常使用熱胞加熱方法，使模式在開始積分時產生運動，或者加入中尺度垂直運動場，如Soong and Ogura（1980），使模式之對流雲發展，此外亦可利用都卜勒雷達資料作爲初始條件。

本研究乃使用熱胞加熱方法來模擬對流雲的發展。爲了使對流雲能夠開始形成於模式的中心軸，因此在模式的中心軸放置一個熱胞，其放置方式如下：

$$\theta'=\theta_0\{1-[(z_0-z)/(z_0-\Delta z/2)]^2\}(1-r^2/r_0^2)$$

其中 θ_0 爲對中心軸而言，在 z_0 高度上位溫偏差最大的初始值，假設爲0.5°K；θ' 爲位溫偏差值在雲底之上位於網格的中央，其正值區正好爲相對濕度100％的雲內，此處 $z_0=1.0$ km，$r_0=1.2$ km。

模式裏的邊界條件採用水平速度u的自由滑動條件以及垂直速度w的上下固定條件。其假設條件爲

$w=0$， $\partial\bar{\rho}u/\partial z=0$， 在 $z=0$，z_H

$u=0$， $\partial w/\partial r=0$， 在 $r=D$

其中 z_H 爲積分範圍的高度，D爲由雲中心到側邊界的距離。由此假設條件可明顯看出渦度 η 和流函數 ψ 在四周邊界上爲零。

對 θ，q_v'，q_c，q_r，q_i，q_g 等物理量而言，其邊界條件並不需假設，因爲它們位於邊界內側網格的中央，並無邊界內外介入之問題，故在邊界上沒有定義。在計算這些物理量的渦動擴散項時，使其爲零以避免不實的擴散值越過邊界。此外在所有邊界條件中，θ 的改變因雲的生命期短且液態水初始值爲零而視爲不重要。

模式採用有限差分法求出數值解。在空間上的分布，使用交錯網格的修正上游格式，而時間差分則採用前向差分法。

對變數F（θ，q_v，q_c，q_r，q_i，q_g）而言，其分布如圖1所示。把有關熱力變數及水汽變數放在中間，而u和w的位置各向上向下及左右移半個間距。η 和 ψ 在網格點上，使用此格式的最大優點就是可以防止 q_r 和 q_g 因本身重量而降至地面，此外也不會使 q_r，q_c，q_i 和 q_g 變爲負值而產生誤差。因此對同一數目的網

格點而言，比用其他格式來講可以得到較高的準確度。同時此格式也節省儲存資料所佔空間（Wilhelmson, 1974）。

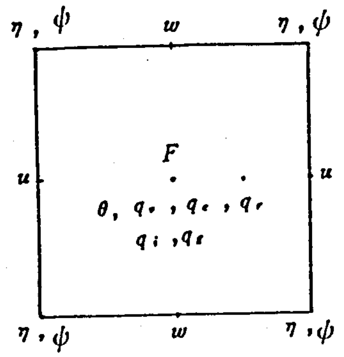

圖 1　各變數在網格系統中的位置

對變數 F 平流項而言，爲了守恒起見，均以通量形式表示：

$$\frac{\partial F}{\partial t}=-\frac{1}{r\bar{\rho}}\frac{\partial}{\partial r}(r\bar{\rho}uF)-\frac{1}{r\bar{\rho}}\frac{\partial}{\partial z}(r\bar{\rho}wF)$$

將上式以修正上游格式表達，可以寫爲如下的差分格式：

$$\left(\frac{\partial F}{\partial t}\right)_{i,k}=-\{(r_{i+1/2}\bar{\rho}u_{i+1/2}F_{i+1/2}-r_{i-1/2}\bar{\rho}u_{i-1/2}F_{i-1/2})_k/\Delta r+(r\bar{\rho}_{k+1/2}w_{k+1/2}F_{k+1/2}-r\bar{\rho}_{k-1/2}w_{k-1/2}F_{k-1/2})_i/\Delta z\}/r_i\bar{\rho}_k$$

在上式中右邊括號代表著變數 F 的內流和外流。

假定變數 F 在體積中均勻，那麼

$$F_{i+1/2,k}=\begin{cases}F_{i,k} & u_{i+1/2}>0\\ F_{i+1,k} & u_{i+1/2}<0\end{cases}$$

相同的條件適用於 $F_{i-1/2,k}$，$F_{i,k+1/2}$，$F_{i,k-1/2}$。對 η 的平流項採用上游格式。

模式中所取的網格間距及時間間距分別爲

$\Delta r=\Delta z=400\,m$，　$\Delta t=20\,sec$

至於積分範圍爲 12.8 km × 12.8 km。

3.雲微物理過程的參數化

自從 1949 年雷雨計劃證實在夏季對流雲中，冰晶的成長過程對於降水的發展具有決定性後，有關冰晶成長過程的個別研究受到氣象學家們的重視。然而在1970年代以前所有對流雲模式根本忽略了冰相結構。直到 1970 年的前半期，冰相結構的數值模擬才被引進對流雲模式中（如 Simpson and Wiggert, 1969；Hirsch, 1971；Cotton, 1972；Kachurin et al., 1973；Ogura and Takahashi, 1971；Wisner et al., 1972；Danielson et al., 1972；Orville et al., 1975；Takahashi, 1976）。其中在 Takahashi 的軸對稱冰雹模式更是詳細的探討冰雹成長的雲微物理過程，結果證實冰雹的成長對降水量的大小扮演著極爲重要的角色。根據以後的數值實驗結果（如 Orville and Kopp, 1977；Soong and Ogura, 1982；Cotton, 1981；Lin et al., 1983），若將冰相結構引進對流雲的動力模式中，模擬的結果與觀測結果更趨一致。以下將就本文所利用的雲微物理過程做一介紹。

本研究所使用的液相參數化和 Soong and Ogura（1973）一樣，但雨滴的終端速度稍做改變以和冰相參數化一致。

雨滴的粒徑分布假設呈 Marshall-Palmer（1948）分布，其分布是爲粒徑 D 的函數。其公式爲

$$N(D)=N_{0r}\exp(-\Lambda D) \tag{11}$$

其中 N(D) dD 爲 D 到 D + dD 間單位體積的粒徑數目，Λ 爲雨滴斜率，積分(11)式得到

$$\Lambda=\left[\frac{3.14\,N_{0r}}{q_r}\left(\frac{\rho_w}{\bar{\rho}}\right)\right]^{0.25}$$

N_{0r} 爲擴獲雨滴的斜率分布，設爲 0.08 cm⁻⁴，$\bar{\rho}$ 和 ρ_w 分別是空氣和液態水的密度。假設雨滴的拖曳力等於本身重力，則個別雨滴終端速度爲

$$V_r(D) = \left(\frac{4}{3}\frac{g\rho_w}{C_{dr}\bar{\rho}}\right)^{0.5} D^{0.5} \qquad (12)$$

其中拖曳係數 C_{dr} 取 0.587 。然後由(11)和(12)，我們得到雨滴加權平均後的終端速度

$$\overline{V}_r = 118.54\,\bar{\rho}^{-0.375} q_r^{0.125} \qquad (13)$$

在(6)(7)和(8)式中，水質產生率 P 可分成下列形式：

$$P_v = -C + E_r + E_c - P_{vi} \qquad (14)$$

$$P_r = P_{rc} + P_{ra} - E_r - P_{ri} \qquad (15)$$

$$P_c = C - E_c - P_{rc} - P_{ra} - P_{ci} \qquad (16)$$

其中 P_{rc} 和 P_{ra} 分別是雲滴的自動轉換和黏附率，根據 Kessler (1969)的研究分別爲

$$P_{rc} = K_1 (q_c - a)$$

$$P_{ra} = K_2 q_c q_r^{0.875}$$

其中參數 $K_1 = 10^{-3}\,\mathrm{sec}^{-1}$，$a = 10^{-3}\,g/g$，$K_2 = 2.2$，$E_r$ 和 E_c 分別爲雨滴和雲滴的蒸發率，我們假設如果空氣未飽和雲滴立即蒸發，如果空氣未飽和則雨滴繼續蒸發，其公式根據Ogura and Takahashi (1971)的研究爲

$$E_r = -\frac{1}{\bar{\rho}}\frac{[(q_v/q_{vs}) - 1]\,A\,(\bar{\rho} q_r)^{0.525}}{5.4\times 10^5 + (0.41\times 10^7/e_s)}$$

因 $e_s = \bar{p}\, q_{vs}/0.622$ ，故上式變爲

$$E_r = -\frac{1}{\bar{\rho}}\frac{[(q_v/q_{vs}) - 1]\,A\,(\bar{\rho} q_r)^{0.525}}{5.4\times 10^5 + 2.55\times 10^6/(\bar{p}\, q_{vs})} \qquad (17)$$

其中 $A = 1.6 + 5.7\times 10^3\,(\overline{V}_r)^{1.5}$

$$= 1.6 + 124.9\,(\bar{\rho} q_r)^{0.2046}$$

此乃通風係數。其中 q_{vs} 爲平水面上水汽的飽和混合比，e_s 爲平水面上的飽和水汽壓。在(14)式中 C 是凝結過程，P_{vi} 爲水汽凍結率，(15)中的 P_{ri} 是雨滴的凍結率，(16)中的 P_{ci} 是雲滴的凍結率。此三種凍結產生率將於下一節冰相參數化中討論。

本文使用Cotton et al. (1981)的冰相參數化，然而基於研究熱帶對流雲的目的，在模擬上做了二種參數的改變：(a)冰珠（雹）的總密度，(b)雨滴的粒徑分布。

基於在過飽和區免於重複計算的好處，本文將用Soong and Ogura (1973)的飽和技術，使雲內始終滿足飽和條件。

以下將介紹Cotton et al. (1981)的冰相參數化。在他的研究中，雲冰（雪晶）的粒徑分布用Fletcher (1962)所導的公式，假定和沈積核的數目一致，其表達式爲：

$$N_I = 10^{-5} \exp[\,0.6\,(273.16 - T)\,] \qquad (18)$$

然後個別的雲冰質量 m_I 爲

$$m_I = q_I\, \bar{\rho}/N_I$$

依其質量 m_I 將雲冰分成：未霜化、輕度霜化以及略似冰珠形式的六邊形雪片，由Hobbs et al. (1972)知粒徑和終端速度之間的關係有

$$D_I = c_1 m_I^{0.5}$$

$$V_I = c_2 D_I\,(p_o/p)^{0.5} \qquad (19)$$

這裏 $c_1 = 51.5\,\mathrm{cm\ g}^{-0.5}$，$c_2 = 304\,\mathrm{s}^{-1}$，當 $m_I < 1.7\times 10^{-7}\,g$

$c_1 = 19.2\,\mathrm{cm\ g}^{-0.5}$，$c_2 = 1250\,\mathrm{s}^{-1}$，當 $1.7\times 10^{-7}\,g \le m_I \le 1.0\times 10^{-5}$

至於質量大於 $1.0\times 10^{-5}\,g$ 的雪片由 Locatelli and Hobbs (1974) 的研究爲

$$D_I = c_1 m_I^{0.417}$$

$$V_I = c_2 D_I^{0.25}\,(p_o/p)^{0.5} \qquad (20)$$

這裏 $c_1 = 8.89\,\mathrm{cm\ g}^{-0.417}$

[illegible] $c_2 = 153\,\mathrm{cm}^{0.75}\,\mathrm{s}^{-1}$，　當 $m_I \ge 1.0\times 10^{-5}\,g$

上式中 c_1 和 c_2 分爲代表雲冰粒徑常數及終端速度常數。

[illegible] Cotton et al. (1981)假設很復雜的冰珠形式以及重霜化後冰粒子的數目密度 N_g 呈Marshall - Palmer 分布

[illegible] $N_g(D_g) = N_{og} \exp(-\lambda D_g)$ (21)

其中 N_{og} 是捕獲冰珠的斜率分布，λ 是冰珠分布斜率，D_g 是冰珠粒徑。冰珠總數目密度 N_{tg} 由(21)式做積分得

[illegible]

[illegible]

$$N_{tg}=\int_0^\infty N_g(D_g)\,dD_g=N_{og}/\lambda$$

此處 N_{tg} 假設爲一常數值。Cotton et al.(1981)採用 $10^{-4}cm^{-3}$，然而在熱帶地區所觀測的對流雲，缺乏像中緯度所觀測到的對流雲具有強烈的上升氣流以及再循環氣流，何況本模式爲一軸對稱模式，對於後者更是無法形成。因此，巨大的冰珠（雹）不容易形成，所以選擇粒徑較小，數目密度較大的冰做爲模擬對象，故 N_{tg} 取 $3.2\times10^{-3}cm^{-3}$。λ 值可由質量計算的積分求得

$$q_g=\int_0^\infty \frac{3.14}{6\bar{\rho}}D_g^3\rho_g N_{og}\exp(-\lambda D_g)\,dD_g$$

然後

$$\lambda=[3.14\,\rho_g N_{tg}/(\bar{\rho}q_g)]^{0.3333} \tag{22}$$

冰珠依質量大小以兩種不同形式的冰粒子代替，分別爲中度密度的冰珠（霰）和冰雹。然而只允許一種形式的混合比存在於網格點上，因此可以平均質量 $\overline{m}_g$ 來區別：

$$\overline{m}_g=\bar{\rho}q_g/N_{tg}$$

冰珠的密度 ρ_g 和拖曳係數 C_{dg} 爲

$\rho_g=0.6g\ cm^{-3}$；$C_{dg}=0.45$，當 $m_g<2\times10^{-2}g$

$\rho_g=0.9g\ cm^{-3}$；$C_{dg}=0.6$，當 $m_g\geq2\times10^{-2}g$

假設冰珠的拖曳力等於重力，則將粒徑分布做積分後，冰珠的終端速度 $\overline{V}_g$ 爲

$$\overline{V}_g=57.88\left[\frac{(\rho_g/\bar{\rho})^{0.333}}{N_{tg}^{0.17}C_{dg}^{0.5}}\right]q_g^{0.17} \tag{23}$$

在(9)和(10)式中的雲冰和冰珠的產生率 P_I 和 P_g 能夠分成下列形式：

$$P_I=P_{ns}+P_{rs}+P_{ds}-P_{ms}-P_{tg}$$

$$P_g=P_{rg}+P_{dg}+P_{fg}+P_{tg}+P_{cg}-P_{mg} \tag{24}$$

P 產生項的物理意義分別爲

P_{ns}：雲冰的核化速率，$T<0$℃

P_{rs}：過冷雲滴霜化成雪晶的速率，$T<0$℃

P_{rg}：過冷雲滴霜化成冰珠的速率，$T<0$℃

P_{ds}：水汽沈積至雪晶的速率，$T<0$℃

P_{dg}：水汽沈積至冰珠的速率，$T<0$℃

P_{fg}：過冷雨滴與冰晶接觸凝固成冰珠速率，$T<0$℃

P_{tg}：雲冰經重霜化後轉換成冰珠的速率，$T<0$℃

P_{cg}：冰珠收集雨滴的速率

P_{ms}：雲冰熔解成雲滴的速率，$T>0$℃

P_{mg}：冰珠熔解成雨滴的速率，$T>0$℃

有關這些項的參數公式將在後面加以介紹。根據以上各項的物理解釋(14)(15)(16)公式中的 P_{vl}，P_{cl}，P_{rl} 可分別寫成：

$$P_{vl}=P_{ns}+P_{ds}+P_{dg} \tag{25}$$

$$P_{cl}=P_{rs}+P_{rg}-P_{ms} \tag{26}$$

$$P_{rl}=P_{fg}+P_{cg}-P_{mg} \tag{27}$$

P_{ms} 和 P_{mg} 之熔解過程僅僅當溫度高於凝固點 0 ℃時才會發生。(26)(27)和(24)式中的 P_{fg} 爲平均液態水經由併合過程凍結成冰粒子的自動轉換項。(25)和(14)到(16)式中所描述的過程需用飽和技術，使得水汽和溫度在過飽和區回復到純水飽和點。當所有自動轉換項計算過後，已知溫度和水汽的混合比，爲達飽和狀態我們可算出水汽的凝結量。當溫度在 0 ℃以下時，由水汽的過飽和混合比扣除飽和混合比，然後再減去(25)式的 $P_{vl}\,\Delta t$，如果有剩餘水汽量則重複水汽凝結成雲滴的過程。至於在未飽和區時，雲滴、雨滴、冰晶可能同時蒸發。但本模式中我們假定雲滴先蒸發，如果空氣未飽和則雨滴蒸發，同樣的如果空氣仍未飽和，則讓冰粒子蒸發。在整個模擬過程中，總蒸發量不允許有超過飽和混合比的現象。

至於雲微物理過程如圖 2 所示。圖中所含之物理意義乃說明當熱胞向上運動時因絕熱冷卻產生空氣過飽和使得水汽凝結成雲滴，而雲滴因粒徑很小隨空氣向上升，經收集、自動轉換等效應使得雨滴成長，此時雨滴的終端速度如大於上升速

度則下降成雨，否則隨氣流上升，當上升氣流通過 0 ℃層以上時，飽和水汽藉核化、沈積等效應形成冰晶，而雲滴和雨滴則經擴散、碰併等效應成長大冰晶，此時當大冰晶（雹）的終端速度大於上升速度時，則開始降落，其間經熔解層 0 ℃以下時，產生熔解而成暖雲降水。以上整個降水過程中，始終包含水質在未飽和環境中的蒸發及昇華作用。

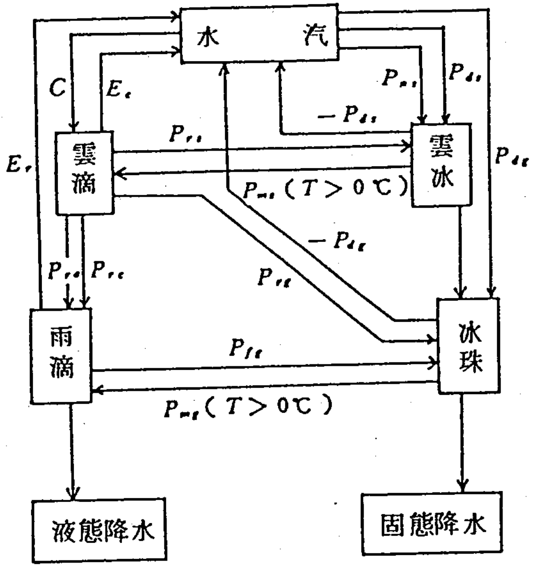

圖 2　雲微物理過程

在(5)位溫方程中的 Q_L 爲

$$Q_L=\frac{L}{c_p}(C-E)+\frac{L_s}{c_p}(P_{ns}+P_{ds}+P_{dg})+\frac{L_f}{c_p}(P_{rs}+P_{rg}-P_{ms}$$

$$-P_{mg}+P_{fg}+P_{cg})$$

其中L，L_s 和 L_f 分別爲凝結、昇華和凝固（熔解）潛熱。

溫度在凝固點以下，僅僅當空氣對水飽和時，P_{ns}，P_{ds}，P_{dg} 都是正值，否則 P_{ds} 和 P_{dg} 爲負值，而 P_{ns} 不會發生，根據 Cotton et al. (1981) 的研究其公式分別爲

$$P_{ns}=-0.6N_i(T)\,w\frac{\partial T}{\partial z}m_{io}/\bar{\rho}$$

$$P_{ds}=4D_iN_iSG(T,P)f(R_e)/\bar{\rho}$$

$$P_{dg}=SG(T,p)\left[K_{1g}+K_{2g}q_g^{0.25}\right]q_g^{0.33}$$

其中 $N_i(T)$是(18)的沈積核數目密度，是溫度的函數，w是垂直速度，$\partial T/\partial z$ 是垂直溫度梯度，m_{io} 爲雲冰初始質量取 10^{-9}g，D_i 爲三種雲冰形式的粒徑，S 爲對冰面上之過飽和值。其公式爲

$$S=q_v/q_{si}-1$$

q_{si} 爲對冰面上的飽和混合比，e_{si} 爲對冰面上的飽和水汽壓，根據Murray (1967) 的研究，其公式爲

$$e_{si}=6.1078\exp\left[21.8746(T-273.16)/(T-7.66)\right]$$

$$q_{si}=0.622\,e_{si}/\bar{p}$$

G(T，p)爲水汽沈積至冰面上的函數。Byers (1965) 定義爲

$$G(T,p)=\left(\frac{0.622\,L_s^2}{10^3\,\kappa RT^2}+\frac{RT}{0.622\,\phi e_{si}}\right)^{-1}$$

其中 κ 是熱力傳導係數，值爲 2500 erg $cm^{-1}s^{-1}$，ϕ 爲水汽擴散係數值爲 0.241 cm^2s^{-1}。R爲氣體常數值爲 2.87×10^3 mb cm^3/g °K。通風函數定義爲

$$f(R_e)=1+0.229(R_e)^{0.25}$$

其中 μ 爲動力黏性係數。V_i 則爲(19)和(20)所得到雪晶的終端速度。至於 K_{1g} 和 K_{2g} 則爲水汽沈積至冰珠上的係數。其公式如下：

$$K_{1g}=\frac{4.29N_{tg}^{0.67}}{\bar{\rho}^{0.67}\rho_g^{0.33}}\qquad K_{2g}=\frac{4.44N_{tg}^{0.42}}{\mu^{0.5}C_{dg}^{0.25}\bar{\rho}^{0.17}\rho_g^{0.33}}$$

其中 N_{tg} 爲冰珠數目總集中數。C_{dg} 爲拖曳力係數由 ρ_g 求得。根據 Cotton (1972) 的研究在熱動力平衡中，冰晶的霜化效應所釋放之熔解潛熱會透過分子擴散效應向環境空氣加熱。因此，在計算過程中，必需在飽和技術進行之前先計算過，而其所釋放之熱量將減少水汽的沈積及核化效應。

有關霜化過程的公式爲

$$P_{ri} = 0.785\, D_i{}^2 V_i E_i N_i q_c$$

$$P_{rg} = K_{rg} E_g q_c q_g{}^{0.83} \qquad (28)$$

雲冰和冰珠的有效係數分別爲

$$E_i = \left(1 + \frac{4.5\,\mu D_i}{\rho_w D_c{}^2 V_i} \right)^{-2} , \qquad E_g = \left(1 + \frac{1.11\,\mu D_g}{\rho_w D_c{}^2 V_g} \right)^{-2}$$

此外

$$K_{rg} = 1.16\, g^{0.5} \left(\frac{\bar{\rho}}{\rho_g} \right)^{0.33} N_{tg}{}^{0.17}\, C_{dg}{}^{-0.5}$$

其中冰珠的平均直徑 $D_g = 1 / \lambda$ 由(21)的積分和(22)得到的 λ 求得。ρ_w 爲水的密度值，取 1g cm^{-3}，D_c 爲雲滴直徑，

$$D_c = \left(\frac{1.91\, \bar{\rho} q_c}{\rho_w N_c} \right)^{0.33}$$

N_c 爲雲滴總集中數取 50 cm^{-3}，此值爲海洋性積雲典型的值（ Rogers, 1976 ）。

雲冰藉重霜化後轉換成冰珠其轉換率

$$P_{tg} = \max \left[P_{ri} - \left(\frac{N_i}{\bar{\rho}} \right) C_m ,\ 0 \right]$$

這裏 C_m 取 1.0×10^{-6}g s^{-1} 。

冰珠的凝固率及收集雨滴的產生率分別爲

$$P_{fg} = 6.5 \times 10^3 \left(\frac{\bar{\rho}}{\rho_w} \right)^{0.125} N_i q_r{}^{1.625}$$

$$P_{cg} = 0.52\, N_{tg} \mid \overline{V}_r - \overline{V}_g \mid \left[84.6 \left(\frac{\bar{\rho}}{\rho_w} \right)^{0.5} q_r{}^{1.5} + 1.4 \left(\frac{\bar{\rho}}{\rho_g N_{tg}} \right)^{0.67} \times \right.$$
$$\left. q_r q_g{}^{0.67} + 13.8 (\rho_g N_{tg})^{-0.33} \bar{\rho}^{0.58} \rho_w{}^{-0.25} q_r{}^{1.25} q_g{}^{0.33} \right] \qquad (29)$$

其中雨滴和冰珠的終端速度 V_r，V_g 由(13)及(23)求得。

當溫度高於凝固點（ 0 ℃ ）時，雲冰立即熔解 P_{mi}。至於冰珠的熔解率 P_{mg} 根據 Wisner et al.（1972）的研究，主要包含兩種機制：(1)空氣的熱傳導以及(2)水汽在冰珠面上凝結釋放潛熱。其公式爲

$$P_{mg} = -\frac{1}{L_f} \left[\kappa (T - 273.16) + \phi L \bar{\rho} (q_v - q_{si}) \right] \left[K_{1g} + K_{2g} q_g{}^{0.25} \right] \times$$
$$q_g{}^{0.33} - \frac{c_w}{L_f} (T - 273.16) (P_{cg} + P_{rg})$$

c_w 是定壓下水汽的比熱，而 q_{vs} 爲飽和水汽混合比，根據 Tetens 公式求得：

$$q_{vs} = \frac{3.799}{\bar{\rho}} \exp \left[\frac{17.2694 (T - 273.16)}{T - 35.86} \right]$$

式中 P_{cg} 和 P_{rg} 代表溫度高於凝固點時，冰珠收集到暖雲滴和暖雨滴的熔解分布，此熔解率爲雨滴生成的一個來源，其值分別由(28)和(29)式求得。

4. 結果分析與討論

本研究利用熱帶標準大氣來起始冰相和無冰相兩種不同雲模式，其中冰相模式又分含雲冰及不含雲冰兩種。本節將就此三種模式的數值資料做結果分析，以探討[illegible]展過程上雲動力與雲微物理間的相互作用以及各微物理過程所可能扮演的角色。此外比較三種不同模式間的差異，以了解冰相結構對雲發展的重要性。

4[illegible]動力學與雲微物理

[illegible]3爲含雲冰模式中，中心軸各物理量的時空分布。其中 3 a 爲上升速度 w 的[illegible]，其單位爲 m sec^{-1}，其值可視爲對流雲強度的指標。由圖中可看出，最初[illegible]內，w 緩慢上升，雲頂上呈現一種有規則的振盪形式。此振盪乃由於雲頂上[illegible]和空氣上升絕熱冷却所產生的，因爲空氣未不飽和故不易產生雲。10分鐘[illegible]迅速增加。在21分鐘時值達到 14.6m sec^{-1}約在 4.8 公里附近。至於最大上

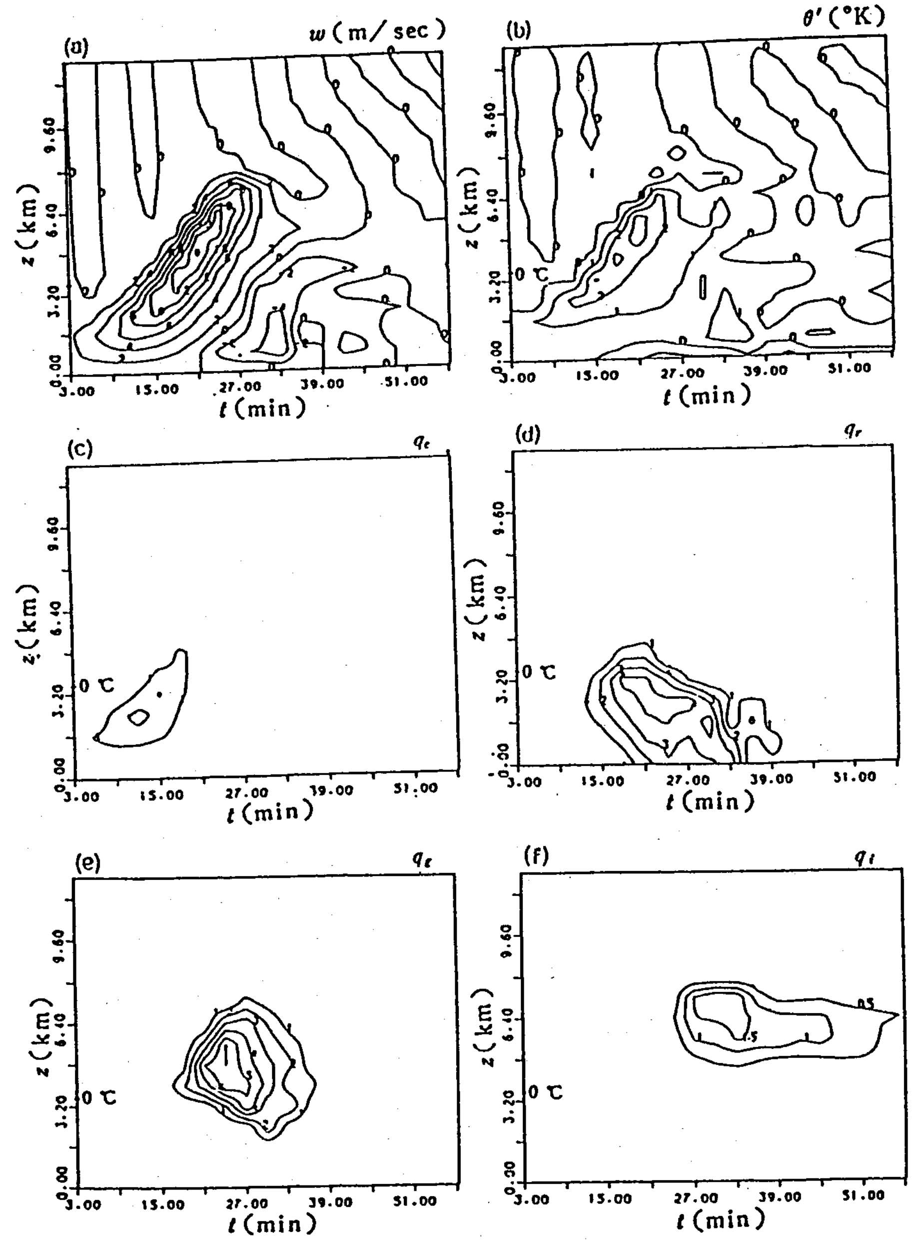

圖 3　模式中各物理量對中心軸的時空分布。單位：垂直速度 w（m／sec），間距 2 m／sec。位溫偏差 θ'（°K），間距 1 °K。混合比 q（g／kg），間距除 q_i 爲 0.5 g／kg 外其餘爲 1 g／kg。

升氣流高度則由開始的 1.6 公里迅速增加到27分鐘的 8 公里，其範圍侷限在一狹窄的區域內。此後迅速的減小而由下降氣流所取代，下降氣流的分布主要出現在熔解層下方。從21分鐘後其由低層向上發展至4.8 公里附近持續時間約18分鐘（21～39分），其最大值在33分鐘時達到－5.5 m／sec 。然後上升和下降氣流減少， 50分鐘後再成一無任何物理效應的振盪形式。

圖 3 b 爲位溫偏差值θ' 的分布，其分布形式不論最大值隨時間所達到的高度或是雲頂高度都和 w 近似。θ' 最大值 4.0°K 出現在21分鐘高度 4.8 公里的地方，其上升最大高度在27分鐘時到達 8 公里附近。27 分鐘後θ' 迅速減小，約在33分鐘出現另一較大值 2.2°K，此乃由於最大下降氣流所造成的絕熱增溫。然後在47分鐘時又再出現一較大值 1.3 °K，此乃受另一下降氣流所導致。此後θ' 不再有任何效應產生。至於負位溫值則出現在雲底 0.8 公里以下，其較大值出現在24分鐘、32 分鐘及42分鐘分別爲－1.55 °K 、－1.31 °K 及－1.39 °K 。此區域正是雨滴自雲底降落蒸發冷却的結果（圖 3 d ）。

圖 3 c 和圖 3 d 分別爲雲滴混合比（q_c）及雨滴混合比（q_r）的分布，其單位爲 g kg^{-1}。由圖可看出 q_c 和 q_r 主要出現在熔解層（ 0 ℃ ）以下，少部份出現在上方；q_c 形成於前 18 分鐘，其最大值 2.4 g kg^{-1} 出現在 12 分鐘 2.4公里附近，然後迅速減小消失。至於 q_r 的分布則主要出現在 12～40 分鐘之間，其較大值（≥ 4 g kg^{-1}）出現時間約 18～30 分之間而高度在 2.7～1.6 公里之間，其中最大值 4.6 g kg^{-1} 出現在 27 分鐘 2.4 公里附近。至於地面最大雨滴含量出現在 33 分鐘值爲 3.6 g kg^{-1}。這顯示出雨滴最大含量及所在高度的區域隨雨滴降落而逐漸減小，然而[illegible]分鐘附近雨滴出現另一較高的值 2.2 g kg^{-1} ，這主要是由高層冰粒子降落熔[illegible]所產生。

圖 3 e 和 3 f 分別爲冰珠（q_g）和雲冰（q_i）的分布圖，單位 g kg^{-1} 。由圖[illegible]出 q_g 主要集中在對流雲的中央，其高度約在 1.6～7.6 公里之間而持續時間約[illegible]（15～39 分），其最大值 6.0 g kg^{-1} 出現在 24 分高度 4.8～5.6 公里之[illegible]也就是 w_{max} 和 $θ'_{max}$ 出現的地方。這顯示出水質因凝結或凍結釋放潛熱增加雲

內環境間的位溫差，使得雲向上成長而增加冰珠的含量。當後者達到最大時，由於本身重量所產生的拖曳力使得上升氣流迅速減小，而冰珠也因降落蒸發熔解增加雨滴含量而迅速減少。於39分鐘後其含量小於 0.1 g kg^{-1}。

至於雲冰則出現在24分鐘以後，高度在0℃層以上，其最大值 1.94 g kg^{-1} 出現在 28 分鐘，高度 7.2 公里的地方。

有關固態水（$q_g + q_i$）的分布，其最大值 6.2 g kg^{-1} 出現在 24 分鐘高度 5.6 公里附近，主要形成時間在 13～47 分鐘之間。

降水粒子（$q_r + q_g$）的分布，其最大值 6.1 g kg^{-1} 出現時間和高度與固態水同在 24 分鐘 5.6 公里的地方，其 1.0 g kg^{-1} 等值線向上伸展到 7.2 公里附近。

由以上分析顯示，雲的生命期可分成發展期、成熟期和消散期等三個階段，其出現時間分別爲 0～15分，15～35分，35～50分。雲在發展階段因水汽凝結作用，釋放潛熱使得上升速度 w 和最大位溫差θ'向上增加，15分鐘後雨滴因本身重量所產生的拖曳力大於上升速度而降落至雲底。當雨滴開始由雲底降至地面時，雲已由發展階段進入成熟階段。在此階段由於上升氣流的高度已通過熔解層，故 w 和θ'能再度藉相變化所釋放的潛熱，向上伸展到 8 公里附近。此時冰珠含量因凍結效應，由 15 分鐘 0.1 g kg^{-1} 迅速增加到 24 分鐘的 6.0 g kg^{-1}，由於冰珠含量的增加，所產生的拖曳力隨時間迅速減弱雲內上升氣流而增強雲底之下降氣流。27分鐘後上升速度減小使得雲不再向上發展，而雲下則因降水粒子降落造成蒸發冷却，使得下降氣流由低層向上伸展至4.8 公里附近。此時由於雲內皆由下降氣流所控制致使低層水汽被切斷而無法繼續供應雲成長機制，故雲開始由成熟階段進入消散階段。

由圖 3 可知，雲生命期內的動力結構和熱量的分布有著密切關係，因此有關雲內熱量的源和滙的討論，對由浮力所產生的運動而言是非常重要的。

另外，我們也計算了不同微物理過程在雲生命期中對溫度變化率的貢獻，研究結果表明：

(1)在雲發展至成熟階段，這期間水汽的凝結率（0.05℃ sec^{-1}）以及冰珠的凍結率（0.07℃ sec^{-1}）扮演著重要角色。而冰珠的熔解率、昇華率（－0.02℃

sec^{-1}）與雨滴的蒸發率（－0.016℃ sec^{-1}）則對雲的衰減具有決定性作用。

(2)雲冰的沈積與昇華效應主要出現在消散期雲頂附近，其分布呈振盪形式，此現象和雲頂上方絕熱冷却、增溫有關。

(3)在熔解層上方，雲滴的蒸發成長冰珠（P_{dg}）釋放昇華潛熱（0.01℃ sec^{-1}）以及雨滴被冰珠收集（P_{cg}）釋放凝固熱的冰相微物理過程，對於雲的發展非常的重要。

有關對流雲成熟期與消散期的空間分布如圖 4a和4b 所示。圖 4 a 代表25分鐘時雲的分布，由圖中可看出雲主要集中在中心軸附近。圖中虛線代表固態水含量（$q_g + q_i$），大部份出現在 0℃層的上方，最大值爲6.09 g kg^{-1}。實線代表液態水含量，其分布主要位於 0℃層下方，最大值爲 4.2 g kg^{-1}，其大於 0.1 g kg^{-1} 的半徑約爲 1.6 公里。

圖 4 b 爲45分鐘時雲的分布。由圖顯示出，位於中心軸附近液態水的分布值很小爲 0.47 g kg^{-1}，固態水則出現在離中心軸 9.6 公里高度 5.6 公里附近，值爲 0.7 g kg^{-1}，此現象乃平流的結果。

由圖 4 分析顯示雲在成熟期時其結構非常的完整，在消散期時則非常的鬆散。

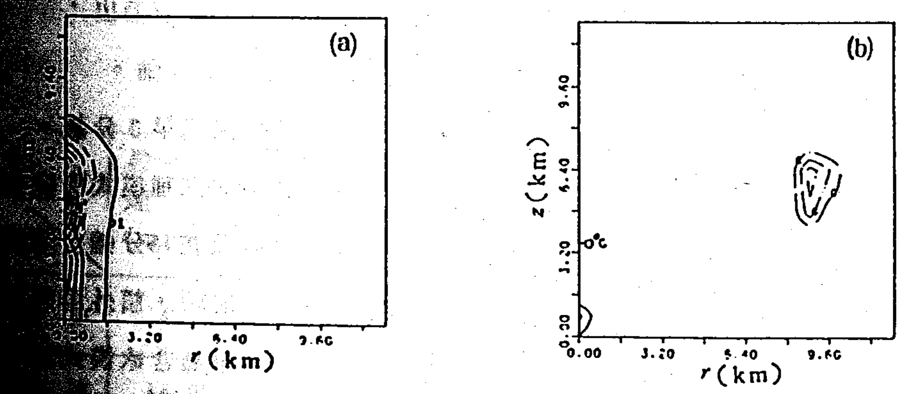

[illegible]在25分鐘時(a)和在45分鐘時(b)，對流雲的空間分布。單位：[illegible] g／kg，間距 1 g／kg，實線爲液態水含量，虛線爲固態水含量。

4.2. 比較三種不同模式的差異

在本節中將就含雲冰(A)不含雲冰(B)以及無冰(C)等三種不同模式的模擬結果做分析比較，以探討冰相結構在雲發展過程上所可能扮演的角色。

圖 5 爲B模式中心軸各物理量的時空分布。由圖顯示出各物理量的分布形式和A模式所模擬的結果（圖 3 ）類似；唯較明顯不同的是在B模式中，下降氣流的強度 $-6.2\,\mathrm{m\ sec^{-1}}$ 比A模式 $-5.5\,\mathrm{m\ sec^{-1}}$ 來得大，且地面降水時間及降水量也比A模式持續得長且大，此外冰珠的最大含量 $6.2\,\mathrm{g\ kg^{-1}}$ 也比A模式 $6.0\,\mathrm{g\ kg^{-1}}$ 大。

此結果顯示出(1)如果雲內不考慮雲冰則將增加過冷雲滴被冰珠收集的效應，使得冰珠因含量增加而加強下降氣流強度及降水量。(2)由A模式所模擬的結果，我們知道雲冰的含量在整個模擬過程中值非常的小，故其對雲發展的效應較不顯著，因此如不考慮雲冰則差異不大，然對發展較旺盛的風暴而言，差異將會加大。

圖 6 爲C模式中心軸各物理量的分布。由圖中仍可看出雲在不同階段的生命期，其分布形式雖和A，B模式類似，然在強度、雲頂高度以及降水時間的分布方面仍有極大的不同。

圖 7 爲三種不同模式中心軸 w_{max}，θ'_{max} 的趨勢變化，由圖中可看出：

(1)含冰對流強度（ $14.6\,\mathrm{m\ sec^{-1}}$ ）比不含冰（ $13.7\,\mathrm{m\ sec^{-1}}$ ）強。

(2)不含冰最大值出現時間（18分）比含冰最大值（21分）出現早 3 分鐘。

此外，由圖 3 、圖 5 、圖 6 和圖 7 ，我們亦發現在15分鐘前三種模式所模擬的結果並無顯著不同，而15分鐘後 w 和 θ' 迅速增加，這主要是因爲在15分鐘前雲頂高度未超過 0 ℃層，而無冰粒子產生。15分鐘後當雲頂通過 0 ℃層時，額外潛熱釋放使得雲因浮力作用向上加速運動而產生較大的 θ'_{max} 及 w_{max}。雖然含冰模式比不含冰的對流強度大，但由圖 8 可看出其產生的總降水量及降水時間却比較小。這主要是含冰模式衰減的較早。至於下降氣流以及雲頂高度的差異，由圖 3 a ，5 a 以及 6 a 可看出不含冰下降氣流強度（ $-4.1\,\mathrm{m\ sec^{-1}}$ ）以及雲頂高度（ 7 公里）都比含冰模式小，如表 1 所示。

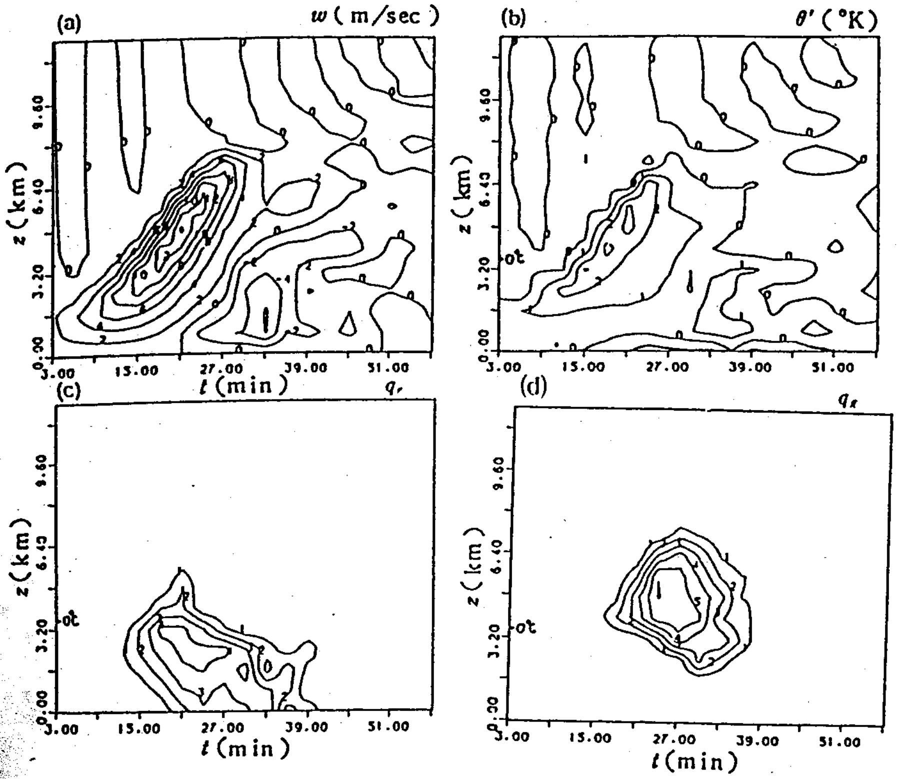

圖 5 無雲冰模式對中心軸各物理量的時空分布。單位：w（m／sec），間距 2 m／sec。θ'（°K），間距 1 °K。q（g／kg），間距 1 g／kg。

表 1　不同模式間各物理量的差異

物理量 ＼ 式名稱	最大上升速度 (m／sec)	最大下降速度 (m／sec)	最大位溫偏差 (°K)	雲頂高度 (km)	中心軸降水強度 (mm／hr)	中心軸總降水量 (mm)
[illegible]雲冰	14.6	－5.5	＋4.0	8.0	0.56	0.10
[illegible]雲冰	14.65	－6.2	＋3.0	8.0	0.63	0.11
[illegible]冰相	13.7	－4.1	＋3.1	7.0	0.45	0.12

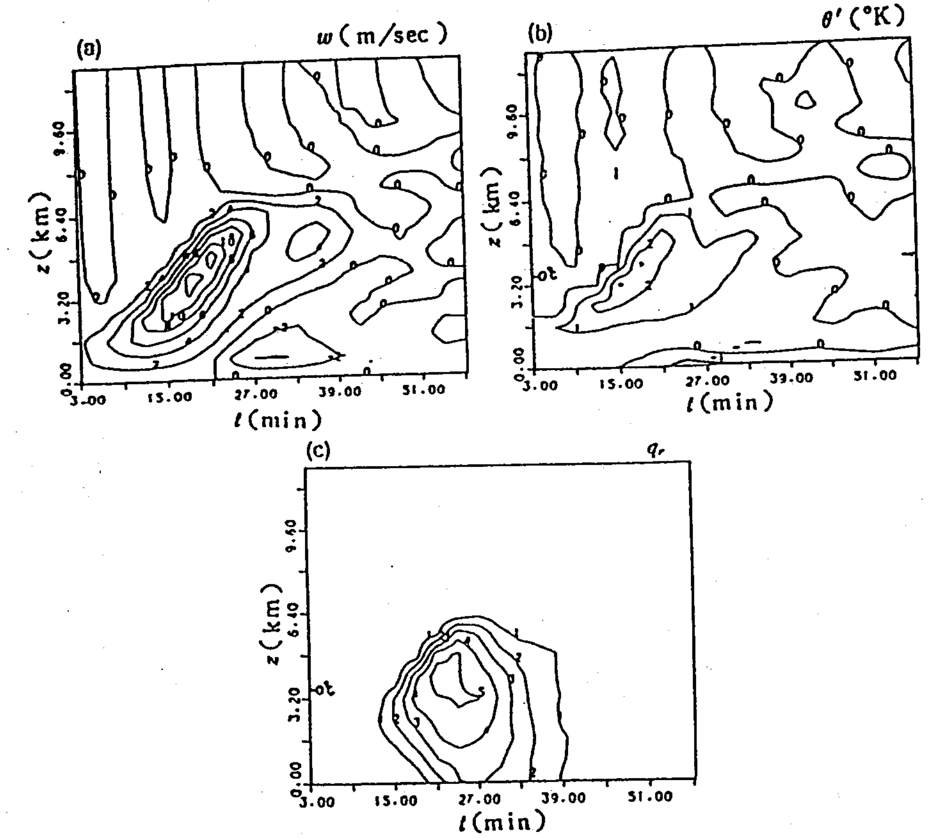

圖 6　無冰相模式對中心軸各物理量的時空分布。單位：w (m／sec)，間距 2 m／sec。θ' (°K)，間距 1 °K。q (g／kg)，間距 1 g／kg。

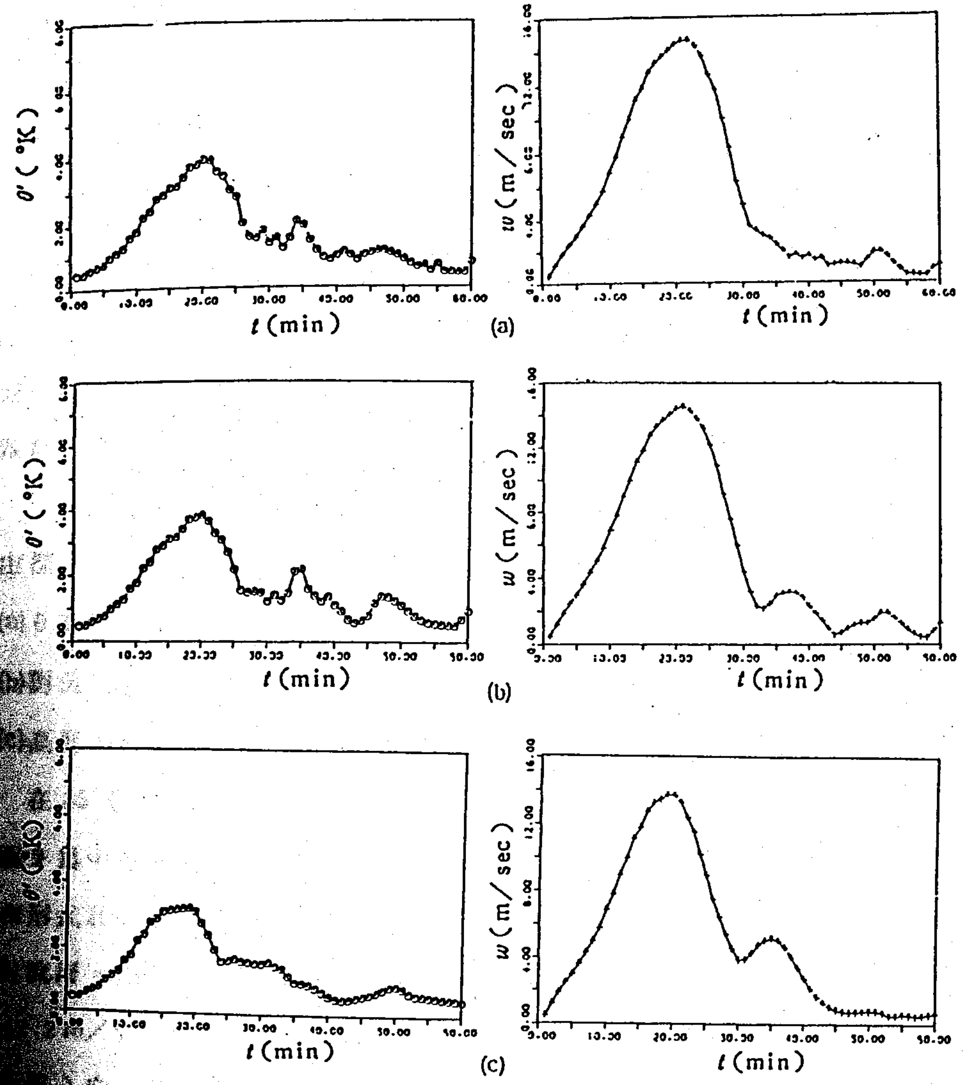

圖7　三種不同模式對中心軸 w_{max}，θ'_{max} 的趨勢變化。(a)含雲冰模式。(b)無雲冰模式。(c)無冰相模式。

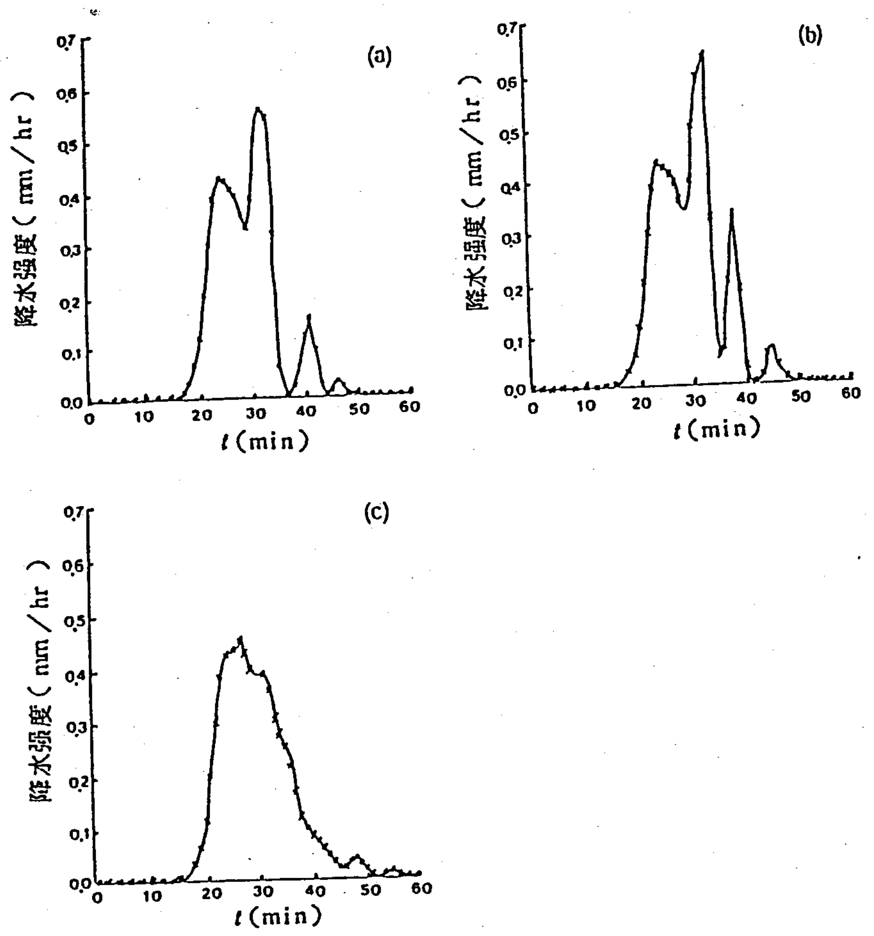

圖 8　三種不同模式地面降水強度的趨勢變化。(a)含雲冰模式。(b)無雲冰模式。(c)無冰相模式。

由以上比較結果顯示在深對流雲中，如果模式中忽略冰相結構將會高估降水量而低估氣流強度。

43. 個案模擬

我們都知道任何大氣模式最好的試驗是和它所模擬的實驗觀測現象做比較，然後由比較結果得出某些結論以做爲模式的改進或是提供模擬資料以支持實驗的進行。因此本文特選取 75 年 8 月 11 日 1200 Z 高雄機場有陣雨或雷雨報告時位於東港的探空資料做爲對流雲發生時的周圍環境條件，以探討模式對實際大氣的模擬能力，進而做爲今後改進模式缺點的參考。以下將討論這個個案的模擬結果與觀測上的比較。

由探空資料得知

[illegible]0 ℃層在 5.2 公里附近而 5.7 公里以下屬於條件 不穩定層。

[illegible]流凝結面（CCL）高度 1 公里，雲頂高度 9.5 公里。

[illegible]1.8 至 4.8 公里間之中對流層相對濕度很小，而近地面相對濕度很大約 85 至 95 %之間。

[illegible]中心軸各物理量的時空分布圖。其中圖 9 a 爲垂直速度（ w ）的分布，[illegible]和圖 3 a 最大不同是明顯的下降運動出現在中高對流層而非圖 3 a 出現[illegible]由圖中得知上升氣流所達到的最大高度約在 8.8 公里左右，最大上升[illegible]/sec 出現在 24 分鐘 5.6 公里的地方，而下降速度則由13分鐘的雲底（[illegible]向上伸展至 5.6 公里，其最大值－5.1 m／sec 出現在 33 分鐘 4.8公里附[illegible]以後上升、下降速度減小，54分鐘後變成無任何物理效應的振盪形式。[illegible]位溫偏差值θ'的分布。其分布形式和圖 3 b 最大不同的是中對流層出[illegible]且持續時間非常的長約36分鐘（ 19至55分），至於大的正θ'值則主要[illegible]附近。此結果說明了當環境水汽含量的垂直分布呈不規則時，最大位溫[illegible]垂直速度（ w ）的分布將和標準熱帶大氣所產生的分布形式不一樣。[illegible]對流層濕度很小，導致所有降水性粒子因蒸發冷卻而在該處產生大的

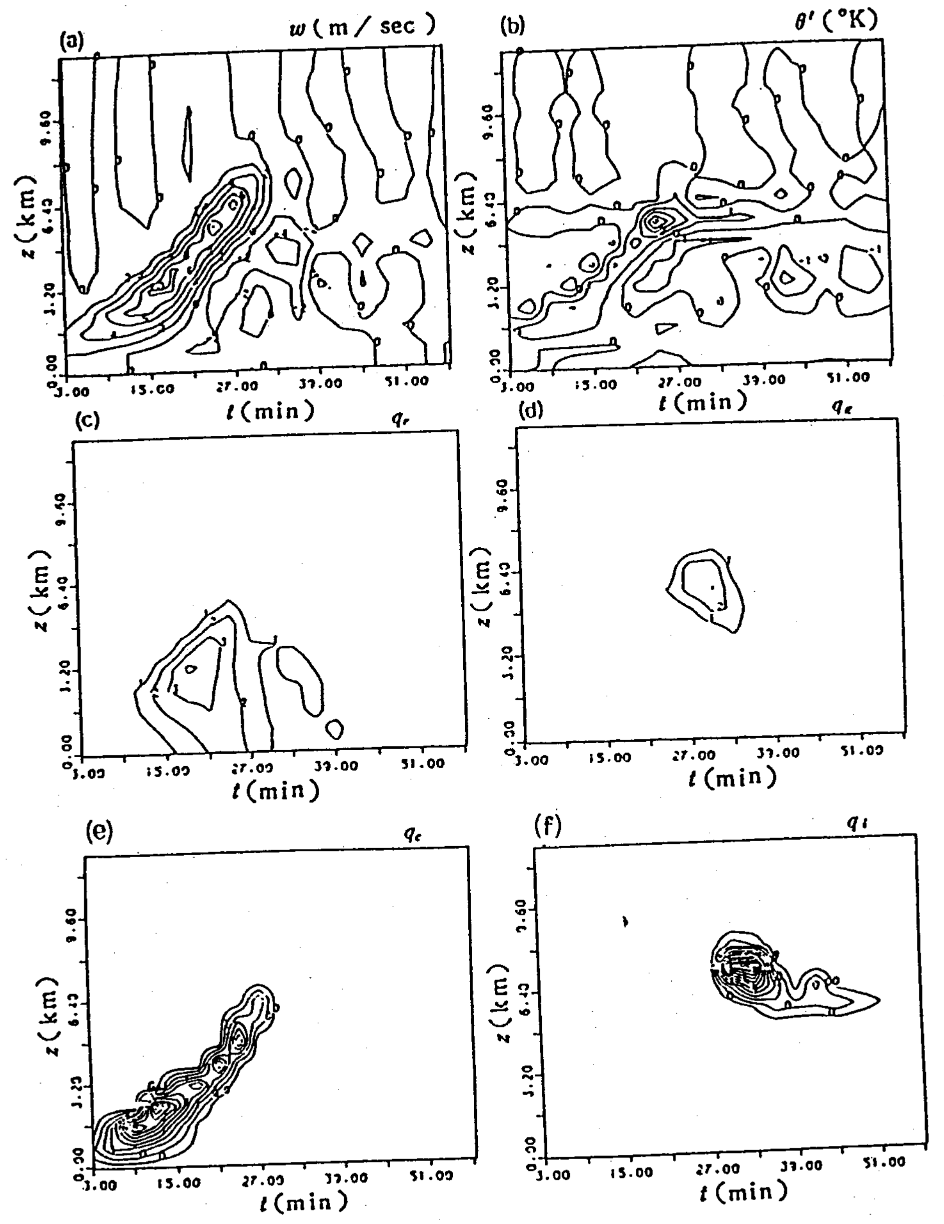

圖 9　74年 8 月11日東港探空資料經模擬所得中心軸各物理量的時空分布。單位：垂直速度 w (m／sec)，間距 2 m／sec 。位溫偏差 θ′ (°K)，間距 1 °K 。混合比 q (g／kg)，間距除 q_c ，q_i 爲0.2 g／kg外，其餘爲 1 g／kg ，(a)垂直速度 (w) 。(b)位溫偏差 (θ′) 。(c)雨滴混合比 (q_r) 。(d)冰珠混合比 (q_g) 。(e)雲滴混合比 (q_c) 。(f)雲冰混合比 (q_i) 。

下降氣流（圖 9 a ）及大的負 θ′ 值，而低對流層除非下沈增溫大於蒸發冷却會產生微弱的上升運動外，將只有微弱的下降運動產生。至於 θ′ 集中在高層則和高層水汽含量大，凝結釋放潛熱有關。

圖 9 c 爲雨滴混合比（ q_r ）的分布。由圖得知 q_r 主要出現在 0 ℃層以下，其近地面分布時間約在15至39分之間，較大值有兩處，一處位於18分 3.2 公里地方，值爲 4.2 g／kg ，另一處位於 33 分 3.2 公里地方，值爲 1.8 g／kg 。

圖 9 d 爲冰珠混合比（ q_g ）的分布。由圖得知 q_g 的分布集中在雲的中央，最大值 3.0 g／kg 出現在30分鐘 5.6 公里地方，此處正爲 0 ℃層附近。

圖 9 e 爲雲滴混合比（ q_c ）的分布。由圖可看出雲滴主要出現在前27分鐘，其範圍隨時間由雲底（ 0.4 公里）向上伸展至 7 公里，最大值 2.3 g／kg 出現在 12 分鐘2.4 公里處。

圖9 f 爲雲冰混合比（ q_i ）的分布。由圖得知 q_i 主要出現在雲成熟期之後 0 ℃[illegible]2 公里）上方，其最大值 1.26 g／kg 出現在 33 分鐘 6.4 公里的地方。

[illegible]10爲中心軸地面降水強度的趨勢變化。由圖看出降水主要出現在10到50分之[illegible]中最大值 0.34 mm／hr 出現在25分鐘，這正是近地面最大下降運動出現的時[illegible]9 a ），次大值 0.13 mm／hr 出現在 41分鐘附近，這和冰珠下降熔解有關。

[illegible]上分析，可歸納出下列幾點比較：

[illegible]對流性雷雨雲的生命期約爲45分鐘，其發展、成熟、消散等三階段出現的[illegible]爲0～13分，13～39分，39～45分，與實際高雄機場觀測到 0 ～ 142 分的[illegible]很多，這可能是機場附近多胞雷雨發生的結果。

[illegible]雲的雲頂高度 8.8 公里與實際探空資料所得到的雲頂高度 9.5 公里差了[illegible]。

[illegible]機場逐時的累計雨量 1200 Z 爲 0.3 公厘， 1300 Z 爲 0.5 公厘，這和模式[illegible]降水強度每小時 0.4 公厘大致吻合。

[illegible]測資料的缺乏，有關雲的熱動力結構並無法比較，然由上面分析顯示此[illegible]的模擬上仍具有模擬能力，不過其中卻也隱含著某些缺點亟待做進一步

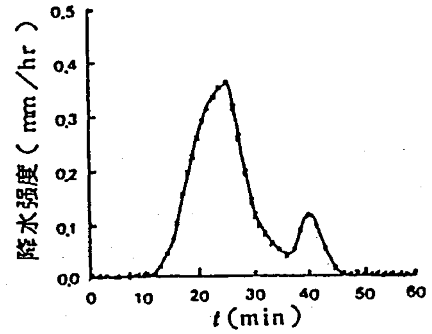

圖10　中心軸地面降水強度之趨勢變化

改進，以便更合理解釋雲的發展過程。

5. 結論與建議

本研究爲了探討對流雲在其發展生命期中，動力與雲微物理過程間的相互作用以及冰相結構在雲發展過程上所可能扮演的角色，曾對雲動力與雲微物理間的關係以及冰相模式和無冰相模式間的差異，做了詳盡的討論。由此討論我們得到下列幾項結論：

(1)雲微物理過程在整個雲生命史上和雲動力一樣扮演著相當重要的角色。

(2)在深對流雲模式中，考慮冰相結構經實驗證明比無冰相結構更接近實際觀測資料。也就是不會高估降水量而低估氣流強度。

(3)一個發展完整的熱帶對流雲，其高層幾乎是由冰粒子所涵蓋。

(4)雲在發展過程中，熔解潛熱的釋放將額外增加浮力效應，以加速雲內的對流運動。

(5)冰珠的凍結速度很快，導致它大部發生在對流雲的中央。

(6)較大的降雨強度和冰珠的含量有關，而冰珠的熔解則增加雨滴含量以減少低層對流運動。此結果將使雲因低層水汽供應被切斷而不再發展。

(7)冰相模式所模擬雲的生命期比無冰相模式短。

(8)模式中做了很多假設且不考慮垂直風切，因此所模擬的對流雲無法和實際觀測資料做比較，然所模擬的生命期以及降水過程和所觀測到的對流雲並不相矛盾。

(9)模式中使用了較大時空間距（$\Delta t = 20$ sec，$\Delta z = 400$ m），較容易產生較大的截斷誤差，如計算機能力許可的話，擬採用較小的時期間間距，以減小誤差，唯對流雲的生命期太短，故在本模式中還不至於影響太大。

(10)冰相結構對於雲的發展扮演重要角色，如要使其效應顯著，根據 Danielsen et al.（1972）的研究，冰雹的成長和上升速度、水滴的初始分布、相對濕度以及水滴的凝結高度有關。因此在水滴初始分布及環境相對濕度不變的情況下，可採取較大位溫偏差值的熱胞，以增加初始上升速度。

(11)爲了解模式的模擬能力，應以實際探空資料做爲模式的初始場，並利用更多的觀測資料以改善模式的缺點。

(12)本模式利用 Cotton et al.（1981)簡單冰相參數化來模擬熱帶單胞對流雲。[illegible]略了很多複雜的冰相過程，但是就整個模擬結果而言，仍就可看出雲內之冰[illegible]

[illegible]是在國家科學委員會專題計劃 NSC 76-0202-M 001-04 支持下完成的[illegible]究計算機中心提供計算機使用上的方便，本研究才得以順利完成全部計[illegible]特別表達衷心的謝意。

參考文獻

李華誕，1986：對流雲之數值模擬研究。國立台灣大學大氣科學研究所碩士論文。

Cotton, W. R., 1972: Numerical simulation of precipitation development in supercooled cumuli – Part II. *Mon. Wea. Rev.*, 100, 764–784.

Cotton, W. R., M. A. Stephens, T. Nehrkorn and G. J. Tripoli, 1981: Three-dimensional cloud/mesoscale model, Part II – An ice phase parameterization. Reports of the Colorado State University.

Danielsen, E. F., R. Bleck and D. A. Morris, 1972: Hail growth by stochastic collection in a cumulus model. *J. Atmos. Sci.*, 29, 135–155.

Deardorff, J. W., 1972: Numerical investigation of neutral and unstable planetary boundary layers. *J. Atmos. Sci.*, 29, 91–115.

Fletcher, N. H., 1962: *The Physics of Rainclouds.* Cambridge University Press, England, 390 pp.

Hirsch, J. H., 1971: Computer Modeling of Cumulus Cloud during Project Cloud Catcher. Rep. 71-7, Institute of Atmospheric Sciences, South Dakota School of Mines and Technology, 61 pp.

Hobbs, P. V., L. F. Radke, J. D. Locatelli, D. G. Atkinson, C. E. Roberson, R. R. Weiss, F. M. Turner and R. R. Brown, 1972: Contributions from the Cloud Physics Group, Research Report VII, Dept. of Atmos. Sci., Univ. of Wash., Seattle, 293 pp.

Hsie, E.-Y., R. D. Farley and H. D. Orville, 1980: Numerical simulation of ice-phase convective cloud seeding. *J. Appl. Meteor.*, 19, 950-977.

Kachurin, L. G., N. D. Artemyeva, A. T. Kartsivadze, S. Stoyanov and M. Tekle, 1973: Simulation of the natural process of hail formation and its transformation under the influence of artificial crystallization. *Proc. WMO/IAMAP Sci. Conf. Weather Modification*, Tashkent, USSR, 1-7 October 1973, WMO 399, 231-237.

Kessler, E., 1969: On the distribution and continuity of water substance in atmospheric circulations. *Meteor. Monogr.*, 10, No. 32, 84 pp.

Koenig, L. R., and F. W. Murray, 1976: Ice-bearing cumulus cloud evolution: Numerical simulation and general comparison against observations. *J. Appl. Meteor.*, 15, 747-762.

Lin, Y. L., R. D. Farley and H. D. Orville, 1983: Bulk parameterization of the snow field in a cloud model. *J. Climate Appl. Meteor.*, 22, 1065-1092.

Locatelli, J. D. and P. V. Hobbs, 1974: Fall speeds and masses of solid precipitation particles. *J. Geophys. Res.*, 79, 2185-2197.

Marshall, J. S., and W. M. Palmer, 1948: The distribution of raindrops with size. *J. Meteor.*, 5, 165-166.

Malkus, J. S., and G. Witt, 1959: The evolution of a convective element: A numerical calculation. *The Atmosphere and the Sea in Motion*, Rockfeller Institute Press and Oxford University Press, New York, 425-439.

Murray, F. W., 1967: On the computation of saturation vapor pressure. *J. Appl. Meteor.*, 6, 203-204.

Murray, F. W., 1970: Numerical models of a tropical cumulus cloud with bilateral and axial symmetry. *Mon. Wea. Rev.*, 98, 14-28.

[illegible] Y., 1963: The evolution of a moist convective element in a shallow, conditionally unstable atmosphere: A numerical calculation. *J. Atmos. Sci.*, 20, 407-424.

[illegible] Y., and T. Takahashi, 1971: Numerical simulation of the life cycle of a thunderstorm cell. *Mon. Wea. Rev.*, 99, 895-911.

[illegible] Y., and T. Takahashi, 1973: The development of warm rain in a cumulus model. *J. Atmos. Sci.*, 30, 262-277.

[illegible] H. D., L. J. Sloan and C. G. Myers, 1975: The dynamics and thermodynamics of precipitation loading. *Pure Appl. Geophys.*, 113, 983-1004.

[illegible] H. D., and F. J. Kopp, 1977: Numerical simulation of the life history of a hailstorm. *J. Atmos. Sci.*, 34, 1596-1618.

[illegible] D., and J.-M. Chen, 1982: Effects of cloud seeding, latent heat of fusion [illegible] condensate loading on cloud dynamics and precipitation evolution: A numerical study. *J. Atmos. Sci.*, 39, 2807-2827.

Rogers, R. R., 1976: *A Short Course in Cloud Physics.* Pergamon Press, New York, 227 pp.

Simpson, J., and V. Wiggert, 1969: Models of precipitating cumulus towers. *Mon. Wea. Rev.*, 97, 471-489.

Soong, S. T., and Y. Ogura, 1973: A comparison between axisymmetric and slab-symmetric cumulus cloud models. *J. Atmos. Sci.*, 30, 879-893.

Soong, S. T., and Y. Ogura, 1980: Response of tradewind cumuli to large-scale processes. *J. Atmos. Sci.*, 37, 2035-2050.

Soong, S. T., and Y. Ogura, 1982: A numerical study of cloud clusters as a scale interaction problem. *WMO Programme on Research in Tropical Meteorology*, Extended Abstracts of Papers presented at the MST/JMA/WMO/AMS, 115-116.

Takahashi, T. 1975: Tropical showers in an axisymmetric cloud model. *J. Atmos. Sci.*, 32, 1318-1330.

Takahashi, T., 1976: Hail in an axisymmetric cloud model. *J. Atmos. Sci.*, 33, 1579-1601.

Takeda, T., 1971: Numerical simulation of a precipitating convective cloud. *J. Atmos. Sci.*, 28, 350-376.

Wilhelmson, R., 1974: The life cycle of a thunderstorm in three dimensions. *J. Atmos. Sci.*, 31, 1629-1651.

Wisner, C., H. D. Orville and C. Myers, 1972: A numerical model of a hail-bearing cloud. *J. Atmos. Sci.*, 29, 1160-1181.

THE SIMULATION AND APPLICATION OF A CONVECTIVE CLOUD MODEL

Kun-chou Wang
Civil Aeronautics Administration
Ministry of Communications

Chung-yi Tseng
Institute of Physics, Academia Sinica
Nankang, Taipei 11529, Taiwan

ABSTRACT

An axisymmetric convective cloud model is used to investigate the interaction of cloud dynamical and microphysical processes and the role played by the ice phase during the life cycle of a cloud. This model consists of conservative equations for momentum, energy and mass of air and water substance, which is solved by using a staggered grid and a modified upstream difference scheme. The model utilizes the bulk water microphysical parameterization technique to simulate the cloud formation and precipitation processes, including the liquid and solid phase parameterization proposed by Soong and Ogura and Cotton et al., respectively.

The results of the model integration show that the cloud formation and precipitation processes are simulated qualitatively by the model. In addition, the relative importance of various microphysical processes in relation to the cloud development can be perceived in this model. It is found that the condensation of water vapor and the glaciation of water drops play a dominant role during the developing stage. On the other hand, the melting of graupels and the evaporation of water drops are important in the decaying stage. Furthermore, the vertical velocity and cloud top height are larger in this model than in the model without the ice phase. The results indicate that the intensity of the air stream will be overestimated and the rainfall underestimated in a cloud model neglecting the ice phase process. The total energy is conserved in the simulation and the convertion and distribution of various forms of energy are also investigated.

VISCOUS EFFECTS ON HYPERSONIC FLOW OVER BLUNT BODIES*

Lai-Chen Chien and Ching Long Hsu+
Institute of Physics, Academia Sinica
Taipei, Taiwan 11529
Republic of China

Abstract

In order to consider the strong viscous effects of the hypersonic flow over blunt bodies, unsteady thin layer Navier-Stokes equations are solved using the explicit upwind second order predictor-corrector scheme. The flux vector is splitted into forward and backward contributions by the eigenvalues of the Jacobian matrix with non-negative and non-positive groups. The split flux contributions are then spatially difference according to one-sided upwind discretizations. No additional explicit dissipation terms are necessary in the scheme.

In this paper, the flow over blunt bodies in a hypersonic stream is studied. The results show that there are strong waves in the flow field. And the characteristics of the flow field such as density, pressure and temperature distribution are presented. The boundary layer is discenible in the velocity and temperature distribution over the flow field. The pressure coefficient and temperature distribution exhibit the viscous effects on the hypersonic flow over the blunt bodies. The computation results are compared with experiment work and existing solutions with satisfactory agreement.

---

* The research is supported by National Science Council, R.O.C. under the direction of Engineering Division, NSC79-0401E-008-19.

+ Graduate research assistant, Institute of Mechanical Engineering, Tamkang University.

I. INTRODUCTION

The investigation of blunt body flow has been pursued since the beginning of supersonic flight. The computation of hypersonic flow around blunt body is of increasing interest for the future development of spacecraft and hypersonic cruise aircraft. The hypersonic flow around blunt bodies is characterized by strong schock waves and expansions, embedded subsonic regions, and shock-boundary layer interactions with separation. To attack the flow problems, the Navier-Stokes equations solver is a powerful tool in investigating the aero- and aerothermo-dynamic characteristics of the space plane at hypersonic flight (Haenel and Schwane, 1980; Yamamoto and Kubo, 1989; Hueber, Pittman and Dalley, 1988; Li, 1985).

Recent developed computational fluid dynamics techniques played an important role in these hypersonic flow simulations and complex flow problems in various portions of the vehicles (Newberry, Dresser, Byerly and Biba, 1988; Yee, Klopfer and Montagne, 1988; Yamamoto, 1988).

Because of the complexity of the viscous effects and large amount of computational resources required, the inviscid or thin layer assumption are made to simplify [illegible] complication of the problems. Even so, the governing equations are nonlinear [illegible] mixed characteristics bounded by the bow shock. The viscous effect is confined [illegible] thin boundary layer. Some investigators incorporate the parabolized Navier-[illegible] formulation to predict the hypersonic flow characteristics.

The research on hypersonic blunt-body flow was commenced by the poineering [illegible] Moretti (1967) which introduced the shock fitting procedure and time dependent finite difference approach. Since then, the numerical techniques have [illegible] great progress because of the advances on the algorithm and computer perfor[illegible] The most significant ones are the finite volume scheme (Bizzi and Inouye, [illegible] Lamda scheme (Moretti, 1979) and flux vector splitting scheme (Steger and Warming, 1981).

[illegible] the investigation on hypersonic flow over blunt body, the strong viscous [illegible] on compressible boundary layer plays important role in aerodynamic characteristics. The Euler solution can not afford scientists to investigation the problems of interest. If the support is sufficiently enough, the solution of full Navier-Stokes equation with chemical non-equilibrium is recommended. Because of the limitation of computer resource, we incorporate the thin layer Navier-Stokes equation formulation in this study.

The thin layer Navier-Stokes (TLNS) equations are obtained by adding viscous terms on Euler equations (Baldwin and Lomax, 1978). TLNS keeps the viscous terms of normal component and characterizes the same wave like properties as Euler solver. The unsteady Euler equations are hyperbolic for all Mach numbers and the wave like solutions can be obtained using time marching procedures. According to the hyperbolic properties of the Euler equations, mathematicians developed a sound characteric theory to determine the directions of wave motion and boundary conditions. The delicate numerical methods such as Lamda, flux vector splitting and Osher upwind scheme (Chakravathy and Osher, 1983) are designed. The classical finite difference schemes has their meits, but they must pay more attention to the disspation and shock treatment in the complicate flow field.

The numerical solutions for hypersonic TLNS has been investigated by a lot of scientists. Schroder and Hanel (1987) solved the TLNS applying the vector splitting algorithm for Euler solver (Van Leer, 1982), and the central difference scheme for viscous terms.

According the characteristic theory, we can evaluate the eigenvalues and solve the Euler equation of hyperbolic-wave characters. Steger and Warming (1981) developed the flux vector splitting scheme by the eigenvalues. Another similar scheme is also devised by Van Leer (1982). The two flux vector splitting methods have been applied to solve the compressible flow of free stream Mach number $0.03 < M < 3$ and obtained excellent accurate solutions. For the case of Mach number greater than ten, the two schemes can not converge (Whitfield, 1983), because they are unable to handle the strong shock waves.

In this paper the flux vector splitting method is employed to study the hypersonic flow over blunt bodies. Equivalent to the Lamda scheme, the method weighted the direction of small disturbance wave in finite difference form. The similar transformation property of the hyperbolic type is also considered in solving the Euler

equations (Chien and Lai, 1989). According to the homogenity characteristics, the flux vector is splitted into forward and backward contributions by the eigenvalues of the Jacobian matrix of non-negative and non-positive groups. Without using shock fitting procedure, the shcok is automatically captured. So far as the viscous terms, the central difference scheme is applied. The method has been applied in investigating the viscous hypersonic flow (Benken and Roberts, 1986; Ruffin, 1988; and Reklis and Lambard, 1982).

In this study, the hypersonic flow over circle cylinder, cylinder-cone combination and sphere-cylinder combination are investigated. The flow properties are obtained by thin layer Navier-Stokes equations using flux split vector scheme. The flow properties over the flow field are thus obtained. The boundary layer effects on the bow shock location, pressure coefficient and Nusselt number distribution are discernible. The results are comared with the existing solutions and experiment works with satisfactory agreement.

II. THEORETICAL FORMULATION

The normalized two dimensional Navier-Stokes equations in fully conservative [illegible] can be written in Cartesian coordinates of Vector expression (Anderson and [illegible]son, 1989)

$$\frac{\partial Q}{\partial t}+\frac{\partial}{\partial x}(E - E_{\nu}) + \frac{\partial}{\partial y}(F - F_{\nu}) = 0 \quad , \tag{1}$$

where Q signifies the conserving variables, and Q vector in the present work is

$$Q = [\rho,\ \rho\mu,\ \rho v,\ e]^T \quad , \tag{2}$$

where u and v are x- and y- components of the velocity, ρ and e are the density and [illegible] energy respectively. E and F are are x- and y- components of the flux [illegible] and E_ν and F_ν are correspondent components of the viscous flux vectors.

[illegible] on the

The flux vectors E and F are

$$E = \begin{pmatrix} \rho u \\ \rho u^2 + p \\ \rho uv \\ (e+p)u \end{pmatrix} , \qquad F = \begin{pmatrix} \rho v \\ \rho uv \\ \rho v^2 + p \\ (e+p)v \end{pmatrix} . \tag{3}$$

the corresponding viscous flux vectors are

$$E_\nu = \frac{1}{Re} \begin{pmatrix} 0 \\ \tau_{xx} \\ \tau_{yx} \\ \beta_x \end{pmatrix} , \qquad F_\nu = \frac{1}{Re} \begin{pmatrix} 0 \\ \tau_{xy} \\ \tau_{yy} \\ \beta_y \end{pmatrix} . \tag{4}$$

In the above expressions, the stress and heat flux terms are expressed by

$$\tau_{xx} = \frac{2}{3} u \left(2\frac{\partial u}{\partial x} - \frac{\partial v}{\partial y}\right) , \tag{5a}$$

$$\tau_{yy} = \frac{2}{3} u \left(2\frac{\partial v}{\partial u} - \frac{\partial u}{\partial x}\right) , \tag{5b}$$

$$\tau_{xy} = \tau_{yx} = \mu\left(\frac{\partial u}{\partial y} + \frac{\partial v}{\partial x}\right) , \tag{5c}$$

$$\beta_x = \frac{\gamma \mu \partial e_I}{Pr \partial x} + u\tau_{xx} + v\tau_{xy} , \tag{5d}$$

$$\beta_y = \frac{\gamma \mu e_I}{Pr\, \partial y} + u\tau_{yx} + v\tau_{yy} , \tag{5e}$$

and

$$e_I = \frac{e}{\rho} - \frac{1}{2}(u^2 + v^2) . \tag{5f}$$

The equation of state for a calorically perfect gas

$$p = (\gamma - 1)\left[e - \frac{1}{2}\rho\,(u^2 + v^2)\right] \tag{6}$$

enables the closure the system of governing equations.

In order to have finner meshes in the region where the flow properties vary

singnificantly and in the neighborhood of the body surface with large curvature, mesh generation procedure must be applied to transform the physical plane into computation plane obtaining the grids required. The full Navier-Stokes equation (1) can be transformed from the Cartesian coordinate system into a generalized boundary conforming coordinate system. The transformation relating the physical and computational space is

$$\tau = t, \ \xi = \xi(x, y) \ , \ \eta = \eta(x, y) \tag{7}$$

The transformation matrices are given by

$$J = \begin{pmatrix} x_\xi & x_\eta \\ y_\xi & y_\eta \end{pmatrix} , \qquad J^{-1} = \begin{pmatrix} \xi_x & \xi_y \\ \eta_x & \eta_y \end{pmatrix} = \frac{1}{h} \begin{pmatrix} y_\eta & -y_\eta \\ -y_\xi & y_\xi \end{pmatrix} \tag{8}$$

where h is the determinant of the matrix. The transformation is chosen such that the domain in the computational space is rectangular in shape with a regular uniform mesh, and is obtained by numerical solving the following system of elliptic partical differential equations,

$$\alpha x_{\xi\xi} - 2\beta x_{\xi\eta} + \gamma x_{\eta\eta} + J^2 (P x_\xi + R x_\eta) = 0 \tag{9a}$$

$$\alpha y_{\xi\xi} - 2\beta y_{\xi\eta} + \gamma y_{\eta\eta} + J^2 (P y_\xi + R y_\eta) = 0 \tag{9b}$$

with the appropriate boundary conditions. In Eq. (9), α, β, γ are transformation coefficients

$$\alpha = x_\eta^2 + y_\eta^2 , \quad \beta = x_\xi x_\eta + y_\xi y_\eta , \quad \gamma = x_\xi^2 + y_\xi^2 \tag{10}$$

and the parameters P, R are user determined forcing functions which control grid point spacing on the interior of the physical plane. The grid system for sphere-cone combination in physical plane is shown in Figure 1.

Using the grid generation technique, we obtain the two dimensional Navier-Stokes equations in the computational space.

$$\frac{\partial \hat{Q}}{\partial \tau} + \frac{\partial}{\partial \xi}(\hat{E} - \hat{E}_\nu) + \frac{\partial}{\partial \eta}(\hat{F} - \hat{F}\nu) = \hat{S} \ . \tag{11}$$

The transformed conservative variable and flux vectors are of the following expressions,

$$\hat{Q} = h\,[\,\rho, \rho u, \rho v, e]^T \quad , \tag{12a}$$

$$\hat{E} = h\begin{pmatrix} \rho U \\ \rho u U + \xi_x P \\ \rho v U + \xi_y P \\ U(e+P) \end{pmatrix} \quad , \qquad \hat{F} = h\begin{pmatrix} \rho V \\ \rho u V + \xi_x P \\ \rho v V + \xi_y P \\ V(e+P) \end{pmatrix} \tag{12b,c}$$

where U and V are components of contravariant velocity defined as

$$U = \xi_x u + \xi_y v, \quad V = \eta_x u + \eta_y v \tag{13}$$

In equation (11), the viscous flux vectors are of the forms

$$\hat{E}_\nu = (Re\eta)^{-1}\begin{pmatrix} 0 \\ \xi_x \tau_{xx} + \xi_y \tau_{xy} \\ \xi_x \tau_{yx} + \xi_y \tau_{yy} \\ \xi_x \beta_x + \xi_y \beta_y \end{pmatrix} \qquad \hat{F}_\nu = (Re\eta)^{-1}\begin{pmatrix} 0 \\ \eta_x \tau_{xx} + \eta_y \tau_{xy} \\ \eta_x \tau_{yx} + \eta_y \tau_{yy} \\ \eta_x \beta_x + \eta_y \beta_y \end{pmatrix} \tag{14}$$

Equation (11) is the expression for unsteady two dimensional compressible Navier-Stokes equation in generalized coordinate system.

Because of the limitation of computer resources, it is hard for us to solve the Navier-Stokes without simplification. In the previous investigation, we try to solve the hypersonic flow over blunt bodies with Euler solver by neglecting the viscous

flux vector terms in governing equation (1) (Chien and Lai, 1989). Comparing the pressure distribution on the surface of the cylinder, we proved that the numerical values agree with the existing experiment data (Lyubimov and Rusanov, 1973) and Euler equations solution (Chakravathy and Osher, 1983) satisfactorily.

In hypersonic flow, the viscous boundary layer is thin and is of importance because of the determination of skin friction and skin temperature (Anderson, 1989). It is better to apply the full Navier-Stokes equation model in investigation. In this study, we incorporate thin layer Navier-Stokes equations model due to the limitation of computation resources. The equations in conservative vector form in generalized coordinates are:

$$\frac{\partial \hat{Q}}{\partial t} + \frac{\partial}{\partial \xi}\hat{E} + \frac{\partial}{\partial \eta}\hat{F} = \frac{1}{Re2\eta}\frac{\partial}{}S \tag{15}$$

where

$$S = \frac{1}{h}\begin{pmatrix} 0 \\ \alpha_1 \frac{\partial u}{\partial \eta} + \alpha_2 \frac{\partial v}{\partial \eta} \\ \alpha_2 \frac{\partial u}{\partial \eta} + \alpha_3 \frac{\partial v}{\partial \eta} \\ \alpha_4 \frac{\partial}{\partial \eta}\left(\frac{e}{\rho}\right) + \frac{\alpha_1 - \alpha_4}{2}\frac{\partial u^2}{\partial \eta} + \frac{\alpha_3 - \alpha_4}{2}\frac{\partial v^2}{\partial \eta} + \alpha_2 \frac{\partial uv}{\partial \eta} \end{pmatrix} \tag{16}$$

$$\alpha_1 = \mu\left(\frac{4}{3}\eta_x^2 + \eta_y^2\right) \tag{17a}$$

$$\alpha_2 = \frac{1}{3}\mu \eta_x \eta_y \tag{17b}$$

$$\alpha_3 = \mu\left(\eta_x^2 + \frac{4}{3}\eta_y^2\right) \tag{17c}$$

$$\alpha_4 = \gamma K(\eta_y^2 + \eta_y^2) \ . \tag{17d}$$

Equation (15) is thin layer Navier-Stokes equations in conservative form.

Solving the equations, we can capture the discontinuity phenomenon such as shock wave slip line and expansion fan. Using upwind scheme in the subsonic region with positive or negative eigenvalues, one can not obtain the convergent solution desired. The flux vector must be splitted into forward and backward contributions by the eigenvalues of the Jacobian matrix into non-negative and non-positive groups. The splitted method applied is that developed by Reklis and Lombard (1982), Grossman and Walters (1989) obtaing the satisfactory results.

Using the splitted scheme, one obtains the governing equation of the form

$$\frac{\partial Q}{\partial t}+\frac{\partial K}{\partial k}=0 \; , \tag{18}$$

where

$$K = K_1 + K_2 + K_3 \; , \tag{19}$$

$$K_1 = \lambda_k^1 h \frac{\gamma-1}{\gamma}[\rho \;\; \rho u \;\; \rho v \;\; \frac{\rho(u^2+v^2)}{2}]^T \; , \tag{20a}$$

$$K_2 = \lambda_k^3 \frac{h}{2\gamma}[\rho \;\; \rho u + \rho c k_x \;\; \rho v - \rho K_y \;\; e + P + \rho c\theta]^T \; , \tag{20b}$$

$$K_3 = \lambda_k^4 \frac{h}{2\gamma}[\rho \;\; \rho u - \rho c k_x \;\; \rho v - \rho c k_y \;\; e + P - \rho c\theta_k]^T \; , \tag{20c}$$

and

$K = E$, when $k = \xi$

$K = F$, when $k = \eta$

$\lambda_k^1 = \lambda_k^2 = k_x u + k_x v = \theta_k \; , \qquad \lambda_k^3 = \theta_k + c|\Delta k| \; ,$

$\lambda_k^4 = \theta_k - c|\Delta k| \; , \quad |\Delta k| = \sqrt{k_x^2 + k_y^2}$

$\theta_k = k_x u + k_y v \; , \quad k_i = k_i/|\Delta k| \; ,$ when $i = x$ or y

III. FLUX SPLIT VECTOR SCHEME

Having applied the splitted method, we can employ the different numerical scheme to solve the thin layer Navier-Stokes equations. The most popular algorithm is the predictor-corrector proposed by MacCormack. Beam and Warming (1976) extended the algorithm for the second order upwind predictor corrector method. Because the upwind scheme applied two procedures of one side difference, it can match the theory of characteristics. The technique utlized the forward or backward one side difference depending on the direction of the wave motion. Therefore, the method developed by Beam and Warming is incorporated in the numerical scheme.

Integrating the thin layer Navier-Stokes equation (15) with respect to control volume for the cell centered at (i,j), we have the difference form

$$\frac{\Delta\hat{Q}}{\Delta\tau}\Delta\xi\Delta\eta + (\hat{E}_{i+1/2,j} - E_{i-1/2,j})\Delta\eta + [(\hat{F}_{i,j+1/2} - \hat{F}_{i,j-1/2})$$

$$- Re^{-1}(S_{i,j+1/2} - S_{i,j-1/2})]\,\Delta\xi = 0 \; . \tag{21}$$

The numerical method handled is the finite volume of second order upwind scheme. To explain the scheme, consider the simple model equation

$$\frac{\partial u}{\partial t}+\frac{\partial F(u)}{\partial x}=0 \; . \tag{22}$$

The predictor for the second order upwind scheme is

$$U_i^{n+1} = u_i^n - \Delta t\frac{\Delta F_i^n}{\Delta x} \; . \tag{23}$$

And the corrector is

$$u_i^{n+1} = \frac{1}{2}(u_i^n + U_i^{n+1}) - \frac{\Delta t}{2\Delta x}(\Delta^2 F_i^n + \Delta_i^{n+1}) \; . \tag{24}$$

Where Δ is the backward difference operator, and $F_i^{n+1} = F(u_i^{n+1})$. Using the one point upwind extrapolation u_i for $u_{i+1/2}$ and u_{i-1} for $u_{i-1/2}$, one has the predictor for equation (22).

$$u_i^{n+1} = u_i^n - \frac{a\Delta t}{\Delta x}(u_i^n - u_{i-1}^n) \tag{25}$$

which is the same as Equation (23). Similarly, using the two point upwind expropolation, the finite volume corrector can be written as

$$u_i^{n+1} = u_i^n - 2u_{i-1}^n + u_{i-2}^n) + (u_i^n - u_{i-1}^n)] - \frac{\Delta t}{2}\frac{F_i^{n+1}}{\Delta x} \tag{26}$$

By Equation (23), we can put Equation (26) into the form of Equation (24) which is exactly the same form as Warming and Beam's corrector. The stability, dissipation and dispersion have been investigated by Warming and Beam, and extended to finite volume scheme.

Putting on the above analysis, into the numerical solution of thin layer Navier-Stokes equations, we have a complete scheme for two-dimensional unsteady hypersonic flow over blunt body with predictor

$$\begin{aligned}\hat{Q}_{ij}^{n+1} = \hat{Q}_{ij}^n - \Delta\tau_{ij} \sum_{l=1}^{3} [\hat{E}_1(\hat{Q}_{i+1/2,j}^n - \hat{E}_1(\hat{Q}_{i-1/2,j}^n) + \hat{F}_1(\hat{Q}_{i+1/2,j}^n) \\ - \hat{F}_1(Q_{i-1/2,j}^n) - Re^{-1}\left\{ S(\hat{Q}_{i,j+1/2}) - S(\hat{Q}_{i,j-1/2})\right\}]\end{aligned} \tag{27}$$

where the subscript 1 corresponds to one part of the split vector

$$\hat{Q}_{i+1/2,j}^n = \hat{Q}_{i,j}^n \;, \quad \text{when} \quad \lambda_{i+1/2,j} > 0 \tag{28a}$$

and

$$\hat{Q}_{i+1/2,j}^n = \hat{Q}_{i+1,j}^n \quad \text{when} \quad \lambda_{i+1/2,j} < 0 \tag{28b}$$

Similarly, $Q_{i-1/2,j}^n$, $Q_{i,j+1/2}^n$, $Q_{i,j-1/2}^n$ are managed by the same way. Whilst the difference scheme applied in viscous flux vector is central.

The correspondent corrector is of the form

$$\begin{aligned}\hat{Q}_{i,j}^{n+1} = Q_{i,j}^n - \frac{\Delta\tau_{i,j}}{2} \sum_{l=1}^{3} [\hat{E}_1(Q_{i+1/2,j}^n) - E_1(Q_{i-1/2,j}^n) + F_1(\hat{Q}_{i,j+1/2}^n) \\ - \hat{F}_1(Q_{i,j-1/2}^n) - \hat{E}_1(\hat{Q}_{i+1/2,j}^{n+1}) - \hat{E}_1(\hat{Q}_{i-1/2,j}^{n+1}) + F_1(\hat{Q}_{i,j+1/2}^{n+1}) \\ - \hat{F}_1(Q_{i,j-1/2}^{n+1}) - Re^{-1} \quad S(\hat{Q}_{i,i+1/2}) - S(\hat{Q}_{i,j-1/2}) \\ - Re^{-1}\left\{S(\hat{Q}_{i,j+1/2}) - S(\hat{Q}_{i,j-1/2})\right\}]\end{aligned} \tag{29}$$

where $\hat{Q}_{i+1/2,j}^{n+1}$ and other variables are determined in the same way as $\hat{Q}_{i+1/2,j}^n$ described in equation (29). And $Q_{i+1/2,j}^n$ is regulated by

$$\hat{Q}_{i+1/2,j}^n = 2\hat{Q}_{i,j}^n - \hat{Q}_{i-1,j}^n \;, \quad \text{when} \quad \lambda_{i+1/2,j} > 0 \tag{30a}$$

and

$$\hat{Q}_{i+1/2,j}^n = 2\hat{Q}_{i+1,j}^n - \hat{Q}_{i+2,j}^n \;, \quad \text{when} \quad \lambda_{i+1/2,j} < 0 \tag{30b}$$

Similar treatment is handled for the other variables.

The method described above is applied to solve the hypersonic flow over the blunt body. The upwind difference depends on the eigenvalues of sign positive or negative. The eigenvalues are computed at cell faces rather than cell centers. It is the average of the eigenvalues on the cell faces.

To accelerate convergence for steady state solution, the maximum allowable time step in each cell is used where CLF≤2. Wornom and Hafez (1986) investigated the local time step such that the time increment in every cell satisfies Von Neuman condition

$$\Delta\tau_\xi = \frac{CFL\Delta\xi}{MAX(\lambda_\xi^1)}, \qquad \Delta\tau_\eta = \frac{CFL\Delta\eta}{MAX(\lambda_\eta^1)} \tag{31}$$

and

$$\Delta\tau = \frac{\Delta\tau_\xi \cdot \Delta\tau_\eta}{\Delta\tau_\xi + \Delta\tau_\eta} \tag{32}$$

where $Max(\lambda_\xi^1)$ and $Max\ (\lambda_\eta^1)$ express the maximum eigenvalue in ξ and η direction respectively.

IV. INITIAL AND BOUNDARY CONDITIONS

The numerical solution of the problem considered is an initial-boundary value problem. The non-slip condition at the body surface specifies the boundary conditions

$$u = 0, \quad v = 0 \qquad at\ \xi = 0 \tag{33}$$

The pressure and density are determined by the eigenvalues discussed in the above section.

$$P_b = P_r \pm \rho_o c_o (k_x u_r + k_y v_r) \tag{34}$$

$$\rho_b = \rho_b + (P_b - P_r)/c_o^2 \tag{35}$$

where the subscript b represents the point of the boundary and r refers to the reference value. The minus and plus signs in equation (34) correspond to the location of the point r. The linearization point with subscript o is taken on the boundary.

For the characteristic variables at the inflow, the free stream is hypersonic. In this situation, all eigenvalues have the same sign. Because flow is coming into the computational domain, all flow variables are defined. Whilst at the outflow, the supesonic condition is also assigned. This is another situation where all eigenvalues have the same sign. Because flow is leaving the computational domain, all flow variables at the boundary must be obtained from the solution in the computational domain, and are extrapolated from inside of the computational domain to the boundary.

Besides the boundary conditions decribed in above paragraph, the initial values of variables concerned must be given in order to carry out the numerical integration.

The more reasonable initial conditions assigned, the faster convergence obtained. Therefore, the appropriate initial values employed to integrate the governing equations will reduce the computation time to obtain the convergent solution desired. If the initial conditions ultilized is poor enough, it will take more computation time to converge the accurate solution. This is the fortunate property of the thin layer Navier-Stokes equation that a numerical solution approaches analytic solution, if any, and its accuracy is probably acceptible after a few steps of compution (Crank, 1975). The initial conditions assigned for the problem are the free stream condition. The free stream variables normalized are specified at every points in the computation domain.

V. RESULTS AND DISCUSSION

The hypersonic flow over blunt bodies are present in this investigation. The cases of cylinder, cylinder-cone combination and sphere-cylinder combination are studied. Comparing with the existing solutions and experiment data, we conclude that the present study of thin layer parabolic Navier-Stokes solutions are more satisfactory agreement than those of Euler solver compared with the experiment.

In order to compare the investigation results of this study with those of experiment works, existing solution and previous developed Euler solver, the cases of Mach number 8, and Mach number 4 are investigated. At first, using the grid generation technique, we transform the physical plane into rectangular grid coordinate system by equations (9a) and (9b). Then, we solve the governing equations by flux vector splitting method. (Reklis and Lambard, 1982; Gross man and Walters, 1989) and obtained the solution. The velocity distribution over the flow field is shown in Figure 2. The velocity direction and magnitude reveal the existence of the bow shock. At the vicinity of the bow shock, the sharp deceleration and considerable deflection of the flow are depicted by the arrows. The shock location obtained by the computation, Figure 3, is compared with the existing Euler solution of Belotserkovskii (1958), experimental work (Kim, 1956) and the previous developed Euler solver (Chien and Lai, 1989). In Figure 3, we conclude that the present thin layer Navier-Stokes model agrees excellently with the experiment work expressed in solid line. In the neighborhood of the front stagnation point, the present study agrees with that of Euler solvers (Chien and Lai, 1989; Belotsekovskil, 1972). Whilst at the region where the boundary layer developed, the bow shock of the two solvers diverse. The bow shock with boundary layer considered displaced outward.

The boundary layer can be discerned in Figure 2. In the neighbor of the front stagnation point, the boundary is nil. Then it grows thicker and thicker along the cylinder surface from 0° to 75°. Then the boundary layer fully developed and the thickness remains in constant condition.

Figure 4 demonstrates the pressure distribution over the surface of the cylinder. There exists a maximum value at the front stagnation point. Then it decreases from the front to the top of the cylinder. The comparison is also shown. Not only the tendency, but also the numerical values agree with the experiment work satisfactorily (Kim, 1972). The pressure coefficient of viscous considered solution is higher than that of Euler Solver, because of the lower velocity of the Viscous flow resulting in the higher the pressure. The difference of C_p is more clearly observed in the region where boundary layer grows more discemible in Figure 2. The present viscous layer considered investigation agree. With that of experiment study of Kim.

The countour lines of isobar, isothermal and Mach number distribution over the flow field are shown in Figure 5, 6 and 7 respectively. The crip shock transition is clearly evident in this manner of portraying the results. The iso-lines clustered

into the thin region where the shock wave located. The lines also distributed closely in the boundary layer. The phenomena demoustrated the fact that the gradients of temperature and pressure are great in both shock and boundary layers. The bow shock is strong enough and the entropy changes across the shock is significant. For the hypersonic flow over the cylinder, the shock wave is curved, and the entropy jump will vary from point to point on the shock. Thus, the existence of the entropy gradient at the downstream of the shock induces strong vorticity in the inviscid flow field. The boundary layer embeded in the strong entropy layer, and its growth will be dominated by strong rotational flow (Anderson, 1989). The oscillation phenomena shown in our computation are induced by second order dispersion error.

The temperature distribution over the cylinder surface is indicated in Figure 8. Both TLNS and Euler solver show the maximum temperature at the neighbor of the front stagnation point, because the nil velocity at the stagnation point. Then both curves decrease along the cylinder surface, temperature distribution diminishes sharply for Euler solver, whilst that obtained by TLNS decreases gently because the existence of viscous boundary layer. This phenomena demonstrate that the influence of the convection heat transfer is significant. At the stagnation point, the small heat transfer results in the large temperature gradient, so does the temperature distribution.

In order to compare with our previous study (Chien and Lai, 1989), the case of free stream Mach number 8 is also investigated. The velocity pressure, temperature and Mach number distribution are almost similar to the phenomena for the case of $M_\infty = 4$ shown in the Figures 2, 5-7. The pressure distribution ont he cylinder surface is investigated. In previous study, we have compare our Euler solver with that developed by Chakravathy and Osher (1982). Figure 9 shows the present TLNS solver excellently agrees with the experiment work of Lynbimov and Rusanov (1973).

The second case investigated is this cae of hypersonic flow of free stream Mach number 8, Reynolds number 1.36×10^6 over a cylinder-cone combination. The cone with deflection angle 10 degrees. The stand-off position of the bow shock is $1.49r_o$, whilst that of cylinder is $1.44r_o$. The conclusion exactly agrees with that of

Lee and Loellbach (1989). The Mach number, temperature and pressure over the cylinder-cone distribution are shown in Figures 10-12. The patterns agree with those computed by Lee and Loellbach.

The third case of interested in the study is the hypersonic flow over an axisymmetric sphere-cylinder combination. Because of the complex geometry, the grid system generated using the boundary conforming coordinate is applied to obtain the grid desired, Figure 2. The flow field of free stream Mach number 25 and an angle of attack $\lambda = 20$ is shown in Figure 13. The boundary layer is discernible along the body surface. Because of the high angle of attack, the bow shock wave is near to the body at the windside than the leeside. Figure 14 and Figure 15 show the iso-bar and isothermal. From above figures, the sharpness of the transition at the windside is stronger than the leeside. The feature is agreed with that of existing solution (Peraire, Vahadati, Margan and Zienkiewiz, 1987). And the high temperature is produced at the front. In hypersonic speed, the temperature is enough to burn up the convectional material. Therefore, it is necessary to have additional thermal protection. The design of thermal protection is the most significant work of hypersonic vehicle.

VI. CONCLUSION AND RECOMMENDATION

Hypersonic flow over blunt body is investigated by solving the unsteady thin layer Navier-Stokes equations based on flux vector splitting method. The equations are cast in curvilinear coordinates and a finite volume discretized equations is used for handling arbitrary geometries. The discretized equations are solved using an explicit upwind second-order predictor-corrector scheme that is stable for a CFL of 2. No additional dissipation terms are included in the scheme. Local time stepping is used to accelerate convegence for steady-state problem. Characteristic variable boundary conditions are developed and applied in the farfield and at solid boundary surface. Numerical results are obtained and compared with data of experimental work and previous numerical solutions.

The cases of hypersonic flow over cylinder at $M_\infty = 4$ and 8, cylinder-cone combination at $M_\infty = 8$, and sphere-cylinder combination at $M_\infty = 24$ are investigated. The boundary layers are shown in the flow field. The computation results are more accurate than those obtained by Euler solver. Comparing the flow perperties with experiment data, we show that the agreements are excellent.

This is the preliminary study for the hypersonic flow over blunt bodies. In the future, the full Navier-Stokes equations with chemical reaction model is recommended because the strong viscous effect and high temperature effect must be considered (Tam and Li, 1990).

REFERENCE

1. Anderson, D. A. and Thompson, D. S. (1989). Plume interference study. UTA CFD Report 89-03.
2. Anderson, D. J. Jr. (1989). Hypersonic and high temperature gas dynamics. McGraw-Hill Book Company.
3. Baldwin B. S. and Lomax H. (1978). Thin layer approximation and algebraic model for separated tubulent flows. AIAA Paper 78-257.
4. Banken, G. J. and Roberts, D. W. (1986). A parabolized Navier-Stokes prediction of hypersonic window cooling. J. Spacecraft Rocket, Vol. 25, pp. 125-146.
5. Belotserkovskii, O. M. (1958). Flow past a circular cylinder with a detach shock wave. Vychislitel'noi Mat., Vol. 3, pp. 149-185.
6. Chakravarthy, S. R. and Osher, S. (1983). Numerical experiments with the Osher upwind scheme for the Euler equations. AIAA J., Vol. 21, pp. 1241-1248.
7. Chien, L. C. and Lai, C. M. (1989). Application of flux split vector scheme for hypersonic flow over blunt body. Numerical Methods in Thermal problems, Vol. 6, pp. 388-398.
8. Crank, J. (1975). The mathematics of diffusion. Clavendon Press, Oxford

Press.

9. Grossman, B. and Walter, R. W. (1989). Flux-split algorithm for multi-dimensional Euler equations with real gas. Computers and Fluids, Vol. 17, pp. 99-112.
10. Haenel, D. and Schwane, R. (1989). An implicit flux vector splitting scheme for computation of viscous hypersonic flow. AIAA Paper 89-0273.
11. Hueber, L., Pittman, J. and Dalley, A. (1988). Computation validation a parabolized Navier-Stokes solver on a sharpnose cone at hypersonic speeds. AIAA Paper 88-2566.
12. Kim, C. S. (1972). Experimental studies of supersonic flow past a circular cylinder. J. Phys. Soc. Japan, Vol. 11, pp. 439-445.
13. Lee K. D. and Loellbach J. M. (1989). Mapping technique for solution-adaptive grid control. AIAA Paper 89-2178.
14. Li, C. P. (1985). A three dimensional Navier-Stokes/Euler code for blunt body flow computation. NASA TM 58266.
15. Lyubimov, A. N. and Rusanov, V. V. (1973). Gas flows past blunt bodies. NASA-TT-F715.
16. Moretti, G. (1979). The Lammda scheme. Computers and Fluids, Vol. 7, pp. 191-205.
17. Moretti, G. and Bleich G. (1967). Three-dimensional flow around blunt bodies. AIAA J., Vol. 5, pp. 1557-1562.
18. Newberry, C. F., Dresserm M. S., Byerly, J. W. and Biba, W. T. (1988). The evaluation of forebody compression at hypersonic Mach numbers. AIAA Paper 88-0479.
19. Peraire, J., Vahadati, M., Morgan, K. and Zienkiewiz, O. C. (1987). Adaptive remeshing for compressible flow computations. J. of Computational Physics., pp. 449-446.
20. Reklis, R. P. and Lombard, C. K. (1982). Shock-capturing algorithm for the Navier-Stokes equations. AIAA J., Vol. 20, pp. 1212-1218.
21. Rizzi, A. W. and Inouye, M. (1973). Time split finite volume method for three-dimensional blunt body flow. AIAA J., Vol. 11, pp. 1478-1485.

22. Ruffin, S. M. (1988). Solutions for hypersonic viscous flow over delta wing. AIAA Paper 88-0126.
23. Schroder, W. and Hanel D. (1987). An unfactored implicity scheme with multigrid accleration for the solution of the Navier-Stokes equation. Computers and Fluids, Vol. 15, pp. 313-336.
24. Steger, J. L. and Warming, R. F. (1981). Flux vector splitting of the inviscid gasdynamics equations with application to finite difference methods. J. Comp. Phys., Vol. 40, pp. 263-293 (1981).
25. Tam, P. and Li, C. P. (1990). Comparisons of thermochemical nonequilibrium viscous flowfield predictions for AFE vehicle. AIAA Paper 90-0141.
26. Van Leer, B. (1982). Flux-Vector splitting for the Euler equations Lecture Notes in Physics, Vol. 170, pp. 507-512.
27. Warming, R. F. and Beam, R. M. (1976). Upwind second order difference schemes and applications in aerodynamic flows. AIAA J., Vol. 14, pp. 1241-1249.
28. Wornom, S. F. and Hafez, M. M. (1986). Implicit conservation schemes for the Euler equations. AIAA J., Vol. 24, pp. 15-223.
29. Yamamoto, Y. (1988). Numerical simulation of hypersonic flow around a space plane. AIAA Paper 88-2615.
30. Yamamoto, Y. and Kubo, S. (1989). Numerical simulation of hypersonic flow around a space planeat high angle of attack using implicit TVD Navier-Stokes code. AIAA Paper 89-0274.
31. Yee, H. C., Kopter, G. H. and Montagne, J. L. (1988). High resolution shock-caputring schemes for inviscid and viscous hypersonic flows. NASA TM 100097.

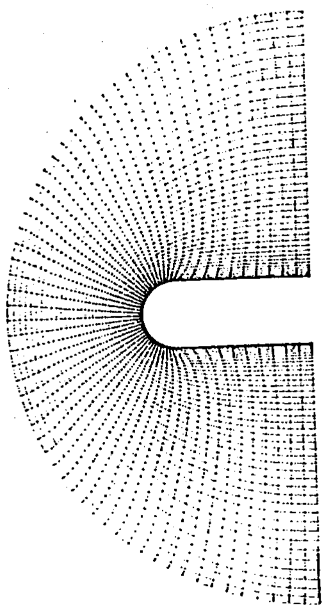

Fig. 1. Computation grid system for sphere-cylinder combination.

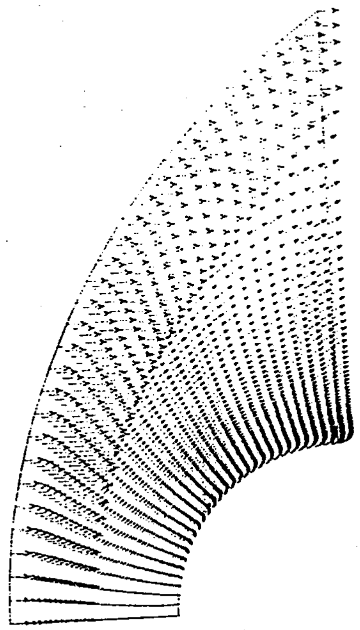

Fig. 2. Velocity velocity vector for $M_\infty = 4$, $Re_\infty = 6.8 \times 10^5$ over circular cylinder.

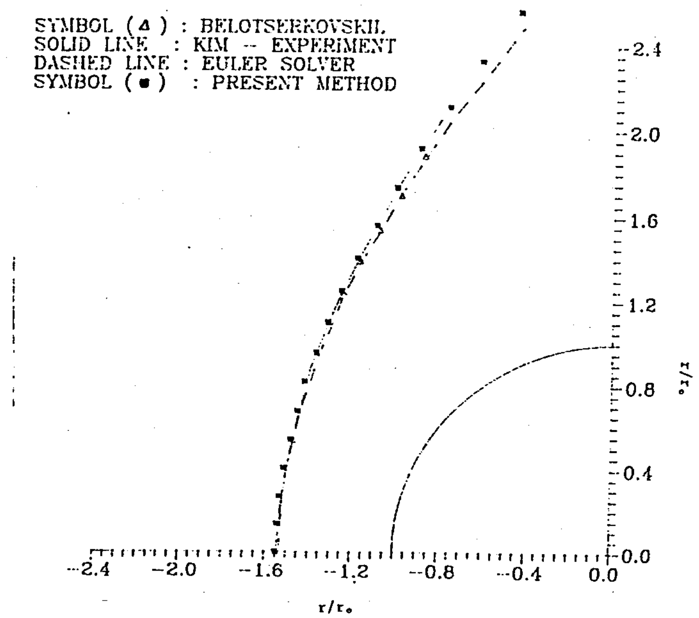

Fig. 3. Bow shock location for $M_\infty = 4$ over circular cylinder.

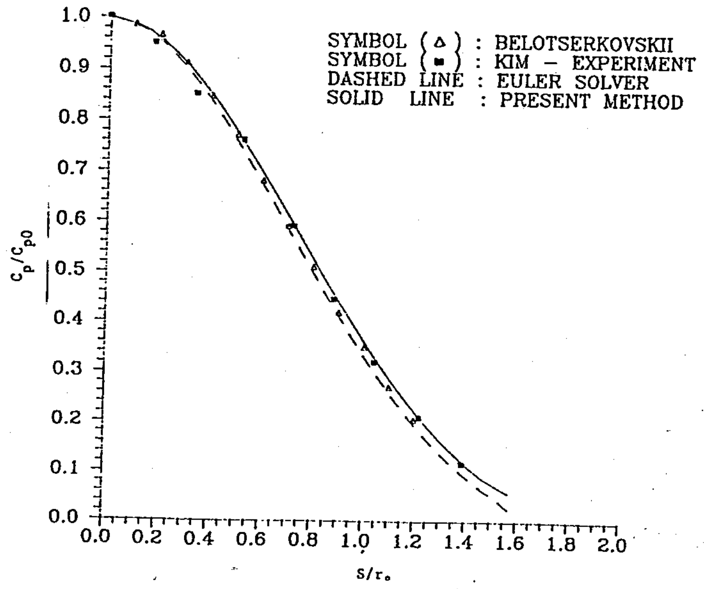

Fig. 4. Pressure coefficient on cylinder surface for $M_\infty = 4$.

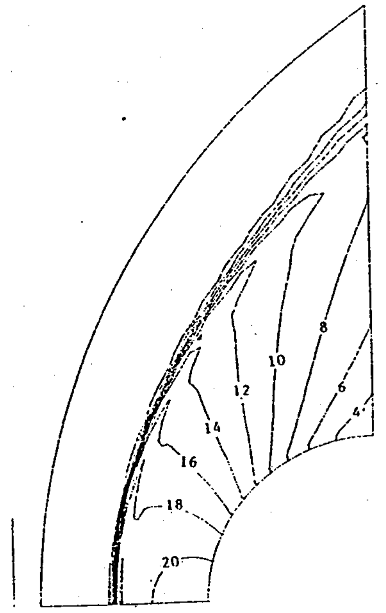

Fig. 5. Iso-bar pattern for $M_\infty = 4$ over circular cylinder.

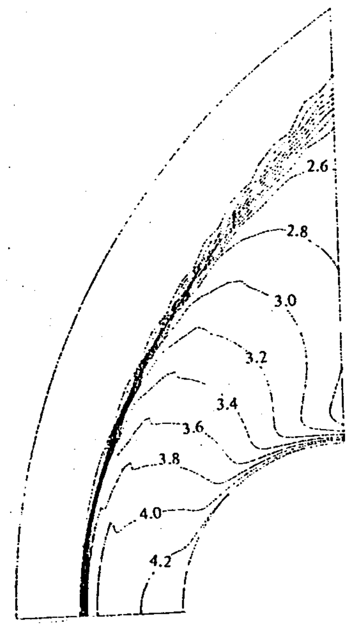

Fig. 6. Iso-thermal pattern for $M_\infty = 4$ over circular cylinder.

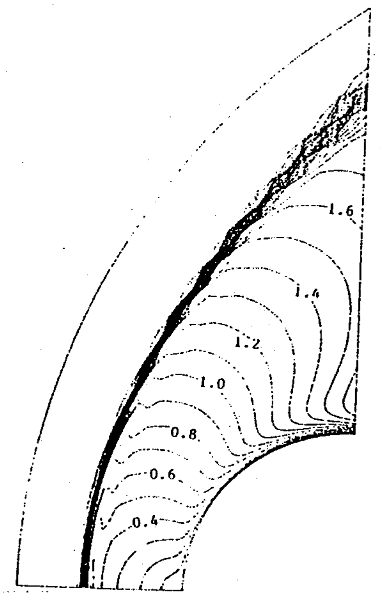

Fig. 7. Mach number distribution for $M_\infty = 4$ over circular cylinder.

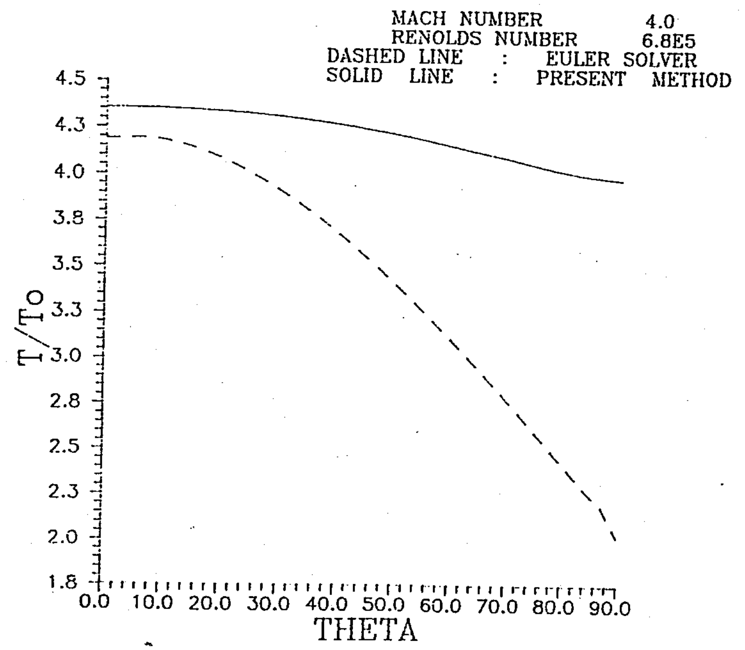

Fig. 8. Temperature distribution on the cylinder surface for $M_\infty = 4$.

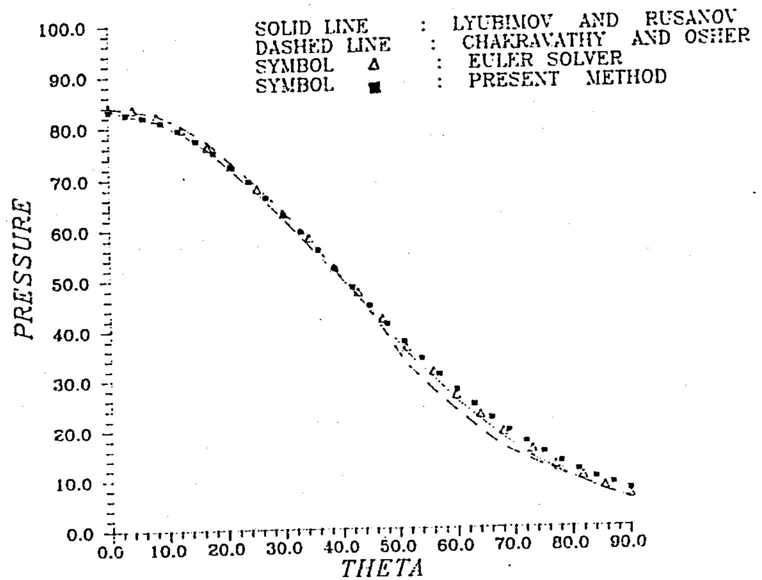

Fig. 9. Pressure on cylinder surface for $M_\infty = 8$, $Re_\infty = 1.36 \times 10^6$.

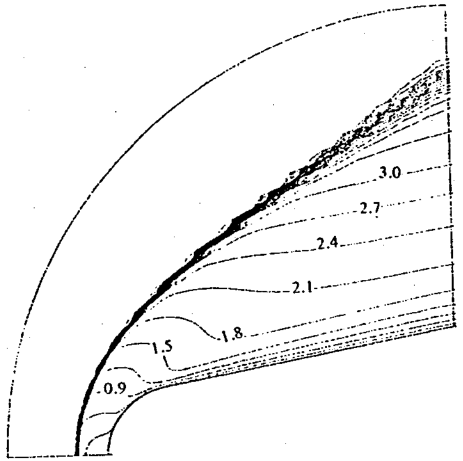

Fig. 10. Mach number distribution for $M_\infty = 8$, $Re_\infty = 1.36 \times 10^6$ over cylinder-cone combination.

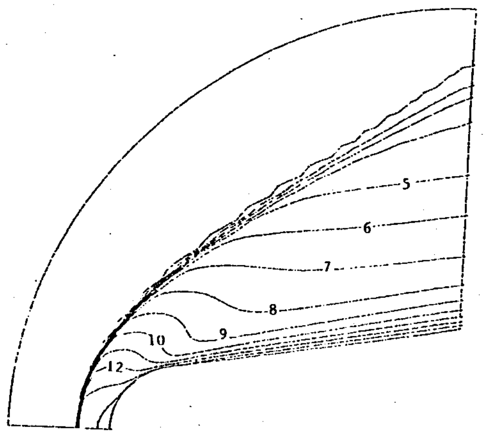

Fig. 11. Iso-thermal pattern for $M_\infty = 8$ over cylinder-cone combination.

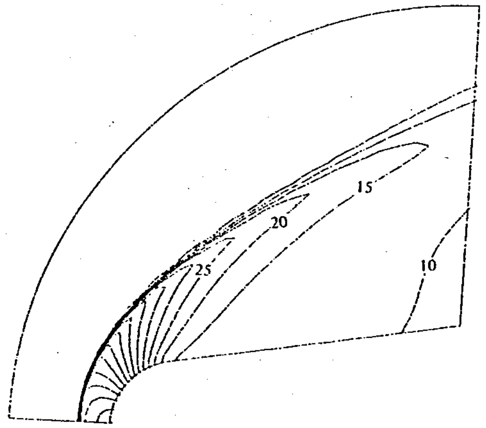

Fig. 12. Iso-bar pattern for $M_\infty = 8$ over cylinder-cone combination.

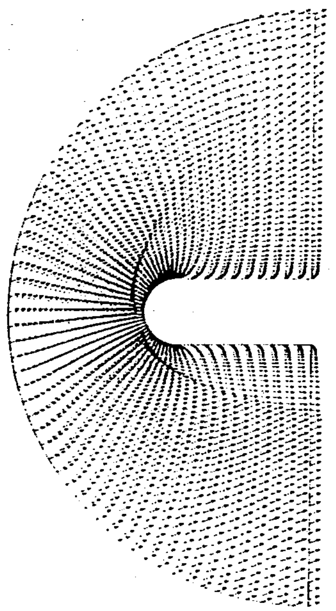

Fig. 13. Velocity vector for M_∞ = 25, Re_∞ = 3.5 x 10, $\alpha = 20°$ over sphere-cylinder combination.

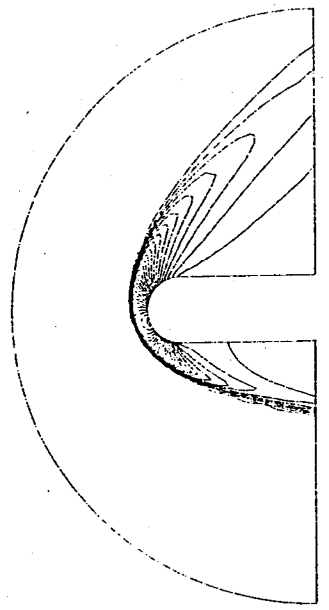

Fig. 14. Iso-bar pattern for M_∞ = 25, $\alpha = 20°$ over sphere-cylinder combination.

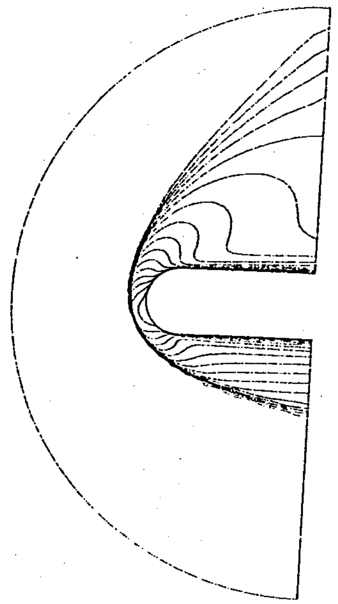

Fig. 15. Iso-thermal pattern for M_∞ = 25, $\alpha = 20°$ over sphere-cylinder combination.

ON THE ISOLATED DISTURBANCE IN A TURBULENT BOUNDARY LAYER BY THE CONDITIONAL SAMPLING SCHEME

Bao-Shi Shiau
Institute of Physics, Academia Sinica, Taipei, Taiwan, 11529, R.O.C.
and
Shui-Shong Lu
Department of Mechanical Engineering, National Taiwan University
Taipei, Taiwan 10764, R.O.C.

Abstract

An artificial isolated disturbance in the wall region of a fully developed turbulent boundary layer was investigated experimentally by using a hot-wire anemometer. The Isolated disturbance was generated by a small pin which was driven up and down through a minute hole into the boundary layer. A DC servo system was used to drive a cam and the small pin follower. A conditional sampling scheme was employed to yield the streamwise turbulent velocity distributions. Results show that the isolated disturbance propagates and decays in strength as it moves downstream from the source. The affected region of artificial disturbance generated in the present study is very close to that of the energetic near-wall eddy which was reported in the previous flow visualization studies.

Presented at the Pressure Vessel and Piping Conference, American Society of Mechanical Engineers, Tennessee, June, 1990.

EFFECT OF TURBULENCE INTENSITY ON WAKE FLOW OF A CYLINDER

Bao-Shi Shiau, Victor W. Nee***
*and Robert R. Hwang**

** Institute of Physics, Academia Sinica, Taipei, Taiwan, R.O.C.*
*** Department of Aerospace and Mechanical Engineering*
University of Notre Dame, Indiana, U.S.A.

Abstract

Different turbulence intensities in the same mean velocity flow fields are created. The effect of turbulence intensity on the wake behind a cylinder is investigated. The study is conducted in the low speed wind tunnel which test section is 18.5 m long, 3.2 m wide, and 2.2 m high. The measurement results exhibit that the similarity of wake mean velocity distribution appears in the near wake region when turbulence intensity becomes higher.

Presented at the 13-th National Conference on Theoretical and Applied Mechanics, Dec. 1989.

CRYSTALLIZATION STUDY OF AMORPHOUS $Fe_{86}B_{14}$ BY THE ELECTRICAL RESISTIVITY METHOD

S. U. Jen (任盛源) *L. P. Lee* (李廉步) *and C. H. Lam* (林志雄)

Institute of Physics, Academia Sinica
Taipei, Taiwan, R.O.C.

Abstract

We have studied the isothermal crystallization behaviors of $Fe_{86}B_{14}$ at annealing temperature T_a = 320C for annealing time t = 0–300 min. The techniques used in this study included electrical resistivity measurements, magnetization measurements, and X-ray analysis. It was found that at T_a = 320C, α-Fe is the major species of crystallization in $Fe_{86}B_{14}$, and these crystallites grow first from the top and the bottom surfaces and then into the interiors. Based on the model calculations, we provided a simple method to estimate the kinetics of α-Fe growth.

To appear in J. Phys. Chem. Solids (1990)

鈀與重水無室溫融合現象之實驗觀察

吳建國
大同工學院材料工程研究所
姚永德* 王建萬 林爾康
中央研究院物理研究所

摘　要

當進行 γ 射線及中子測量實驗時，在酸性電解液中，採用較易得到金屬面高密度氘原子之 $KHSO_4$ 添加鹽。配合的溶液還包括添加 Na_2S 及硫代尿素（H_2NCSNH_2）等氫原子促進劑，以便鈀表面覆滿最高密度原子狀態的氘。實驗結果，均未測出與融合相關之 γ 射線及中子等。此外，我們以 5 mm 直徑長約10公分之鈀條爲陰極，以 0.5 mm 直徑的鉑線環繞於鈀條四周爲陽極，在 $LiOH + D_2O$ 溶液中經一個多月來之測量，但均未測出與室溫融合相關之 γ 射線、中子。

綜結我們的實驗結果，陰極鈀金屬表面與重水之反應，經過一個多月來之觀察尚未觀察到氘原子室溫融合現象。

Published in Chemistry (The Chinese Chem. Soc., Taiwan China) June, 1989 Vol. 47, No. 2, PP. 139 - 141.

SUPERCONDUCTING PROPERTY AND STRUCTURE STUDIES OF $YBa_2Cu_3O_7$-Ag_2O COMPOSITES

J. J. Lin, Teng-Ming Chen,† Y. D. Yao,†† J. W. Chen, and Y. S. Gou†††
Department of Physics, National Taiwan University
Taipei 10764, Taiwan
† Institute of Applied Chemistry, National Chiao-Tung
University, Hsinchu 30050, Taiwan
†† Institute of Physics, Academia Sinica
Taipei 11529, Taiwan
††† Institute of Electrophysics, National Chiao-Tung
University, Hsinchu 30050, Taiwan

Abstract

We have studied the superconducting property and the structure of $YBa_2Cu_3O_7$ added with Ag_2O, with the weight ratios of $YBa_2Cu_3O_7$ to Ag equal to 4, 6, 8, and 10. Resistance and magnetization measurements show that the normal-state transport behavior and the superconducting transition temperature, T_c, are insensitive to the amount of Ag added. The normal-state resistance decreases linearly with temperature, reaching a large value of $\cong 3$ for the ratio R(300K)/R(100K). This value is evidently larger than that ($\leqslant 2.5$) generally observed in polycrystalline $YBa_2Cu_3O_7$, and is ascribed to the improved grain growth behavior resulting from Ag addition. X-ray diffraction and scanning electron microscopy studies have also been

Published in Japanese Journal of Applied Physics 29, 497 (1990).

PHOTOEMISSION STUDIES OF THE EFFECTS OF SILVER IN THE ELECTRON-DOPED SUPERCONDUCTOR, $Nd_{2\text{-}x}Ce_xCuO_{4\text{-}\delta}$

C. S. Ares Fang, Y. D. Yao and C. C. Wu[a]

Institute of Physics, Academia Sinica, Taipei 11529, Taiwan, R.O.C.
a. Department of Physics, Fu-Jen University, Taipei, Taiwan, R.O.C.

Abstract

Variations of physical properties with silver addition and substitution of 10% and 20% in the bulk $Nd_{1.85}Ce_{0.15}CuO_{4\text{-}\delta}$ electron-doped superconductor have been investigated. The T_c drops from −24K to −22K with 10% doping. It becomes non-superconducting when the Ag content is increased to 20%. Ag clusters were observed in the 20% Ag-doped samples. Ag impurities also behave as a good oxygen stabilizer.

Published in C 167, 89 (1990).

MAGNETIC PROPERTIES OF SUPERCONDUCTING $nMBa_2Cu_3O_x$:Ag (M = Y, Gd, and Eu) COMPOSITES

C. Y. Huang,[*] T. J. Li,[†] Y. D. Yao,[†] L. Gao,[‡] Z. J. Huang,[‡] Y. Shapira,[§,+]
E. J. McNiff, Jr.,[§] and M. K. Wu[–]

[*] *Lockheed Missiles & Space Company, Inc., Research & Development Division,*
Palo Alto, CA 94304-1191, USA

[†] *Institute of Physics, Academia Sinica, Taipei, Taiwan*

[‡] *Texas Center for Superconductivity and Department of Physics*
University of Houston, Houston, TX 77004, USA

[§] *Francis Bitter National Magnet Laboratory, Massachusetts Institute of Technology*
Cambridge, MA 02139, USA

[+] *Department of Physics, Tufts University, Medford, MA 02155, USA*

[–] *Department of Metallurgy and Materials Science, Henry Krumb School of Mines*
Columbia University, New York, NY 10027, USA

Abstract

We measured the M-H hysteresis loops of $nYBa_2Cu_3O_x$:Ag (n = 3, 5, and 7) and $3RBa_2Cu_3O_x$:Ag (R = Gd and Eu) as a function of temperature, and found that the residual magnetization and, hence, pinning is independent of n and the rare-earth ions (R and Y), but depends greatly on the processing conditions. These samples exhibit the strongest pinning force for high-temperature superconductors developed to date.

Published in Modern Physics Letters B Vol. 3, No. 16 (1989) 1251-1265.

PREPARATION OF HIGH-PURITY $Tl_2Ca_nBa_2Cu_{n+1}O_{6+2n}$ (n = 1,2) POWDERS FROM STOICHIOMETRIC REACTANT MIXTURES

Nae-Lih Wu
National Taiwan University, Department of Chemical Engineering
Taipei, Taiwan R.O.C.

Yeong Der Yao
Institute of Physics, Academia Sinica, Taipei, Taiwan, R.O.C.

Abstract

New powder synthesis methods have been developed for preparing the single-phase $Tl_2CaBa_2Cu_2O_8$ (the 2122 compound) and $Tl_2Ca_2Ba_2Cu_3O_{10}$ (the 2223 compound) powders from stoichiometric reactant mixtures. The 2122 compound was prepared from a stoichiometric mixture of Tl_2O_3, CuO, and $CaBa_2CuO_4$, while the 2223 compound was prepared from the same mixture but with additional CaO and CuO to match the correct (Tl:Ca:Ba:Cu = 2:2:2:3) stoichiometry. The single-phase 2122 samples with T_c above 110 K were obtained by using one-step calcination at 830°C, while the 2223 samples with T_c ranging between 115 and 120 K were obtained by employing a first calcination at 830°C for 5 hrs and a second calcination at 870°C. Powder melting, which is strongly associated with the conventional methods, was significantly suppressed in the new methods.

Published in Mat. Res. Soc. Symp. Proc. 169, in press (1990).

SUPERCONDUCTING AND NORMAL STATE PROPERTIES OF THE $Y_{1-x}Cd_xBa_2Cu_3O_{7-\delta}$ SYSTEM

J. W. Chen, C. F. Chen and T. C. Chang
Department of Physics, National Taiwan University, Taipei, Taiwan

Y. D. Yao
Institute of Physics, Academia Sinica, Taipei, Taiwan

Abstract

The superconducting and normal state properties of the pseudo-quaternary system $Y_{1-x}Cd_xBa_2Cu_3O_{7-\delta}$ with $0 \leqslant x \leqslant 1.0$ were investigated by means of the AC electrical resistance, DC magnetization and powder X-ray diffraction measurements. For Cd concentration $x \leqslant 0.6$, X-ray diffraction pattern reveals that the majority phase of the samples is of the oxygen deficiency perovskite type with a gradual change from orthorhombic to tetragonal structure as x increases. The superconducting transition temperature T_c was observed to remain almost unchanged up to $x \cong 0.6$. This means the superconductivity occurs in orthorhombic structure as well as in the tetragonal structure. However, DC magnetization measurements taken at $H = 20$ G indicate that the superconducting volume fraction in the sample decreases as x increases, although T_c remains unchanged, which shows that superconductivity in these samples is of granular characteristic.

Published in Physica C 165, 287 (1990).

MAGNETIZATION STUDY ON GRAIN-BOUNDARY PRECIPITATION IN A Ni-8 at. %Sn ALLOY

Y. D. Yao, Y. Y. Chen, and T. J. Li
Institute of Physics, Academia Sinica, Taipei, Taiwan
Republic of China

T. H. Chuang
Graduate Institute of Material Engineering, National Taiwan University
Taipei, Taiwan, Republic of China

Abstract

The variations of the grain-boundary precipitates, the electrical resistivity, and the magnetization of a Ni-8 at. % Sn alloy have been investigated as functions of annealing temperature and annealing time. For samples annealed at 773°K, the averaged growth rate of the size of the grain boundary precipitates is roughly 0.42 μm/h for the first 24 h; the electrical resistivity at $T = 10°K$ and the magnetization at $T = 10°K$ and $H = 5$ kG vary monotonically with respect to the annealing time for the first 2 weeks, changing from 22.5 to 7 μΩ/cm for the electrical resistivity and from 27 to 33 emu/g for the magnetization. A large tail section in the magnetization versus temperature curve was also observed in the aged samples. All these electrical and magnetic variations in the Ni-8 at. %Sn samples annealed at 773°K varied monotonically with respect to the growth of the grain-boundary precipitates.

Published in Journal of Applied Physics (1990).

EFFECTS OF SILVER DOPING IN THE HIGH-Tc SUPERCONDUCTOR SYSTEM Y-Ba-Cu-O

Y. H. Kao, Y. D. Yao,[1] *L. Y. Jang,*[2] *F. Xu, A. Krol, L. W. Song, and C. J. Sher*
Department of Physics, State University of New York at Stony Brook,
Stony Brook, New York 11794-3800
1) Institute of Physics, Academia Sinica
Taipei, Taiwan 11529
2) Department of Physics, National Tsing Hua University
Hsinchu, Taiwan 30043

A. Darovsky and J. C. Phillips
SUNY X3 Beamline, National Synchrotron Light Source
Brookhaven National Laboratory, Upton, New York 11973

J. J. Simmins and R. L. Snyder
Alfred University, Alfred, New York 14802

Abstract

Changes in various superconducting properties as a function of silver substitution in the bulk granular high-Tc system Y-Ba-Cu-O have been investigated. In the low doping limit, Ag impurities behave as an excellent oxygen stabilizer and the critical current density is enhanced by an order of magnitude while the Tc remains practically unchanged. When the Ag content is increased to above 20%, the Tc starts to drop and the effects of Ag clusters as well as impurity phases become more important. However, the compound is still a superconductor with a Tc around 20 K by full substitution of Ag for Cu. The problems concerning the location of Ag atoms and formation of Ag clusters are examined with measurements of x-ray absorption fine structure using synchrotron radiation. Our results indicate that at least some Ag atoms occupy the Cu(1) and Cu(2) sites in the material. Magnetic field dependence shows that the critical current density of a bulk sintered high-Tc superconductor below a characteristic value H'c is mainly controlled by intergranular weak-link coupling. A shift of H'c with the addition of Ag helps explain the variation of critical current density in this compound system.

Published in Journal of Applied Physics, 67, 353 (1990).

ELECTRICAL RESISTIVITY OF NICKEL-RICH NICKEL-INDIUM ALLOYS BETWEEN 10 AND 800 K

S. J. Tzeng(1), *Y. D. Yao*(2) *and T. H. Chuang*(3)

1 National Taipei Institute of Technology, Taipei, Taiwan, R.O.C.
2 Institute of Physics, Academia Sinica, Taipei, Taiwan, R.O.C.
3 Graduate Institute of Material Engineering, National Taiwan University
Taipei, Taiwan, R.O.C.

Abstract

The electrical resistivity ρ of nickel-indium alloys containing 0.0, 1.5, 3.0, 5.0 and 7.5 at.% In has been studied as a function of the absolute temperature T between 10 and 800 K. The Curie temperature Tc is determined from the maximum in the $d\rho/dT$ vs. T curves which rise gently towards a maximum and then drop sharply above this maximum. Our data show that the values of Tc decrease with increasing the indium content; and with a slope of roughly 26.7 K per at.% of In. The residual resistivity of the Ni-In alloy measured at 10 K shows that it increases roughly 2 $\mu\Omega$-cm per at.% of indium.

Published in Phys. Stat. Sol., A117, K47 (1990).

MAGNETIC, MICROSTRUCTURE, AND HIGH-FIELD STUDIES OF SUPERCONDUCTING 123-AgO COMPOSITES

C. Y. Huang, H. H. Tait†*
Lockheed Missiles & Space Company
** Research & Development Division, Palo Alto, CA 94304 USA*
† Materials & Process Laboratories, Sunnyvale, CA 94088 USA

Y. D. Yao, T. J. Li, Y. Y. Chen
Institute of Physics, Academia Sinica, Taipei, Taiwan

and M. K. Wu
Department of Metallurgy and Materials Science
Columbia University, New York, NY 10027 USA

Abstract

We have measured the magnetization of some $nRBa_2Cu_3O_x$:Ago (R = rare earth) composites as a function of temperature and field up to 20 T. The residual magnetization is large and, hence, the pinning is very strong. From the hysteresis loops, we have obtained the critical current density and the pinning force. We have also investigated the time dependence of the magnetization in response to an applied field, from which the energy barrier were obtained. Our scanning electron microscopic, energy-dispersive x-ray spectroscopic, and polarized light microscopic studies have revealed that the addition of AgO results in the growth of very large grains (~1 mm). The resistance near Tc at high field reveals that the phase slippage is responsible for the transition.

Published in Progress in High Temperature Superconductivity – Vol. 19, P. 84 (1989).

SUPERCONDUCTING AND NORMAL STATE PROPERTIES OF BiSrCaCuO WITH Ag AND Pb DOPING

Y. D. Yao, Y. Y. Chen, Y. H. Kao, J. H. Chen and C. L. Liu*

Institute of Physics, Academia Sinica
Taipei, Taiwan 11529, R.O.C.
** Department of Physics, State University of New York,*
Stony Brook, NY 11794, U.S.A.

Abstract

Superconducting and normal state properties of the High-Tc system Bi-Sr-Ca-Cu-O doped with Ag and Pb impurities have been investigated. Measurements of electrical resistivity and magnetization of compounds with different stoichiometry, eg. $(Bi_{1-x}A_x)_2Sr_2CaCu_2O_y$ and $Bi_2Sr_2Ca(Cu_{1-x}A_x)_2O_y$, where A = Ag or Pb, were made below 300 K. The structure of samples was studied by powder X-ray diffraction analysis. These results were compared with the similar data obtained with a series of samples in which the Cu and Bi contents were varied. In this way effect arising from Cu and Bi deficiency in the system and influence caused by the impurity atoms can be systematically analyzed.

Published in Progress in High Temperature Superconductivity – Vol. 19, P. 249 (1989).

XPS STUDY OF THE PHASE-DECOMPOSITION IN Ni-Sn ALLOY

*K. C. Lin, Y. D. Yao, N. T. Liang, C. S. Fang, R. L. Luo and T. H. Chuang**

Institute of Physics, Academia Sinica, Taipei, Taiwan, R.O.C.
** Graduate Institute of Material Engineering, National Taiwan University*
Taipei, Taiwan, R.O.C.

Abstract

XPS (X-ray Photoelectron Spectroscopy) technique is used to study the surface segregation and phase-decomposition in Ni-Sn alloy system. Surface segregation of samples with and without annealing at 773 K is studied. The composition variations evolved during annealing. Sn segregation to the surface in the Ni-3at.%Sn and Ni-8at.%Sn alloys has been observed. This phenomenon can be explained by the surface energy difference and concentration difference of the Ni and Sn in this binary alloy system.

Published in Proc. of The 1989 Annual Conf. of The Chinese Soc. for Mat. Sci., P. 285.

MAGNETIC AND THERMAL PROPERTIES OF SOME Al-Mn STEELS

S. K. Lee, Y. D. Yao, S. U. Jen, P. L. Huang and C. C. Lee*

Institute of Physics, Academia Sinica, Taipei 11529, Taiwan, R.O.C.
** Department of Physics, Fu Jen University, Taipei, Taiwan, R.O.C.*

Abstract

The thermal properties of some Al-Mn steels have been studied in the temperature range between 120 K and 300 K. The magnetization of these samples has been measured between 30 K and 300 K. Antigerromagnetic behavior has been observed in some of our samples between 30 K and 300 K. These experimental data are compared with that of these commercial 304 stainless steels; we also found that the Neel temperature of the 304 stainless steels is below 70 K.

Published in Proc. of The 1989 Annual Conf. of The Chinese Soc. for Mat. Sci., P. 85.

ELECTRICAL RESISTIVITY STUDY OF NICKEL-INDIUM ALLOYS

S. J. Tzeng[1], Y. D. Yao[2] and T. H. Chuang[3]

1 National Taipei Institute of Technology, Taipei, Taiwan, R.O.C.
2 Institute of Physics, Academia Sinica, Taipei, Taiwan, R.O.C.
3 Graduate Institute of Material Engineering, National Taiwan University
Taipei, Taiwan, R.O.C.

Abstract

Electrical resistivity ρ of nickel-indium alloys containing 0.0, 1.5, 5.0 and 7.5 at.%In has been studied as a function of the absolute temperature T between 15 K and 800 K. The Curie temperature Tc is determined from the maximum in the $d\rho/dT$ vs. T curves which rise gently towards a maximum and then drop sharply above this maximum. Our data show that the values of Tc decrease with increasing the indium content. The residual resistivity of the Ni-In alloys measured at 15 K shows that it is consisted with the Nordheim rule.

Published in Proc. of The 1989 Annual Conf. of The Chinese Soc. for Mat. Sci., P. 281.

ELECTRICAL AND MAGNETIC STUDIES ON GRAIN BOUNDARY SEGREGATION IN A Ni-3AT.%Sn ALLOY

Y. D. Yao(1), *T. H. Chuang*(2) *and C. K. Lee*(3)

(1) Institute of Physics, Academia Sinica, Taipei, Taiwan, R.O.C.
(2) Graduate Institute of Material Engineering, National Taiwan Univeristy, Taipei, Taiwan, R.O.C.
(3) Department of Physics, National Central University, Chung Li, Taiwan, R.O.C.

Abstract

The variations of the grain boundary precipitation, the electrical resistivity and the magnetization of a Ni-3at.%Sn alloy have been investigated as a function of annealing time and annealing temperature. The averaged growth rate of the size of the grain boundary precipitates for samples annealed at 773 K is roughly 7 μm per week. The residual electrical resistivity for samples annealed at 773 K decreases roughly 0.6 $\mu\Omega$-cm per week. All the electrical and magnetic properties in the Ni-3at.%Sn samples annealed at 773 K vary monotonically with respect to the growth of the grain boundary precipitation and segregation.

Published in IEEE Transactions on Magnetics, Vol. 25, 3958 (1989).

PROBING THE EFFECT OF ATOMIC SUBSTITUTION IN THE SUPERCONDUCTOR Y-Ba-Cu-O BY X-RAY ABSORPTION

L. Y. Jang, F. Xu, Y. D. Yao, A. Krol, S. C. Woronick
and Y. H. Kao

Department of Physics, State University of New York
Stony Brook, New York 11794

Abstract

X-ray absorption techniques are employed to investigate the local structure around Ag and Fe impurity atoms in chemically-doped high-Tc superconductor Y-Ba-Cu-O. Changes in these spectra with dopant content are correlated with the variation of valence state and location of the substituted atoms in the host material.

Published in physica B158 (1989) 467-468, North-Holland, Amsterdam.

OXYGEN K-EDGE EXAFS OF THE HIGH-Tc SUPERCONDUCTOR Y-Ba-Cu-O

Y. H. Kao, L. Y. Jang, W. Ng, A. Krol,
S. C. Woronick, F. Xu, Y.D. Yao

Department of Physics, State University of New York
Stony Brook, New York 11794

Abstract

EXAFS spectra above the oxygen K absorption edge of the high-Tc superconductor Y-Ba-Cu-O have been studied by measuring the total electron yield (TEY) as a function of x-ray energy. Temperature variation of the TEY spectra was examined between 77K and 300K. These data provide evidence for the existence of local soft modes in the material.

Published in physica B158 (1989) 488-489, North-Holland, Amsterdam.

STUDIES OF SHORT RANGE ORDER STRUCTURE IN THE HIGH-Tc SUPERCONDUCTOR Y-Ba-Cu-O USING X-RAY ABSORPTION TECHNIQUES

A. Krol, L. Y. Jang, S. C. Woronick, F. Xu, Y. D. Yao, Y. H. Kao

Department of Physics, State University of New York
Stony Brook, New York 11794

Abstract

XAFS techniques are employed to investigate the local structure around Cu, Y, and Ba atoms in the high-Tc superconductor Y-Ba-Cu-O. The XAFS spectra are also used to examine possible effects on the local environment surrounding Cu atoms due to oxygen deficiency and chemical doping.

Published in physica B158 (1989) 465-466, North-Holland, Amsterdam

SOME PHYSICAL PROPERTIES OF SUSPENDABLE SUPERCONDUCTING 123-Ag COMPOSITES

C. Y. Huang, H. H. Tai,* Y. D. Yao,+ T. J. Li,+ and M. K. Wu†*
** Lockheed Palo Alto Research Laboratory, Palo Alto, CA 94304*
+ Institute of Physics, Academia Sinica, Taipei, Taiwan
† Dept. of Physics, Tsinghua University, Hsinchu, Taiwan

Abstract

We have measured the M-H hysteresis loops of n $YBa_2Cu_3O_y$:Ag (n = 3, 5, and 7), and $3RBa_2Cu_3O_y$:Ag (R = rare earth) as a function of temperature. We have found that the residual magnetization and, hence, pinning, is strong and is independent of n and R, but dependent on the metallurgy. The giant creep rates have been measured and are greater than those of pure 123 samples. Scanning electron microscopy and polarized light microscopy have shown that the presence of silver gives rise to the growth of large grains (~1 mm) in the 123-Ag samples. The field dependence of the critical current density is not strong at high field. We have also measured the resistance in field up to 200 kOe. The resistance remains zero even at 80 K and 200 kOe. The field dependence of the superconducting transition is discussed in terms of phase slippage.

Published in Mat. Res. Soc. Symp. Proc. 169, in press (1990).

EFFECTS OF DOPING IN THE HIGH-Tc Y-BASED AND Bi-BASED CUPRATES

Y. D. Yao
Institute of Physics, Academia Sinica
Taipei, Taiwan, 11529, R.O.C.

and

Y. H. Kao
Department of Physics, State University of New York at Stony Brook
Stony Brook, N.Y. 11794, U.S.A.

Abstract

Various dopants are introduced into the high-Tc Y-based and Bi-based cuprates; the effects of substitution on super-conducting properties have been studied. In the YBaCuO system, Ag, Cr, Nb, and Ni were used to substitute for 10 atomic percent of Cu while Cl, S, Se, and Te were used to substitute for 0. In the BiSrCaCuO system, Ag, Cr, Pb, and Ni were used to substitute for 10 atomic percent of Cu; and S was used to substitute for 0. Changes in superconducting transition temperature, critical current density, and room temperature resistivity caused by atomic substitution are investigated. These results are compared with similar data obtained with a series of undoped samples in which the Cu content has been varied. Differences and similarities in these materials are discussed.

Published in Proceedings of the 1st Asia-Pacific Conference on Condensed Matter Physics 27 June - 3 July 1988.

PREPARATION OF $Tl_2CaBa_2Cu_2O_8$ BY A LOW-TEMPERATURE SOLID STATE REACTION METHOD

Nae-Lih Wu[1], Sern-Nan Lee[1], Yeong Der Yao[2]
and Eli Ruckenstein[3]

1 Department of Chemical Engineering, National Taiwan University
Taipei, Taiwan, R.O.C.
2 Institute of Physics, Academia Sinica, Taipei, Taiwan, R.O.C.
3 Department of Chemical Engineering, SUNY at Buffalo
Buffalo, New York, U. S. A.

Abstract

Superconducting $Tl_2CaBa_2Cu_2O_8$ (the 2122) compound was prepared by using a new solid state method in which $CaBa_2CuO_4$ was used as the Ca and Ba sources in the starting powder mixtures. The effects of calcining variables, including calcining temperature and time, on the superconducting properties of the calcined powders were studies. It was found that XRD single-phased 2122 powders with superconducting temperatures, including zero-resistivity (Tc, zero) and diamagnetic onset temperatures, at 110 K were readily obtained after calcination at 830 C for 6 hrs. The superconducting temperatures were further increased, up to 116 K, with an increase in calcining time. No powder melting was observed for calcination at 830 C. Calcination conducted above 850 C resulted in powder melting, and powders thus prepared showed a very high normal-state resistivity and a broad resistivity drop typically with a Tc, onset near 120 K and a Tc, zero remaining at 110 K.

Published in Progress in High Temperature Superconductivity – Vol. 19 (1989).

ELECTRICAL AND MAGNETIC PROPERTIES OF $Y_{1-x}Cd_xBa_2Cu_3O_{7-\delta}$ AND $Gd_{1-x}Cd_xBa_2Cu_3O_{7-\delta}$

J. W. Chen, C. F. Chen, T. C. Chang, and J. J. Lin

Department of Physics, National Taiwan University
Taipei, Taiwan, R.O.C.
and
Y. D. Yao
Institute of Physics,
Academia Sinica, Taipei, Taiwan, R.O.C.

Abstract

We have performed the ac electrical resistance R(T), and dc magnetization measurements on the pseudo-quaternary systems $Y_{1-x}Cd_xBa_2Cu_3O_{7-\delta}$ and $Gd_{1-x}Cd_xBa_2Cu_3O_{7-\delta}$ with $0 \leqslant x \leqslant 1.0$. Increasing Cd concentration x produces the effects of decreasing the superconducting volume fraction in the samples as well as changing the normal state resistivity from a metallic to a semiconducting behavior in both systems. However, the superconducting transition temperature T_c remains essentially constant with $T_c \cong 90$ K for $x \leqslant 0.6$. Dc magnetization measurements performed at H = 5 KG reveal that the high temperature (100-300 K) susceptibility follows a Curie-Weiss behavior with μ_{eff} changing systematically as x increases.

Published in Progress in High Temperature Superconductivity – Vol. 19 (1989).

SYNTHESIS OF $Tl_2Ca_nBa_2Cu_{n+1}O_{6+2n}$ (n = 1, 2) FROM STOICHIOMETRIC REACTANT MIXTURES

Nae-Lih Wu[a], Yeong Der Yao[b], Sern-Nan Lee[a], S-Yen Wong[a] and Eli Ruckenstein[c]

a Department of Chemical Engineering, National Taiwan University,
Taipei, Taiwan
b Institute of Physics, Academia Sinica, Taipei, Taiwan
c Department of Chemical Engineering, SUNY at Buffalo, Buffalo, NY, USA

Abstract

New powder synthesis methods have been developed for the preparation of single-phase $Tl_2CaBa_2Cu_2O_8$ (the 2122 compound) and $Tl_2Ca_2Ba_2Cu_3O_{10}$ (the 2223 compound) powders from stoichiometric reactant mixtures. The 2122 compound was prepared from a stoichiometric mixture of Tl_2O_3, CuO and $CaBa_2CuO_4$, while the 2223 compound was preared from the same mixture but with additional CaO and CuO to match the correct (Tl:Ca:ba:Cu = 2:2:2:3) stoichiometry. For the 2122 compound. XRD single-phase samples with zero-resistivity temperatures ($T_{c,zero}$) above 100 K were obtained by using a one-step calcination at 830°C for a period between 6 and 23 h. A maximum of $T_{c,zero}$ of 116 K was obtained for 14 h of calcination. For the 2223 compound. XRD single-phase samples with $T_{c,zero}$ between 110 and 118 K were obtained by employing a two-step calcination procedure consisting of a first calcination at 830°C for 5 h and a second calcination at 870°C for a period between 2 and 6 h. Both the 2122 and 2223 samples thus prepared exhibit sharp superconducting transitions and typically have a saturation Meissner effect of about 20% of $(-1/4\pi)$ under a field of 20 G. Powder melting is completely eliminated during the preparation of the 2122 compound and much reduced, by employing the pre-calcination step, during the preparation of the 2223 compound. Compared with the conventional method, the new methods require less stringent calcination conditions, and hence allow for a better process control of the synthesis of $Tl_2Ca_nBa_2Cu_{n+1}O_{6+n}$ superconducting powders.

Published in Physica C 161 (1989) 302-312.

NEW REACTION ROUTES FOR PREPARING SINGLE-PHASE $Tl_2CaBa_2Cu_2O_8$ and $Tl_2Ca_2Ba_2Cu_3O_{10}$ POWDERS FROM STOICHIOMETRIC MIXTURES

Nae-Lih Wu, Sern-Nan Lee and Yeong Der Yao†

Department of Chemical Engineering, National Taiwan University,
Taipei, Taiwan, R.O.C.
† Institute of Physics, Academia Sinica, Taipei, Taiwan, R.O.C.

Abstract

Single-phase $Tl_2CaBa_2Cu_2O_8$ and $Tl_2Ca_2Ba_2Cu_3O_{10}$ powders were prepared from stoichiometric mixtures by the following two reactions: (1) $CaBa_2CuO_4 + Tl_2O_3 + CuO \rightarrow Tl_2CaBa_2Cu_2O_8$ and (2) $Tl_2CaBa_2Cu_2O_8 + CaO + CuO \rightarrow Tl_2Ca_2Ba_2Cu_3O_{10}$. Single-phase powders were obtained at 830°C for the first reaction, and at 870°C for the second reaction. At these temperatures, the extent of powder melting and the rate of Tl loss were small. Powders thus prepared showed superconducting temperatures (both the zero-resistivity and diamagnetic onset temperatures) of above 100 K and a saturation Meissner effect of 20% of $(-1/4\pi)$ at a field of 20 G.

Published in Japanese Journal of Applied Physics, Vol. 28, No. 8, August, 1989, pp. L 1349-L 1351.

FABRICATION OF HIGH-Tc YBaCuO and BiSrCaCuO SUPERCONDUCTING WIRES

Y. D. Yao[a], J. W. Chen[b], W. S. Pern[c], M. T. Yeh[d], I. N. Lin[d], P. C. Yao[d]
S. J. Yang[d] and S. E. Hsu[d]

a Institute of Physics, Academia Sinica, Taipei, Taiwan, R.O.C.
b Department of Physics, National Taiwan University, Taipei, Taiwan, R.O.C.
c Department of Physics, Fu Jen University, Taipei, Taiwan, R.O.C.
d Materials R&D Center, Chung Shan Institute of Science and Technology,
Lung-Tan, Taoyuan, Taiwan, R.O.C.

Abstract

High-Tc YBaCuO and BiSrCaCuO superconducting wires have been fabricated by powder metallurgy technique. Copper and silver tubes were used as the external jackets. High critical current density have been observed in these wire-type superconductors. Thermal annealing studies at 773 K show that silver is much better than copper for the external jackets. Their superconducting properties were investigated according to their magnetic behaviors.

Published in Proc. of The 1989 Annual Conf. of The Chinese Soc. for Mat. Sci. P. 1131.

EFFECTS OF CHEMICAL DOPING AND STOICHIOMETRIC VARIATION IN HIGH-Tc SUPERCONDUCTORS

Y. H. Kao, Y. D. Yao, and L. W. Song*

Department of Physics, State University of New York, Stony Brook
NY 11794, USA
** Institute of Physics, Academia Sinica, Taipei, Taiwan 11529, R.O.C.*

Abstract

Superconducting properties of various chemically-doped high-Tc materials are investigated. By using the results obtained with Cu- and Bi-deficient Y-Ba-Cu-O and Bi-Sr-Ca-Cu-O systems as basis, variations of the transition temperature Tc, critical current density Jc, room temperature resistivity ρ, and oxygen content are compared for different dopant contents. In several cases, Jc and ρ are found to be correlated as both quantities show an exponential dependence on the dopant concentration. Most dopants result in a monotonic decrease of Tc and Jc, except for Ag, F, and Cl. Substitution of Ag and Pb for Cu and Bi in Bi-Sr-Ca-Cu-O indicates a condition for compatibility between the impurity atom and the local structure in the host matrix. Results suggest that the predominant mechanism for high-Tc superconductivity is most likely associated with short-range-order structure in the material.

Published in International Journal of Modern Physics B Vol. 3, No. 4 (1989) 573-594.

CHANGES IN PHYSICAL PROPERTIES OF THE HIGH-Tc SUPERCONDUCTORY Y-Ba-Cu-O DUE TO Cu DEFICIENCY

Y. D. Yao
Institute of Physics, Academia Sinica, Taipei, Taiwan, R.O.C.

Y. H. Kao
Department of Physics, State University of New York at Stony Brook
Stony Brook, NY 11794, USA

J. J. Simmins and R. L. Snyder
Alfred University, Alfred, NY 14802, USA

Z. Tao and K. W. Jones
Brookhaven National Laboratory, Upton, New York 11973, USA

Abstract

Stoichiometry of the well-known high-Tc compound $YBa_2Cu_3O_y$ is modified by varing the Cu concentration in the system, and changes in the oxygen content and superconducting properties are investigated. The oxygen content shows a nonlinear dependence on the Cu concentration. For Cu deficiency up to 20%, the transition temperature Tc remains at a nearly constant value of 93 K. X-ray diffraction measurements show that the compound is orthorhombic in this range of stoichiometric variation, and the Cu-deficient superconductor is single phase. The room temperature resistivity increases exponentially while the critical current density decreases exponentially with increasing Cu deficiency. These results indicate that the predominant mechanism for high-Tc superconductivity is closely related to the local structure around the Cu and O atoms.

Published in Modern Physics Letters B Vol. 3, No. 6 (1989) 499-503

THE ANOMALIES IN ELECTRICAL RESISTIVITY OF (Ce,La)$_3$In ALLOYS

C. Y. Liao

Department of Physics, Fu-Jen University, Taipei, Taiwan, R.O.C.

Y. Y. Chen, Y. D. Yao and C. S. Fang

Institute of Physics, Academia Sinica, Taipei, Taiwan, R.O.C.

Abstract

We have studied the electrical resistivity anomalies in $(Ce_{1-x}La_x)_3In$ with x = 0–0.09 in temperature range 4.2–300K. The electrical resistivity ρ(T) of Ce_3In decreases monotonically with temperature decreasing. At temperature around 50°K a weak Kondo-like behavior is followed by a curvature kink, (i.e., a resistivity minimum in a narrow temperature region) near 20 K, then the resistivity drops drastically in lower temperature due to RKKY interaction. As the amount of La substitution of Ce increased the depth of this resistivity minimum is increased and shifted to higher temperature and the magnetic moment correlation of Ce induced by RKKY interaction is gradually disappear. This result is different from its isostructure alloys $(Ce_{1-x}La_x)_3Sn$ in which Kondo-like behavior is smeared out by La substitution and make us to believe the size and electronic structure effects have played an important roles in the competition of spin disorder interaction and RKKY interaction. The X-ray photoemission experiment which have also been arranged for investigation in these aspects will be reported.

RESULTS AND DISCUSSION

Ce_3In is a heavy-fermion system, with a cubic Cu_3Au crystal structure. In the ground state the linear coefficient of the specific heat is 700 mj/mole Ce K (ref. 1).

With high purity Ce_3In no magnetic order is found as temperature down to 1.5 K. Its temperature dependent resistance (Fig. 1) decreases slowly below room temperature, then falls rapidly below about 25 K signaling the onset of coherence in the Kondo spin or valence fluctuation scattering.

Recently we have studied the La substitution of Ce in Ce_3In and found the anomalies in its resistivity ρ(T). In our lastest samples which were made from high purity Cerium and Indium, 99.98% and 99.999% respectively, a weak kink was found around 22K in ρ(T) which was not observed in higher purity Ce_3In (made from higher purity Ce 99.99%). In its alloys $(Ce_{1-x}La_x)_3In$ with x = 0.03, 0.06 and 0.09 Kondo-like resistivity ($\partial\rho/\partial T < 0$) were observed (Fig. 1). The weak kink found in Ce_3In is enhanced and formed a minimum at same temperature scale. An interesting phenomenon is that as La substatution up to 9%, no spin magmetic moment coherence is found even as temperature down to 4.2K. This behavior is very similar to the mixed valence alloys, $(Ce_{1-x}La_x)_3Pd$ (Fig. 2). In which a small amount of La (3% atomic weight) completely removed the coherence of spin magnetic moments (ref. 2) and a resistivity up-turn is shown. The kondo-hole mechanism, used in the interpretation of these phenomena for $(Ce_{1-x}La_x)_3Pd$, will be adequate to the explanation of this system $(Ce_{1-x}La_x)_3In$, i.e., the Ce vacancies can be treated as a Kondo-hole which play a same role in ρ(T) as a Kondo magmetic moment.

REFERENCE

1. Y.Y. Chen, J. M. Lawence, J. D. Thompson and J. O. Willis, Phy. Rev. B. 40, 16 (1989).
2. Theroetical and Experiental Ascepts of Valence Fluctuations and Heavy Fermions C. C. Gupta and S. K. Malik (1989) p. 169.

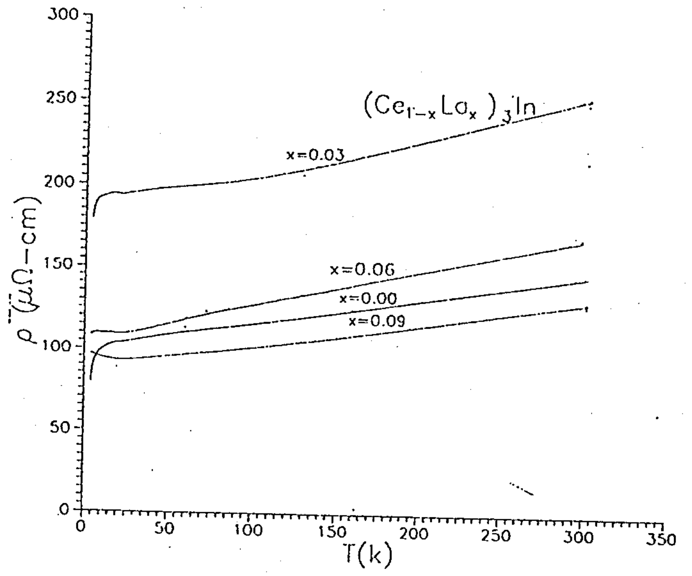

Fig. 1. Resistivity of $(Ce_{1-x}La_x)_3In$ for x = 0.00, 0.03, 0.06 and 0.09.

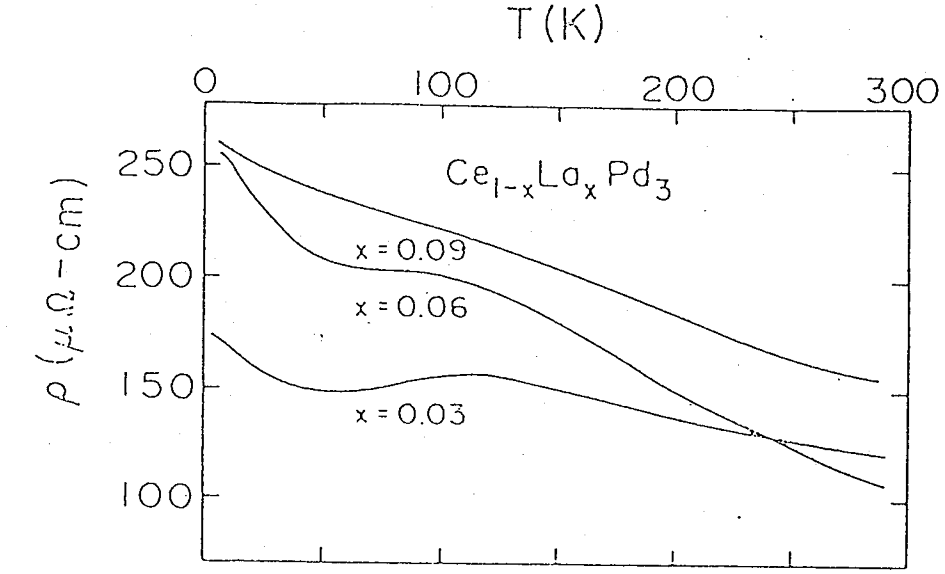

Fig. 2. Resistivity of $(Ce_{1-x}La_x)Pd_3$ for x = 0.03, 0.06 and 0.09.

EFFECT OF La SUBSTITUTION ON THE PHASE TRANSITION IN Ce_3Al COMPOUND

Y. Y. Chen, Y. D. Yao, C. C. Chen and R. L. Luo

Institute of Physics, Academia Sinica, Taipei, Taiwan, R.O.C.

Abstract

The phase transition discovered in resistivity and susceptibility measurements of the compound Ce_3Al was found to be influenced by La substitution of Ce. In a series of resistivity, susceptibility and thermal expansion measurements, we observed that the transition temperature changed from near 100K to about 77K as the amount of La substitution increased from zero to 9% of Ce. This effect is connected to the result reported in pressure dependent resistivity measurements in which the transition temperature was shifted to higher value by pressure increase. To investigate any variance in valence states of Ce came along with this phase transition change, X-ray photoemission experiments were also performed. The origins of this phase transition change will be discussed in terms of chemical pressure and valence state.

RESULTS AND DISCUSSION

The compound Ce_3Al has a hexagonal Ni_3Sn structure. The resistivity measurements (Fig. 1) and thermal expansion (Fig. 2) measurements show around 100K there is a first order phase transition occurrence. At low temperature the resistivity is Kondo-like ($d\rho/dT < 0$); estimating the resistance minimum as the Kondo temperature gives $T_k \cong 10 - 20K$. A sharp peak around 3K in $\rho(T)$ is understood as a ferromagnetic order by susceptibility result (Fig. 3). Recently we have studied the effect of La substitution on the 100K phase transition in alloys $(Ce_{1-x}La_x)_3Al$ (Fig.

4). The resistivity and magnetic susceptibility results show the phase-transition temperature is decreased from 100K to about 77K as the amount of La substitution increased to 9% of Ce. This effect is consistent with the result reported in the pressure dependent resistivity measurements in which the transition temperature is increased by the applied pressure (Fig. 5). Our explanation is that the larger ionic size of La expands the interatomic distance (Fig. 6) and favors the phase transition occurance at lower temperature, whereas the external pressure resists the lattice-expansion phase transition.

The susceptibility in these phase is of Curie-Weiss from $\chi(T) = C/(T + \Theta)$ with $U_{eff} = 2.52\mu_b$. The U_{eff}, not changed by La substitution, indicates Ce in these alloys are also trivalent. These result is also supported by our XPS spectrum in which no distinction could be told between the compound Ce_3Al and its alloys $(Ce_{1-x}La_x)_3Al$.

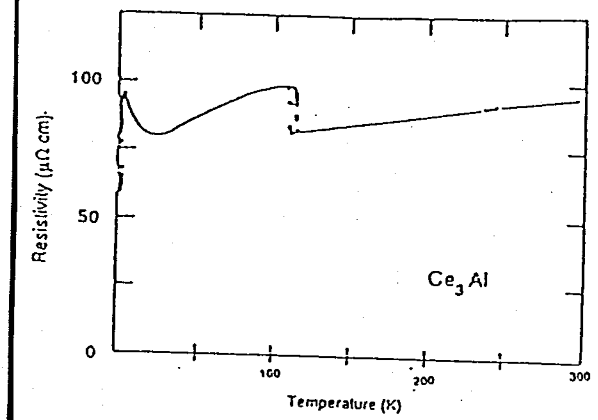

FIG. 1. Resistivity of Ce_3Al

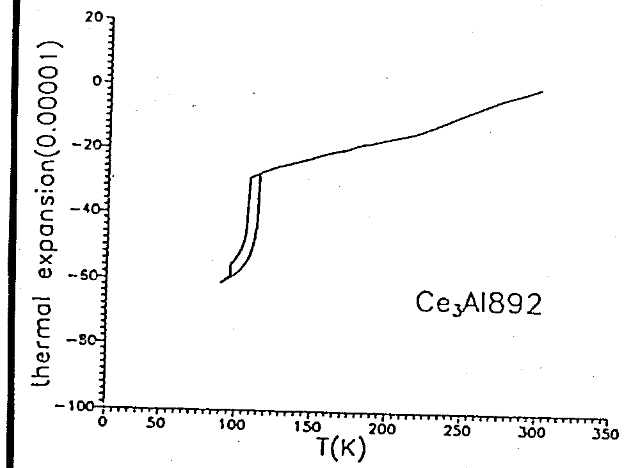

FIG. 2. The thermal expansion vs temperature for Ce_3Al

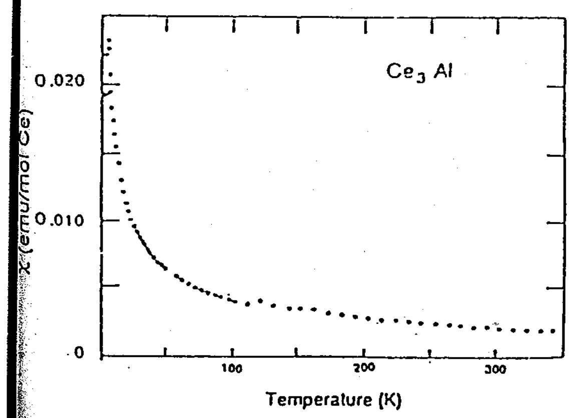

FIG. 3. Susceptibility of Ce_3Al for 0–350 K.

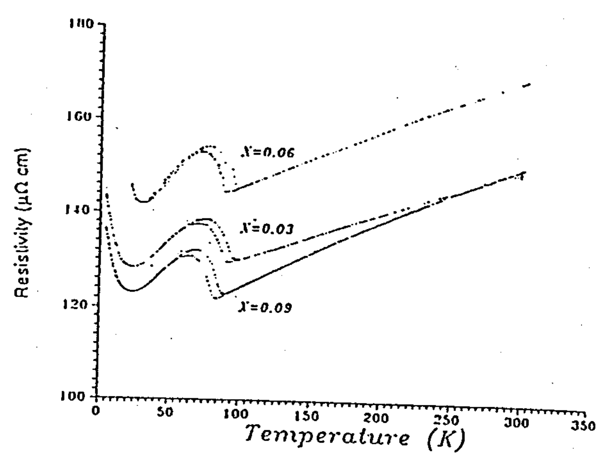

FIG. 4.

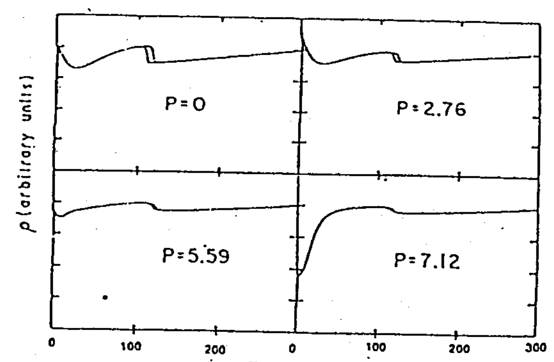

FIG. 5. The resistance vs temperature for Ce_3Al for several pressures in the range 0– 7.12 kbar.

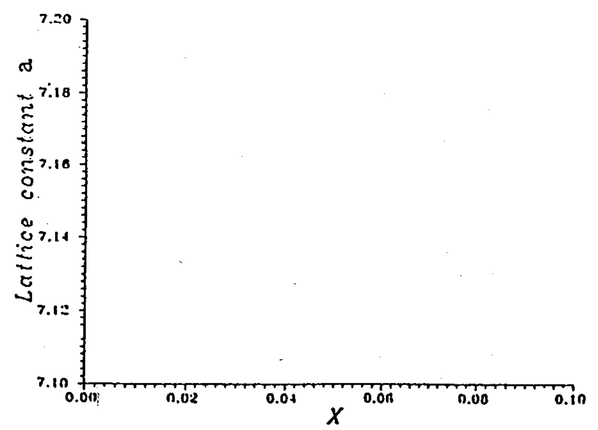

FIG. 6.

由脈波探討經絡與能量的分配

王唯工，徐則林，＊王林玉英，盧友仁，蔣宜

台灣省台北市南港中央研究院物理所生物物理實驗室

＊台灣省台北市國立師範大學物理系

本文曾發表於針灸研究發展與臨床應用研討會

中華民國七十八年三月　台中，台灣

摘　要

我們認爲內臟可視爲有各自不同振動特性的大動脈樹〔 1 ， 2 〕，而經絡則是一群爲同一動脈相聯的動脈樹，動脈樹振動的最大部位既針灸穴位之所在〔 2 ， 3 〕，改變這些動脈樹的物理性質（如以針灸或指壓穴道），其振動狀態則會改變，而造成全身共振能量的重新分配。

實驗上可從一簡單的氣球，水管模型，概括的了解此能量的基本分配關係，由改變某一水管路徑上氣球的振動狀態，可影響其他水管路徑之流量，而各振動頻率的能量經過重新分配的結果亦可由流量之改變觀察得知，簡單物理模型流量分配顯示有相生相剋的關係，而中醫所謂之相生相剋關係，則可能爲身體共振能量分配的基本規律，可由非線性波動力學之法則得到圓滿的解釋。

我們已經證實經絡之存在〔 3 〕，此報告的人體實驗資料則顯示，likely壓不同經絡穴道對不同經絡脈波之各諧振波有不同的選擇性，此經由壓穴道而造成全身脈波能量重新分配的機制，可能卽爲中醫相生相剋及頭痛針脚之治療基本原理。

前　言

近來，針灸的醫療效果已經得到普遍的認知與肯定，針灸與穴道，經絡間的密切關係也廣為所知，因而了解針灸效應的實際生理機轉卽成爲一個重要的課題。

先前，我們由一些觀察脈波變化的實驗曾陸續提出一些觀點，我們認爲不同的臟器可各視爲一個大動脈樹，而各臟器似乎有各自不同的共振特性〔１，２〕。其中，肝的血流變化可能主要由頻率和心跳速度相同的諧振波的強度所表現，而腎的變化則主要可能由頻率爲心跳速度兩倍的諧振波的強度所表現，脾則爲三，肺爲四，胃爲五，膽則爲六。到了四肢時，經絡則似乎是一群爲同一動脈相聯之動脈樹，動脈樹振動的最大部位卽針灸穴位之所在〔３〕。而脈波卽爲全身各內臟、器官、經絡、穴道等共振狀態的綜合表現。同時身體不同部位，因爲血管長度的不同，對脈波有不同的頻率選擇性，頭部對心跳速度六倍的頻率有較強的選擇性，而手則選四，脚則選二〔２〕。我們認爲：如果動脈樹的物理性質遭受改變，（如針灸或指壓穴道），其共振狀態就會因之改變，而造成全身共振能量的重新分配，繼而造成血流的重新分佈，這些變動卽可由脈波表現出來。

在這篇報告中，我們就將從能量分配的觀點出發，對一些中醫習之已久，且再再顯示令人驚奇的有效性的一些針灸規則，如頭痛針脚，以及最主要的，針灸取穴時做爲基本依據的相生相尅關係，做一些探討。

我們首先以簡單的汽球水管作爲內臟及血管循環系統的物理模型，測得其各管路流量的變化有相生相尅的關係。進而，我們發現，中醫相生相尅的法則中各內臟相關頻率間的關係〔１，２〕，與由非線性波動力學所導出的一些波動能量轉換規則〔４，５〕，有極高度的相合性。而我們的人體實驗顯示，不同經絡的穴道受壓時，對脈波各共振波能量會產生不同

的分配型態。這些結果指出：相生相尅法則也許就是脈波各共振波能量非線性轉換的結果，而穴道物理性質改變，確實會使脈波共振波能量依一定的規則重新分配，繼而影響血液的分佈及身體的健康，也許卽爲中醫針灸和頭痛針脚的基本原理。

我們希望這些工作能促使對針灸基本運作法則之生理基礎能有更進一步的了解。

實驗的詳細步驟及理論推導，則分三部份詳述於後。

(一)物理模型實驗

(甲)實驗步驟

實驗設備大致和我們先前的報告相似〔 1 〕，如圖一所示，我們以六條密閉，具有不同彈性及管徑的水管模擬血液循環系統，而以五個不同形狀大小，體積從 1 cc.至10cc.的汽球接在一至五條管路的中央，模擬人體的五臟，五個夾子，# 1 ，# 2 ，# 3 ，# 4 ，# 5 的開關，則分別用來控制 1 至 5 水管的流量，以模擬內臟微循環系統阻抗的改變，第六條水管的中央則和一個線性壓力轉換器相接（ Validyne Model DP 103 ），經過第六管路的壓力波形則經此由一數位轉換器轉換成數位訊號，而由示波器（ The E.G.G. Signal Average, model 4202)顯示出波型，電動脈動馬達則以 1.67 Hz 之固定頻率將牛乳由水管一端打入，使之流經所有的管路及汽球後由水管另一端流出。我們並以出水口之高低調整系統內的充水量，而使各汽球能明顯的以特有共振頻率振動。一個超音波流速儀（ Sonovit SV-2, Schiller ）之探頭則以60度的架子固定在水管的正上方，以 10 MHz 頻率之超音波測量各水管的流速，並測量以不同的夾子# 1 ，# 2 ，# 3 ，# 4 ，# 5 夾住相對應水管時，其它管路的流速，流速資料則經 SV - 2內含之記錄器載下，而以求積儀求得相對應的流量。

(乙)實驗結果

不同管路受夾時，第六管路脈波波型的變化狀態，已發表在我們先前的報告中。

表一(A)爲在不同管路被夾時，其它各管路的流量變化情形，表一(B)爲表一(A)中各管路流量相生相剋示意表。若A管路受夾時（ A流量下降 ）會造成B管路流量上昇達10%以上，則以A$\rightharpoonup$B表示A流量會剋B流量。反之，若A管路受夾會造成B管路流量也下降，且達10%以上，則以A$\overset{+}{\rightharpoonup}$B表示A流量會生B流量。在表一(A)、(B)中A管與C管有明顯相剋的關係，A管與D管則明顯相生，而B與E 、C與D 、C與E則相剋，而A與B 、D與E相互間則不大有影響。表二(A)、(B)爲另一組汽球水管的實驗結果。此組組合中A與B 、A與C 、B與E 、C與D有相剋的關係，而A與D則有明顯的相生關係。

(二)非線性波動力學與相生相剋關係

(甲)理論

非線性波動力學指出：一個頻率爲Ｌ的波的能量可以轉換成兩個頻率爲Ｍ及Ｎ的波的能量，Ｌ爲Ｍ與Ｎ的代數和。即：

$$L = M + N,$$

所以，　$L \xrightarrow{+} M$，　$L \xrightarrow{+} N$，

$$M \rightleftarrows N$$

也就是說，如果Ｌ的能量增加，則Ｍ或Ｎ的能量也會增加，即Ｌ與Ｍ和Ｎ有相生的關係，反之，如果Ｌ的能量維持一定，那麽Ｍ的能量增大時，Ｎ的能量就會變小，即Ｍ與Ｎ之間有相剋的關係。

(乙)與相生相剋關係之比較

圖二(A)爲根據上述理論所得到的一些非線性波動能量間的轉換規則。在規則中，頻率爲二的波的能量可以轉換成頻率爲一的波的能量，而頻率爲四的波的能量可以轉換成頻率爲二的波的能量，而六則可轉換成三。因此二生一，四生二，六生三。頻率爲四的波的能量又可換成頻率爲一及三的波的能量，五則可換成二和三，或一和四，六則可換成二和四，或一和五。因此，一剋三，三剋二，而四剋一，一剋五。四因爲可以生二，所以四與二間彼此相剋的關係就不成立。

圖二(B)爲中醫相生相剋法則，及法則中各內臟相關共振頻率，按照肝一、腎二、脾三、肺四、胃五、膽六，間的關係。其中水（腎２）生木（肝１）、金（肺４）生水（腎２）、火（膽６）生土（脾３）、而生（脾３）剋水（腎２）、金（肺４）剋木（肝１）、木（肝１）剋土（胃５）。

在此我們依許多中醫所建議的將膽列入火性。圖二(A)與圖二(B)對照，二者頻率間的關係顯示高度的相合性。

㈢人體經絡能量分配實驗

㈠實驗步驟

實驗步驟與我們先前的報告相似，我們將記錄脈波所用之壓力轉換器（PSL-200GL, Kyowa Electronic Ins. Co. Ltd. Japan）以膠紙固定在受測者之穴位上，並以一具有小鈕釦之可調節鬆緊帶綁住，藉以調整壓力轉換器所承受的壓力，使觀測穴位上之脈波波幅呈現最大。壓力轉換器與一示波器相聯，脈波上各點數值經此由一14位元類比／數位轉換器與一 IBM 個人電腦相聯並記錄。所記錄的脈波則由一傅利葉轉換軟體程式取週期 $T = 1$ 波分析。所有受測者之年齡均在 23-43 歲之間，在實驗中以仰姿靜躺。

我們分別記錄了當足少陰腎經的湧泉穴被直徑 0.25 公分的細棍擠壓時，位於手少陰心經之神門脈，及頭部足少陽膽經之頷厭脈脈波的變化。以及當手陽明大腸經的合谷穴被壓時，頷厭脈脈波的變化。

㈡實驗結果

圖三(A)及表三(A)爲頷厭脈脈波的十二個傅利葉分量在合谷穴受壓時八組實驗值的平均變化情形。我們以受壓前的頷厭脈脈波爲控制值，而以壓合谷穴道時與壓合谷穴道後四分鐘之頷厭脈波分別與之作比較。在合谷穴受壓時頷厭脈脈波之十二個傅利葉分量的百分比強度差值，其第四、第七及第十諧振波皆顯著大於零，（$P < 0.05$），而第二、第五及第九諧振波則顯著小於零，（$P < 0.05$），第四及第七諧振波處並呈現明顯的峰值。在壓後四分鐘，這些效應皆明顯降低。

圖三(B)及表三(B)則爲壓湧泉穴時頷厭脈波六組實驗之平均值變化情形。以壓湧泉穴前之頷厭脈波作控制值，壓湧泉穴時頷厭脈波的十二個傅利葉分量之百分比強度差值，在第三、第六、第七及第九諧振波皆明顯大於零，（$P < 0.05$），而在第十一諧振波處明顯小於零，（$P < 0.05$）。第三諧振波處呈明顯的峰值，而第六、第七諧振波間，以及第九、第十諧振波間，皆亦呈現明顯的峰值。在壓後四分鐘這些效應皆明顯降低。

圖三(C)及表三(C)則爲壓湧泉穴時神門脈波六組實驗之平均值變化情形。以壓湧泉穴前之神門脈波作控制值，壓湧泉穴時神門脈波的十二個傅利葉分量之百分比強度差值，在第一第三第四，及第六諧振波皆明顯大於零，（$P < 0.05$）。第三第六諧振波處呈明顯的峰值，在壓後四分鐘這些效應皆明顯降低。

圖四(A)、(B)、(C)與表四(A)、(B)、(C)則分別爲壓合谷穴及壓湧泉穴時頷厭脈，及壓湧泉穴時神門脈脈波的十二個傅利葉分量相角變化情形。當穴道受壓時，各諧振波相角大都會有變小的趨勢，也就是說各諧振波速度會變快，這些效應在壓後四分鐘也會明顯降低。

討　論

我們由汽球水管模型實驗中得知，當不同汽球的振動能量因爲管路受阻而改變時，則脈波波型會產生相對應的變化〔 1 〕，並造成各管路共振能量的重新分配。由各管路流量變化情形顯示，波動能量的轉換分配，即使在簡單的物理模型中亦顯示相生相剋的關係。

而中醫相生相剋法則，與由非線性波動力學所導出的波動能量轉換規則間所顯示出的高度相合性，更強烈的暗示；相生相剋法則也許就是脈波各共振波能量非線性轉換的結果。

我們對人體經絡能量分配的實驗則顯示，當不同經絡的穴道受到影響時，就會對脈波各共振波能量產生不同的分配型態。壓合谷穴時會特別加強領厭脈第四，第七諧振波的強度，而壓湧泉穴時則會特別加強領厭脈第三、第六及第九諧振波的強度，以及神門脈第三，第六諧振波的強度。這些資料指出，穴道物理性質的改變，確實會改變脈波共振波能量的分配，因爲脈波的分佈直接影響血液的分配，而身體的機能與健康狀況和血液的分配又有著密不可分的關係，這也許即爲中醫針灸和頭痛針脚的基本原理。

在這篇報告中，我們提出一些基本的研究結果，我們希望這些工作能成爲對針灸基本運作法則做更深入研究的一條方向。

參考資料

1. Wang, W. K.,Lo, Y. Y., Chieng, Y., Hsu, T. L., and Wang Lin, Y. Y., "Resonance of organs with the heart"; To be published in "Advanced in Biomedical Engineering", Hemisphere, Washington, D.C., Ed. W. J. Young.
2. Wang, W. K., Wang Lin, Y. Y., Hsu, T. L., and Chieng, Y., "Some Fundation of pulse feeling in Chinese medicine"; To be published in "Advanced in Biomedical Engineering", Hemisphere, Washington, D.C., Ed. W. J. Young.
3. 王唯工、王林玉英、徐則林、蔣宜，"由脈波探討經絡的存在"，第一屆中醫診斷大會論文，1988。
4. Migulin, V., "Basic Theory of Oscillations", Mir publisher, Moscow, 1983.
5. Whitham, G.B., "Linear and Nonlinear Waves", John Wiley and Sons, New York, 1974.

附圖解說

圖一：循環系統之汽球水管模型，單箭頭代表牛乳流動方向，雙箭頭爲電子訊號輸出方向。

圖二(A)：非線性波動能量頻率轉換規則。＋：代表相生，並以實箭頭連接相生之二頻率。－：代表相剋，並以虛箭頭連接相剋之二頻率。

圖二(B)：中醫相生相剋法則，及各內臟相關頻率，此圖將膽歸屬火性。

圖三：壓穴道對脈波之影響，所示爲壓穴道時（○），與壓穴道後四分鐘（□）之測試脈波十二個傅利葉分量之規一化振幅以壓穴道前之脈波爲控制值相比的差值百分比。

* 代表該點爲零之T-測試機率，$P < (0.05)$。

** 代表該點爲零之T-測試機率，$P < (0.01)$。

*** 代表該點爲零之T-測試機率，$P < (0.001)$。

虛線代表所連相鄰二點爲相同之值之T-測試機率，$P < (0.05)$。

單線代表所連相鄰二點爲相同之值之T-測試機率，$P < (0.05)$。

雙線代表所連相鄰二點爲相同之值之T-測試機率，$P < (0.01)$。

三線代表所連相鄰二點爲相同之值之T-測試機率，$P < (0.001)$。

(A)：壓合谷對頷厭脈影響。

(B)：壓湧泉對頷厭脈影響。

(C)：壓湧泉對神門脈影響。

圖四：壓穴道對脈波之影響。所示爲壓穴道時（○），與壓穴道後四分鐘（□）之測試脈波十二個傅利葉分量之相角以壓穴道前之脈波爲控制值相比之差值。

* 代表該點爲零之T-測試機率，$P < (0.05)$。

** 代表該點爲零之T-測試機率，$P < (0.01)$。

*** 代表該點爲零之T-測試機率，$P < (0.001)$。

(A)：壓合谷對頷厭脈影響。

(B)：壓湧泉對頷厭脈影響。

(C)：壓湧泉對神門脈影響。

表一(A)：利用求積儀所讀取的流量（面積値）及其比率

頻率＝1.67 Hz

夾子 數據 測量位置	1＃	2＃	3＃	4＃	5＃	
A₁	4.55*	5.32	5.67	3.97	5.25	(面積
	1.0	1.17	1.25	0.87	1.15	(比率)
A₂	5.09	4.01*	5.33	4.15	4.63	
	1.27	1.0	1.33	1.03	1.15	
A₃	5.65	5.02	4.87*	8.06	4.29	
	1.16	1.03	1.0	1.66	0.88	
A₄	7.03	7.18	9.98	8.74*	10.08	
	0.80	0.82	1.14	1.0	1.15	
A₅	3.51	3.97	4.34	3.87	3.57*	
	0.98	1.11	1.22	1.08	1.0	

*：所有夾子皆開

表一(B)：各管路相生相剋關係表

$A_1 \underset{-}{\overset{-}{\rightleftharpoons}} B_2$	$B_2 \underset{-}{\rightleftharpoons} C_3$	$C_3 \underset{-}{\overset{-}{\rightleftharpoons}} D_4$	$D_4 \underset{-}{\rightleftharpoons} E_5$
$A_1 \overset{-}{\rightleftharpoons} C_3$	$B_2 \overset{+}{\rightleftharpoons} D_4$	$C_3 \underset{+}{\overset{-}{\rightleftharpoons}} E_5$	
$A_1 \underset{+}{\overset{+}{\rightleftharpoons}} D_4$	$B_2 \underset{-}{\overset{-}{\rightleftharpoons}} E_5$		
$A_1 \underset{-}{\rightleftharpoons} E_5$			

＋：相生　　－：相剋

表二(A)：利用求積儀所讀取的流量（面積値）及其比率

頻率＝1.67 Hz

夾子 數據 量 置	1＃	2＃	3＃	4＃	5＃	
A₁	5.15*	5.18	5.93	4.35	5.78	(面積値)
	1.0	1.01	1.15	0.84	1.12	(比率)
A₂	5.11	4.83*	5.09	4.78	5.64	
	1.06	1.0	1.05	0.99	1.17	
A₃	8.36	8.73	7.13*	9.89	8.33	
	1.17	1.22	1.0	1.39	1.17	
A₄	5.44	6.0	8.19	7.07*	7.37	
	0.77	0.85	1.16	1.0	1.04	
A₅	3.91	4.07	4.75	3.99	3.65*	
	1.07	1.12	1.30	1.09	1.0	

：所有夾子皆開

表二(B)：各管路相生相剋關係表

$A_1 \rightleftharpoons B_2$	$B_2 \rightleftharpoons C_3$	$C_3 \underset{-}{\overset{-}{\rightleftharpoons}} D_4$	$D_4 \rightleftharpoons E_5$
$A_1 \underset{-}{\overset{-}{\rightleftharpoons}} C_3$	$B_2 \overset{+}{\rightleftharpoons} D_4$	$C_3 \underset{-}{\overset{-}{\rightleftharpoons}} E_5$	
$A_1 \underset{+}{\overset{+}{\rightleftharpoons}} D_4$	$B_2 \underset{-}{\overset{-}{\rightleftharpoons}} E_5$		
$A_1 \underset{-}{\rightleftharpoons} E_5$	$B_2 \overset{-}{\rightleftharpoons} C_3$		

＋：相生　　－：相剋

表三：所示者爲脈波之各諧振波在棍壓穴道時，及壓穴道後四分鐘，以壓穴道前之控制值相比，所得之規一化振幅強度差值百分比

(A)壓合谷對頷厭脈影響　　實驗數＝8

頻率數	1	2	3	4	5	6	7	8	9	10	11	12
壓穴道中	0.0	-5.1 *	-0.3	9.8 *	-7.6 **	1.3	21.4 *	2.3	-8.6 *	15.2 *	23.1	-7.0
標準誤差	5.0	5.5	10.8	11.9	4.6	11.5	21.4	13.3	8.3	15.5	62.1	17.1
		!		!	!!!	!	!	!	!	!!!		
壓後四分鐘	0.0	-0.1	-1.0	-7.3 **	-5.7 *	-3.5	0.5	-5.4	-2.4	10.4	6.9	4.0
標準誤差	2.0	7.9	7.5	6.0	7.1	5.8	13.4	15.3	8.2	17.7	29.5	20.4

(B)壓湧泉對頷厭脈影響　　實驗數＝6

頻率數	1	2	3	4	5	6	7	8	9	10	11	12
壓穴道中	1.5	-0.6	8.0 *	-6.1	2.3	20.0 **	15.5 **	2.3	31.9 **	26.3	-14.0 *	20.4
標準誤差	2.1	4.6	7.9	9.5	6.3	12.1	9.5	9.4	20.6	36.2	15.2	34.7
			!	!!		!!		!	!!		!	!
壓後四分鐘	-1.5	-2.8	-3.4	-5.2	-3.6	-2.9	5.1	-5.1	0.8	6.5	-16.9	-15.6
標準誤差	3.2	7.4	15.4	11.0	9.2	16.2	14.2	13.0	14.4	34.4	23.7	30.4

(C)壓湧泉對神門脈影響　　實驗數＝6

頻率數	1	2	3	4	5	6	7	8	9	10	11	12
壓穴道中	1.8 *	-2.7	18.9 **	2.3	11.7 *	30.5 **	6.6	21.6	29.8	89.4	91.1	82.7
標準誤差	2.1	6.6	9.0	10.5	12.8	17.9	21.2	28.1	41.7	146.6	226.2	180.5
			!!!	!!		!	!					
壓後四分鐘	-2.5	2.8	2.3	3.9	5.2 *	6.3	-1.5	4.2	-3.8	10.3	7.0	-3.1
標準誤差	4.6	11.8	10.9	10.2	6.0	11.8	19.8	17.1	26.5	67.1	43.3	17.9

＊：P＜(0.05)　　＊＊：P＜(0.01)　　＊＊＊：P＜(0.001)　　T－測試差値爲零之機率

！：P＜(0.05)　　！！：P＜(0.01)　　！！！：P＜(0.001)　　T－測試二相鄰頻率之値相等之機率

表四：所示者爲脈波之各諧振波在棍壓穴道時，及壓穴道後四分鐘，以壓穴道前之角度爲控制值相比，所得之角度差值

(A)壓合谷對頷厭脈影響

頻率數	1	2	3	4	5	6	7	8	9	10	11	12
壓穴道中	-1.7	-2.7	-8.6 **	-6.2 *	-11.6 **	-20.8 **	-17.1 *	-11.4 *	-17.4	-7.7	-3.9	12.1
標準誤差	3.1	5.7	7.6	9.3	10.6	16.1	20.9	17.4	28.0	48.9	35.8	26.5
壓後四分鐘	-0.5	0.6	0.0	1.9	-4.3	-6.7	-5.1	-3.4	-2.0	5.8	-20.0	3.6
標準誤差	2.6	5.6	6.5	8.9	10.9	13.3	16.5	18.4	19.1	34.0	43.6	41.7

(B)壓湧泉對頷厭脈影響

頻率數	1	2	3	4	5	6	7	8	9	10	11	12
壓穴道中	-0.8	-2.4	-2.6 *	2.0	-7.9 *	-4.9	3.3	-3.1	3.1	24.4 *	5.7 *	-1.7
標準誤差	1.7	4.9	4.6	4.4	7.5	7.2	9.2	10.9	20.8	24.2	36.1	54.3
壓後四分鐘	2.1	3.6	3.8	2.5	1.8	2.5	6.3	8.4	17.4 *	7.0	-18.7	-10.6
標準誤差	3.9	7.4	8.4	8.6	16.0	15.8	9.9	27.2	17.5	47.7	34.1	43.3

(C)壓湧泉對神門脈影響

頻率數	1	2	3	4	5	6	7	8	9	10	11	12
壓穴道中	-2.4 **	-9.1 *	-10.8 *	-3.5 *	-15.2 *	-4.4	-9.0	-14.6	-17.8	-15.7	-1.0	1.7
標準誤差	1.5	6.7	10.8	3.7	16.8	21.5	18.4	30.7	35.5	44.0	28.1	17.0
壓後四分鐘	0.3	-2.0	0.0	-2.5	-0.5	3.9	-0.2	2.8	6.0	-11.4	-9.0	-5.6
標準誤差	2.2	4.9	8.0	11.2	14.0	19.4	19.0	20.8	25.2	38.3	34.9	57.7

＊：P＜(0.05)　　＊＊：P＜(0.01)　　＊＊＊：P＜(0.001)　　T－測試差値爲零之機率

！：P＜(0.05)　　！！：P＜(0.01)　　！！！：P＜(0.001)　　T－測試二相鄰頻率之値相等之機率

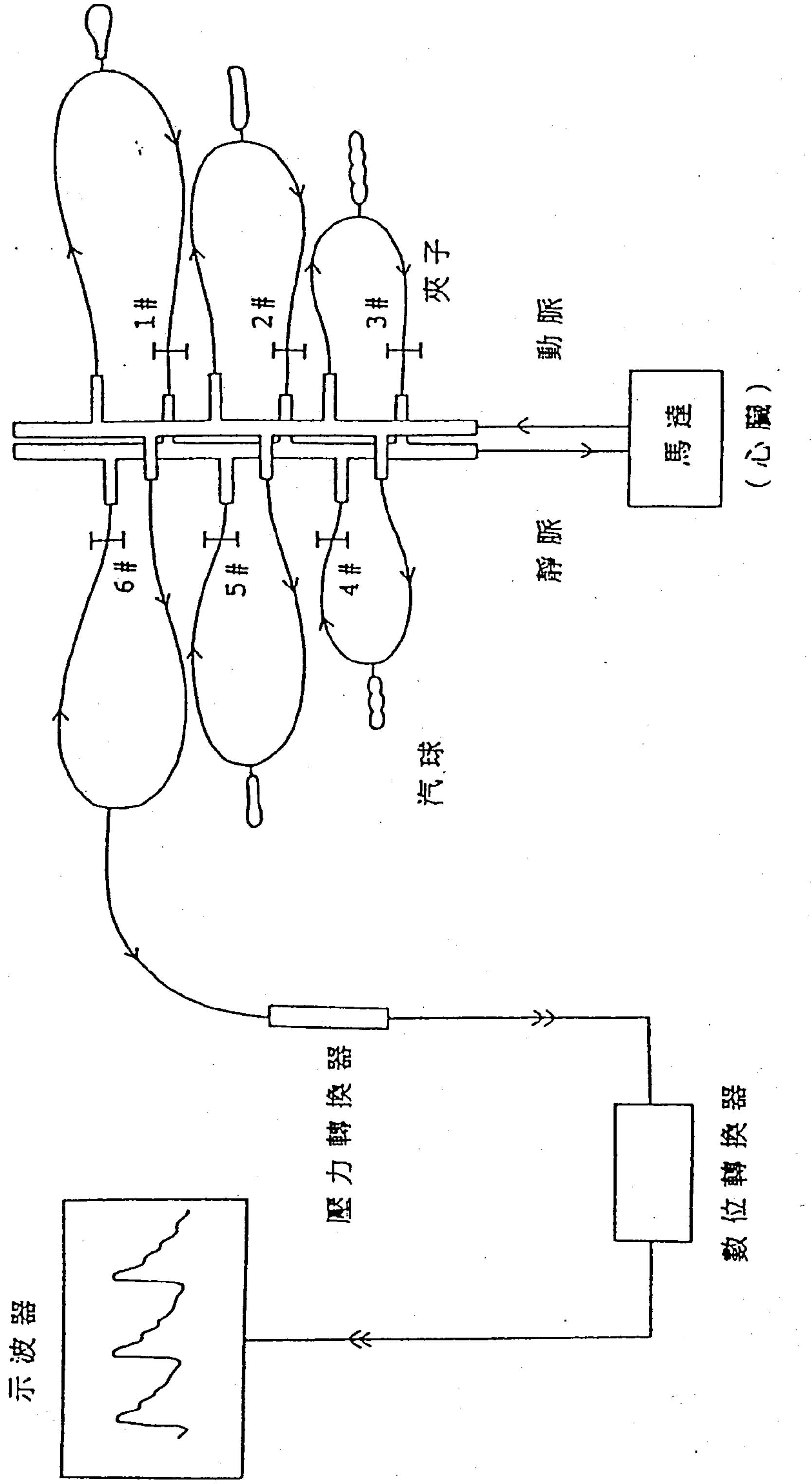

圖一

（A）： 非線性波動力學能量轉換規則

$2 \xrightarrow{+} 1+1$

$4 \xrightarrow{+} 2+2$

$6 \xrightarrow{+} 3+3$

$4 \longrightarrow 2,\quad 1+3$

$5 \longrightarrow 2+3,\quad 1+4$

$6 \longrightarrow 3,\quad 2+4,\quad 1+5$

$3+5 \xrightarrow{+} 4+4$

（B）： 中醫相生相剋法則

—— 相生

- - - 相剋

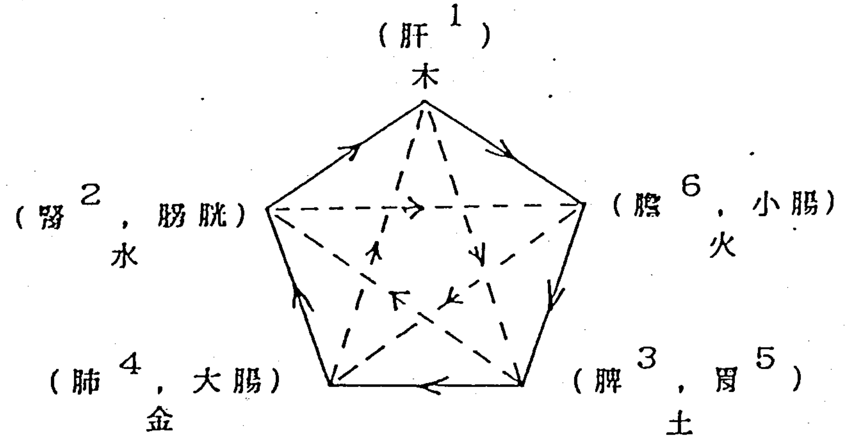

圖二

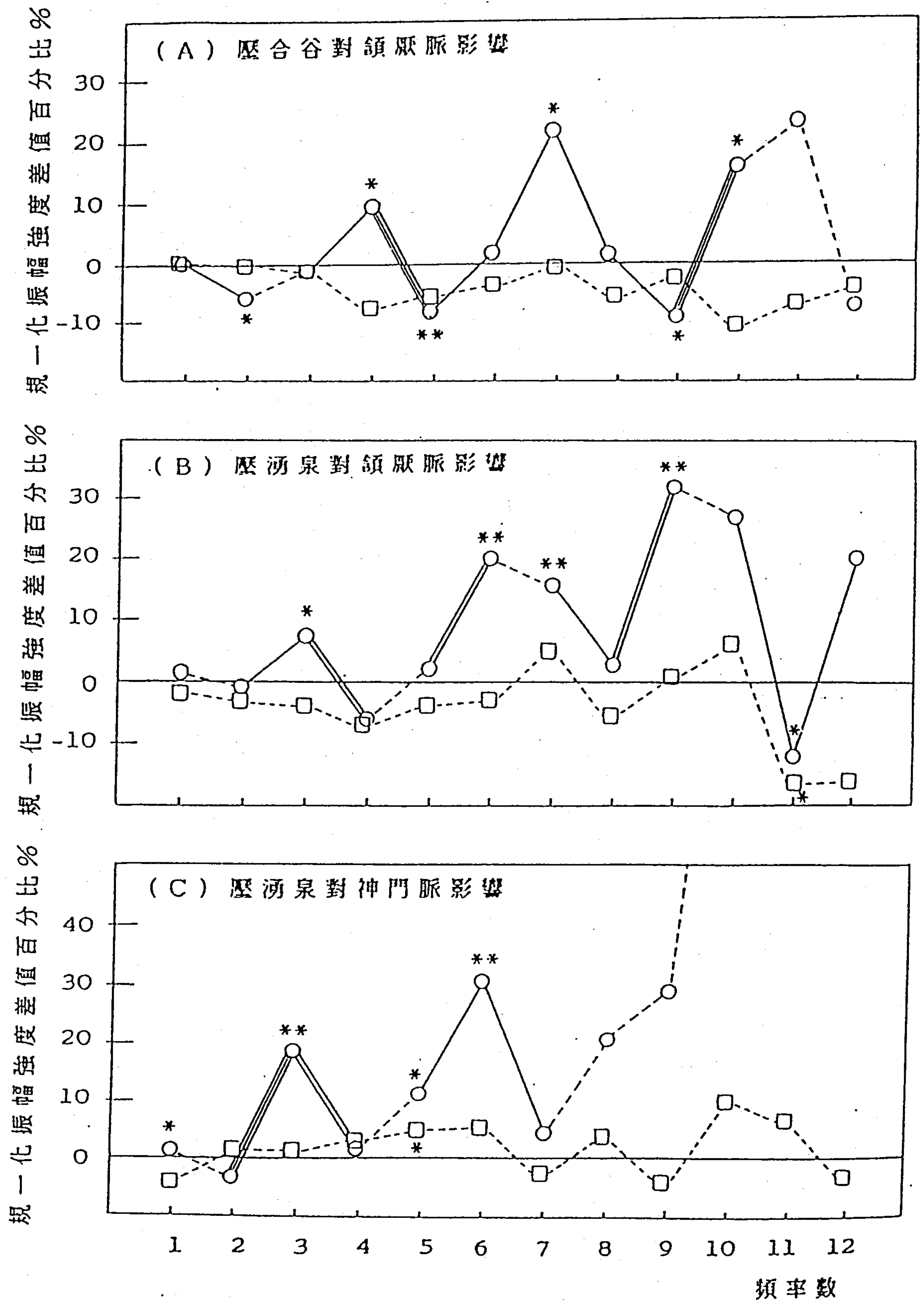
(A) 壓合谷對頷厭脈影響
(B) 壓湧泉對頷厭脈影響
(C) 壓湧泉對神門脈影響
規一化振幅強度差值百分比%
40
30
20
10
0
-10
*
**
1
2
3
4
5
6
7
8
9
10
11
12
頻率數

圖三

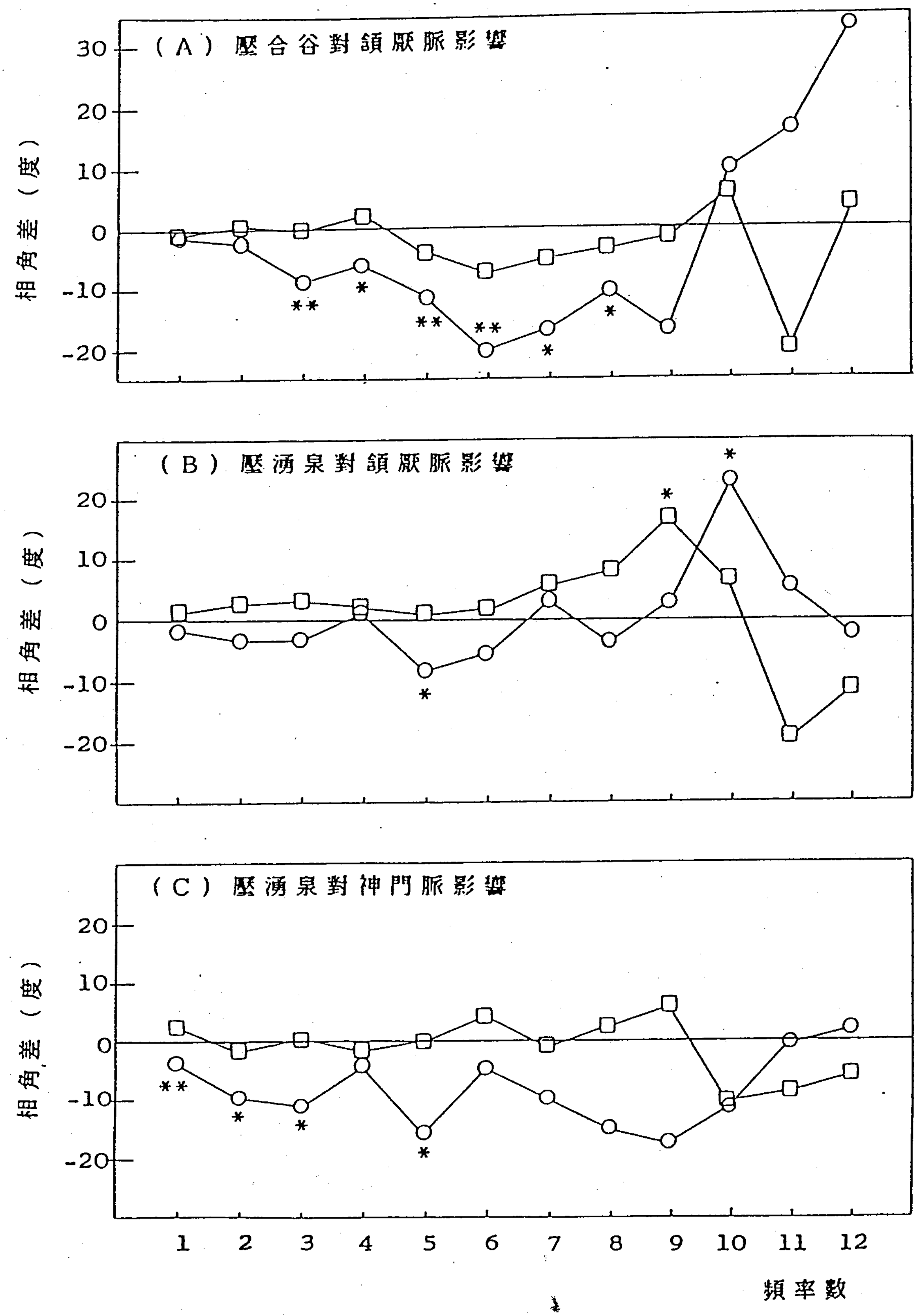
(A) 壓合谷對頷厭脈影響
(B) 壓湧泉對頷厭脈影響
(C) 壓湧泉對神門脈影響
相角差（度）
30
20
10
0
-10
-20
*
**
1
2
3
4
5
6
7
8
9
10
11
12
頻率數

圖四

非賣品

中央研究院
物理研究所集刊
第十九卷

發行人：
編輯者：中央研究院物理研究所集刊編輯委員會
出版者：中央研究院物理研究所　臺北市南港區
印刷者：永立印刷有限公司
電　話：三五一四一三三

中華民國七十九年六月出版